# METABOLIC AND BIOELECTRIC CROSSTALK IN DIRECTED DIFFERENTIATION AND SPATIAL PATTERNING OF IPSC-DERIVED CARDIOMYOCYTES

A Dissertation
Presented to
The Academic Faculty

by

Dennis Andre Norfleet II

In Partial Fulfillment
of the Requirements for the Degree
Doctor of Philosophy in the
Interdisciplinary Bioengineering Program

Georgia Institute of Technology
MAY 2023

# METABOLIC AND BIOELECTRIC CROSSTALK IN DIRECTED DIFFERENTIATION AND SPATIAL PATTERNING OF IPSC-DERIVED CARDIOMYOCYTES

Approved by:

Dr. Melissa Kemp, Advisor
Department of Biomedical Engineering
*Georgia Institute of Technology*

Dr. Craig Forest
Department of Mechanical Engineering
*Georgia Institute of Technology*

Dr. Manu Platt
Department of Biomedical Engineering
*Georgia Institute of Technology*

Dr. Sung Jin Park
Department of Biomedical Engineering
*Georgia Institute of Technology*

Dr. Eberhard Voit
Department of Biomedical Engineering
*Georgia Institute of Technology*

Dr. Ravi Kane
School of Chemical and Biomolecular Engineering
*Georgia Institute of Technology*

Date Approved: April 18, 2023

I dedicate this thesis to my parents, Dennis Andre Norfleet I and Veronica W. Norfleet, my brother, French Philip Norfleet, and my loving, supportive girlfriend Seleipiri Charles

# ACKNOWLEDGEMENTS

The completion of this Ph.D. stands as a testament to the efforts, time, and care invested in me by my family, friends, and support system. I would like to thank my mother and father for instilling a work ethic and a strong sense of self-efficacy in me. I would like to thank Dr. Melissa Kemp for taking the chance on an excited 'newbie' in the field. The level of creative freedom I was afforded with this project and its development has done wonders for my confidence as a scientist, and I can honestly say it was one of the main reasons that this was the most enjoyable science endeavor that I've undertaken. She has done a masterful job of balancing constant solid support through the ebbs and flows of the Ph.D. and constantly pushing me to explore my limits and improve as a scientist and mentor. Next, I would like to thank my committee members for their valuable insights, advice, and input throughout my graduate training: Dr. Manu Platt, Dr. Craig Forest, Dr. Eberhard Voit, Dr. Sung Jin Park, and Dr. Ravi Kane. I would also like to thank research collaborators Dr. Michael Levin, Dr. Alexis Pietak, Dr. Juanita Matthews, Dr. Sean Palecek, and Dr. Bo Yang, all of whom were not only incredibly considerate with their advice and time, but also inspirational in their mastery of their respective research niches. I would like to all sources of financial support that I received throughout my training from the Bioengineering Ph.D. program, RISE Fellowship award, and Herbert P. Haley Fellowship award. I would like to thank the Kemp lab members with whom I've experienced countless failures and triumphs, aimless scientific debates, a fair share of SpongeBob jokes, and consistent support. I would like to especially thank Dr. Andrew Raddatz for being a consistent friend, source of support, idea bouncing board, and fellow

music connoisseur that really made a large impact on how much I enjoyed my Ph.D. Also, I would like to thank Sarah Seals, who provided a ‘newbie’ with an excellent foundation in benchtop work, planning, and organization (and was patient through my endless stream of questions when she was very busy). Finally, I would like to thank my girlfriend Seleipiri Charles, who has been an absolute rock throughout this process and inspires me to improve as a scientist, human and can always (seemingly magically) pull a smile and laugh out of me even on my toughest days and I am forever grateful. Finally, I would like to thank my best friends Jackson Padgett, Maurice Call, Sean Blount, Robert Niter, Anthony Johnson, and Michael Johnson, and Dylan Young, who have kept me sane throughout a tumultuous period in my personal life with constant laughs and invaluable brotherhood and routinely encourage me to stay focused and positive.

# TABLE OF CONTENTS

# LIST OF TABLES

# LIST OF FIGURES

# LIST OF SYMBOLS AND ABBREVIATIONS

| | |
|---|---|
| hiPSC | human induced pluripotent stem cell |
| hiPSC-CM | human induced pluripotent stem cell derived cardiomyocyte |
| PSC | pluripotent stem cell |
| M-CELS | multi-cellular engineered living systems |
| LIF | leukemia inhibitory factor |
| ESC | embryonic stem cell |
| hESC | human embryonic stem cell |
| TF | transcription factor |
| RPE | retinal-pigmented epithelial |
| PDMS | polydimethysiloxane |
| MI | myocardial infarction |
| HLA | Human leukocyte antigen |
| 2D | two-dimensional |
| 3D | three-dimensional |
| CNS | central nervous system |
| ABM | agent-based modeling |
| FEM | functional expression matrix |
| RIPPER | rule-based machine learning algorithm |
| $V_{mem}$ | voltage potential |
| X. laevis | *Xenopus laevis* |
| BETSE | bioelectric tissue simulation engine |
| CRISPRi | clustered regularly interspaced short palindromic repeats interference |

| | |
|---|---|
| PFA | Paraformaldehyde |
| DiBAC | distribution-based analysis of cell differentiation |
| HEPES | 4-(2-hydroxyethyl)-1-piperazineethanesulphonic acid |
| EGTA | ethylene glycol-bis(β-aminoethyl ether)-N,N,N′,N′-tetraacetic acid |
| GHK | Goldman-Hodgkin-Katz |
| ROI | region of interest |
| FI | fluorescence intensities |
| TSSL | tree superposition spatial logic |
| MEAs | microelectrode arrays |
| FVA | flux variance analysis |
| GPR | gene-protein-reaction rules |
| OCR | oxygen consumption rate |
| NGS | next generation sequencing |
| Cx43 | Connexin 43 |

# SUMMARY

The goal of multi-cellular engineered living systems is the design and manufacturing of multi-cellular systems with novel form or function using engineering design principles. Induced pluripotent stem cells represent an excellent tool to enable actualization of these design goals because of their intrinsic pluripotent capacity and recapitulation of various embryogenesis and organogenesis processes. The objective of this research was to investigate through computational modeling how molecular components of bioelectric and metabolic systems alter multicellular bioelectric patterning and cell metabolic flux dynamics, and to extend system understanding to guide emergent morphogenic outcomes via external modulation of the culturing environment. The central hypothesis of this work was that specific media compositions can alter molecular components of bioelectric and metabolic multicellular systems in a predictable manner, leading to desired morphologies, cell phenotypes, and novel functionalities. In the first study, a multi-scale bioelectric computational model describing human iPSC tissue-scale membrane voltage potentials ($V_{mem}$) was developed to understand unexplored patterning outcomes when various molecular components of the bioelectric system are altered by culture media. Model simulations accurately predicted multicellular $V_{mem}$ patterns when one or more molecular components were altered, as quantitatively confirmed by a machine learning-based quantitative image pattern similarity analysis. In the second modeling analysis, a genome-scale computational model of the human metabolic network was expanded with additional descriptors to investigate how induced pluripotent stem cells reroute metabolic fluxes and achieved cell growth objectives during cardiomyocyte

differentiation under various culture media compositions. This framework integrated transcriptomic, thermodynamic, kinetic, and proteomic and novel fluxome constraints including transport exchange between the cytosol and extracellular environment. From a comparative analysis across multiple published studies and our own experimental validations, we observed that the combination of novel and previous model constraints was required to replicate experimental media-induced changes in metabolic network dynamics during pluripotency and hiPSC-cardiomyocyte (hiPSC-CM) differentiation. We extended this study to a novel media supplementation condition of glutamine and ascorbic acid and found that experimental extracellular flux assays supported the model-predicted improvements to metabolic respiration of iPSC-derived cardiomyocyte progenitor cells. In summary, these results collectively validate the potential for model-guided media design of engineered living systems using understanding of bioelectric and metabolic systems properties.

# CHAPTER 1. INTRODUCTION

The goal of multi-cellular engineered living systems (M-CELS) is to design and manufacture multi-cellular systems with novel form or function using engineering design principles. These biological systems are composed of individual biological subsystems with self-regulated development. Many robust morphogenic processes, such as embryogenesis and organogenesis, require precisely timed and coordinated cues upon exit from an initially homogenous embryonic stem cell population. The understanding of multi-scale cell- and molecular-level process drivers is a prerequisite condition for integration of intrinsic cellular mechanisms with external signaling cues into defined methodologies to produce novel engineered living biological systems. Induced pluripotent stem cells represent an excellent tool to enable actualization of these design goals because of their intrinsic pluripotent capacity and previously observed recapitulation of various embryogenesis and organogenesis processes. Computational modeling methodologies will be necessary to complement the development of these systems, as they can elucidate intrinsic mechanisms of emergent outcomes.

The **objective** of this work is to utilize computational modeling to understand the multi-scale drivers of multi-cellular bioelectric signaling and metabolic network processes for downstream optimization of cell culture medium composition to engineer desired multicellular emergent process outcomes. The central hypothesis was proper understanding that external signal cues with bioelectric and metabolic cell systems will predicate downstream model-based design of culture media to engineer desired morphogenic outcomes.

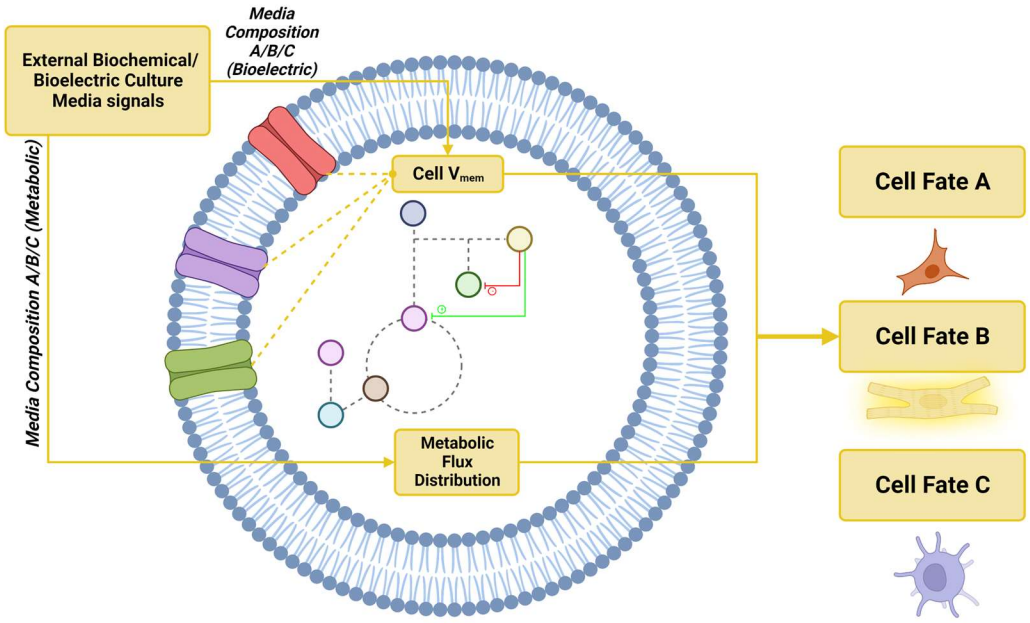


**Figure 1-1.Simplified schematic of the cellular signaling networks analyzed in the study**

I validated my model-based media design approach using confocal microscopy data displaying bioelectric patterning *in vitro* and experimentally derived metabolic network flux data for hiPSCs and intermediate phenotypes through iPSC-CM differentiation. Overall, this work demonstrates the potential of computationally guided M-CELS design and cell therapeutic clinical translation.

## 1.1 Specific Aims

### *1.1.1 Aim 1. Develop multi-scale model framework to accurately predict and design hiPSC emergent bioelectric patterns under differing media condition*

I hypothesized that the integrated ionic transport dynamics defining $V_{mem}$ and cell-cell ion transport dynamics will result in accurate simulation of steady-state spatial bioelectric patterns in vitro when applied to various culture composition contexts.

Supervised machine learning was utilized to elucidate unique local and global spatial features of media-induced bioelectric patterns in hiPSC colonies. Furthermore, particle swarm optimization was utilized to recapitulate needed optimal ionic diffusivity ratios to produce observed target patterns. This methodology reproduced the pre-known values with relatively high accuracy, suggesting that cell culture media could realistically be designed to control multi-cellular signaling and morphogenic processes.

### *1.1.2 Aim 2. Develop mathematical model of the hiPSC metabolic network and determine media conditions that encourage functional and phenotypic maturation of hiPSC-derived cardiomyocytes*

I hypothesized that specific model-based cell culture media formulations/compositions will not only alter cell function but also directly influence phenotypic outcomes of iPSC-CM directed differentiation. Incorporating a bioinformatic-based genome-scale reconstruction of human metabolic network enabled insights into critical media components, metabolic subsystems, and individual reactions that are required to satisfy particular cellular objectives. We found that the model recapitulated critical aspects of experimental metabolic characterizations under defined media conditions and could predict cell metabolic activity under novel, cardiac-promoting culture media conditions.

# CHAPTER 2. BACKGROUND

## 2.1 hiPSC Biotechnology

One of the greatest challenges currently facing biomedical engineering is the lack of resources for cell therapies. This issue arises from an organism possessing an intrinsic capacity to utilize a stem and progenitor cell pool to replace dying cells; these stem and progenitor cells eventually differentiate into cells and tissues that perform specialized functions. Higher vertebrates and mammals possess a limited pool of these specialized cells, directly limiting their regenerative capabilities. Cell and tissue transplantation from other donors or species is a potential solution to this issue, but faces significant drawbacks associated with immunological rejection and consequential functional failure. Cells and tissues sourced from the donor themselves, known as autologous cells and tissues, alleviate this issue but still suffer from short supply. An early solution to this problem was presented with the discovery of stem cells. The term stem cell was first conceptualized in 1870s by the German scientist Ernst Haeckel [1]; he surmised that a 'stem cell' refers to a single parental progenitor cell that originates in the maternal zygote from which all differentiated, specialized cells derive. This characterization was supported by histologist Alexander Maximow in 1909 [2], when he defined stem cells as progenitor/precursors to white and red blood cells, when their bone marrow origin and hematopoietic nomenclature was still unestablished. The stem cell traits introduced with this novel phenotypic classification (multipotency, proliferative capacity) still has highly relevant implications in current biotechnological applications, as hematopoietic stem cells are utilized in cell and tissue transplants as a relatively safe and efficacious source material [3]. However, the discovery of this cell source still did not satisfy the requirements for organ or tissue transplant, as multiple interacting cell types must maintain organization of anatomical structure and resulting function. Furthermore, novel tissues must possess the ability to communicate and

process biophysical and biochemical signals within the host or patient. Thus, further progress in biotherapeutic applications necessitates stem cells to possess a more pluripotent or totipotent-like capacity to satisfy this required phenotypic diversity observed in meso-/macroscopic tissue and organ systems. The arrival of embryonic stem cell technologies in 1981 showed the possibility of maintaining a pool of infinitely expanding stem cells, while possessing the critical ability to differentiate into any specialized mature cell type [4]. The authors dissected embryonic stem cells (ESCs) directly from *in vitro* mouse blastocyst culture and observed differentiation to diverse tissue types upon *in vitro* embryoid body culture. The discovery of human embryonic stem cells occurred 15 years later in [5]; cells were dissected from a fertilized human blastocyst and subsequently cultured *in vitro* on mouse embryonic fibroblast feeder layers. The authors observed differentiation to a variety of extra-embryonic phenotypes when they subjected immunodeficient mice to a teratoma formation assay and spontaneous differentiation when the cells were cultured without a mouse embryonic fibroblast feeder layer and human leukemia inhibitory factor (LIF). However, ethical considerations [6; 7] have severely limited its practical application to cell-based biotechnologies and therapeutics. Many countries and administrations consider ESC use in research to be synonymous with killing; thus, ESC research is treated as a crime and banned in multiple countries.

Due to the above limitations with ESCs, the true therapeutic potential of pluripotent stem cells was realized with the first recorded generation of human induced pluripotent stem cells (hiPSCs) [8], a functionally similar alternative cell source to their human embryonic stem cell (hESC) counterparts. Importantly, these cells can be differentiated to any extra-embryonic lineage, maintain an infinite proliferative capacity, and can be induced from a variety of somatic phenotypes. The authors sought to probe the possibility of nuclear-based cell reprogramming, based on previous experimentally observed evidence that somatic cells have been shown to be amenable to cell nuclear reprogramming via

nuclear content transfer into mammalian oocytes [9] and via fusion with embryonic stem cells [10; 11]. This phenomenon served as the foundation for their hypothesis of key transcriptional causal drivers of somatic cell reprogramming to pluripotency. They surmised that this reprogramming was controlled and maintained by the coordinated activity of multiple transcription factors (TFs), leading to the development of an assay system in which 24 candidate genes were systematically introduced into mouse embryonic fibroblasts via retroviral transduction. They analyzed the transduced cells for embryonic stem cell marker expression and ran functional pluripotency tests, such as the teratoma formation assay and ability to form colonies in culture. They ultimately determined that Oct3/4, Sox2, Klf4, and c-Myc were the critical transcription factors that are required to maintain cell pluripotency. While Nanog has historically been associated with pluripotency maintenance [12; 13], the authors found that it was not a necessary factor to maintain pluripotency. Importantly, this opened the possibility for patients to utilize their own cells and tissues to ensure maximal transplant efficacy and safety. While human iPSCs and ESCs are nearly identical, several molecular differences result in several significant differences in functional capacity. For example, mouse iPSCs performed worse in teratoma assays than their embryonic stem cell counterparts [14]. Furthermore, several studies have shown that human iPSCs possess a decreased propensity to differentiation to neuronal [15], neuroepithelial [14], and hematopoietic lineages [16] when compared to embryonic stem cells from the same species. Many researchers interpret these observations to elucidate an intrinsically lower differentiation capacity hiPSCs relative to hESCs. However, others [15] believe that the decreased differentiation capacity occurs because of donor-specific transcriptional profiles. This notion is supported by experimental cell-of-origin studies, that have shown that parental phenotype-of-origin used to generate iPSCs in fact influences differentiation capacity. For example, Hu et al. [15] found that reprogramming efficiency of hiPSCs derived from retinal-pigmented epithelial (RPE) cells exhibited a significant preference for redifferentiation back to the RPE phenotype in culture once FGF2 was

removed. Ultimately, while hiPSCs and hESCs maintain the same general pluripotent and proliferative capability, the capacity to differentiate may differ between the two phenotypes, with epigenetic drivers from the source patient critically influencing this capacity.

The potential of hiPSC application extends to drug screening as a means for discovering mechanisms responsible for disease progression; for the purpose of this thesis, I highlight notable successes in identifying new therapeutics for cardiac diseases. Animals and animal cells cultured *in vitro* often function poorly in human model drug screening systems, due to multiple existing differences between their physiology and that of their human counterparts. Furthermore, response to drug treatment will differ between species due to genetic makeup, as it is directly tied to physiologic function. Several genetic disorders have been shown to specifically affect the heart, such as familial lethal arrythmias, congenital heart diseases, and familial cardiomyopathy. Tanaka et al. [17] found that ion channel blocker-induced dose-dependent changes in electrophysiological field potential waveform mimicked that of native cardiomyocytes, which suggests the valuable potential for hiPSC-cardiomyocyte (hiPSC-CM) model use in cardiac drug screen and associated electrophysiological characterization. The authors [18] developed a cardiac disease model which incorporates hiPSC cell lines generated from type-2 LQTS patients. These cells possessed a genetic mutation in the KCNH2 gene, which encodes ion channel hERG. Once they subsequently performed a cardiomyocyte differentiation protocol and compared the patient-derived hiPSC-CM electrophysiological profile to that of healthy control cells, the diseased cells generated a prolonged action potential duration. They hypothesized that this functional readout for a genetic defect could provide beneficial for disease treatment planning. Thus, they extended the study to drug screening for potential therapeutic pharmacological agents and found that potassium-channel blocking agents aggravate cells and calcium-channel blockers, late sodium-channel blockers, and $K_{ATP}$-

channel openers provide a therapeutic effect. Moretti et al. [152] probed another ion channel-associated gene that contributes to the type-1 long QT syndrome phenotype, KCNQ1, which encodes a voltage-gated potassium ion channel that repolarizes the cell post-action potential and channel defects. Similar to [18], the authors derived patient-specific hiPSCs and differentiated them to cardiomyocytes, then performed electrophysiological patch clamp, and observed the characteristic prolonged action potential response in diseased cells. In contrast to the hERG study, this screen of hiPSC-derived cardiomyocytes indicated that beta-blockers were the class of compounds that provided the most therapeutic benefit. This is important because both studies reflected similar electrophysiological defects, but the specific causal molecular driver, and associated favorable treatments strategies could not otherwise be determined without risky human clinical trials or expensive animal pre-clinical models.

## 2.2 Engineered Living Systems and Cell Manufacturing

### *2.2.1 Engineering Living Systems*

Morphogenesis is the process by which biological entities, such as cells, tissues, and organisms develop specific forms and functions. In the context of embryonic development and organogenesis, smaller scale morphogenic processes or modulatory drivers produce robust anatomical and functional outcomes despite constantly changing microenvironments and external signaling cues. The robustness of developmental processes suggests that the initial embryonic stem population contains some intrinsic capacity for the constituent cells to interpret spatial/temporal biological signals and communicate them throughout the collective embryonic multicellular system. Heavily inspired by multi-scale component drivers of these emergent processes, “multi-cellular engineered living systems” (M-CELS) is a burgeoning field broadly defined as the design and construction of multicellular systems that produce emergent behaviors with desired

natural or non-natural form/function. The field sits at the intersection of organoid, microfluidic, genetic engineering, biobot, and nanofabrication technologies, and seeks to extend the holistic understanding of complex biological systems to ultimately control both natural and synthetic emergent outcomes.

Aydin et al [19] defined two basic M-CELS research goals: (1) better understand the properties, mechanisms, and dynamics of the composite parts of living organisms [20] and (2) create more efficient, and intelligent biological machines that are capable of dynamic adaption to their environment. Furthermore, they established a set of design principles for future manufacturing of M-CELS devices. These principles may be traced across three representative M-CELS research areas: (1) organoids, (2) microphysiologic systems, and (3) biobots. Biobots have been utilized in biomedical and pharmacology applications and have provided societal benefits in their respective applications. For example, Webster-Wood et al. [21] developed a two-legged biobot attached to aligned cardiomyocytes, which were seeded onto a micropatterned silicon wafer. The device locomotion was actuated by the force of the cardiomyocyte cell layer contraction. Kim et al. [22] extended the design to incorporate micropatterned polydimethylsiloxane (PDMS). This modification effectively increased the device's functional capacity and resulted in six-legged biobots that were capable of functioning over extended time periods (up to 11 days).

Ethical considerations and possible cultural sources of contention are also important aspects of the design process that should be diligently monitored and respected as advances in biotechnology the field continues to expand the use of M-CELS biotechnologies [23]. Furthermore, the design of M-CELS will force us to consider two-level hierarchical frameworks, the first of which being individual subsystems. The defining feature of a M-CELS subsystem is self-regulation, or the ability to attain primary form and function without input or feedback from other sub-systems. The next, higher level involves

systems that develop via integration of multiple modules. The interactions between modules are necessary to induce desired emergent behaviors.

The most familiar example of the first hierarchical level at work is the application of reaction-diffusion principles to Turing patterns and Turing-like patterning mechanisms [24]. A more complex extension of these principles was applied to a bacterial population context [25], where a stochastic activator-inhibitor system was implemented. Groups have also leveraged cell biomechanical properties in the design of self-organizing multicellular systems. [26] combined biochemical and biomechanical self-organizing signal cues to engineer an array of novel patterned structures. An engineered chimeric synthetic Notch receptor was capable of external signaling cues and subsequently transducing downstream transcriptional expression. When the synthetic biologists engineered the transcriptional output to be cadherin expression, cell aggregates gained the ability to self-organize. This occurred because of the differential biomechanical properties afforded to the cells with induced cadherin expression. In related work, Tordoff et al. [153] investigated differential cell-cell adhesion and the principles of biomechanics-based cell sorting by integrating cell sorting relaxation kinetics into their morphogenic study. Their cell system was based on differential cell-cell adhesion and the principles of biomechanics-based cell sorting. They found that by tuning the cell ratio of highly and lowly adhesive cells and cell number, they generated long-lasting patterned self-assembled multicellular structures. These same biomechanics-based cell sorting mechanisms have been exploited in [68] with associated computational modeling-generated insights.

Examples that integrate multiple subsystems together (i.e., the second, higher level of hierarchy) are now discussed. Aydin et al. [19] created a biohybrid machine system in which they attached neuromuscular tissue onto a scaffold body. The scaffold geometry coaxed myoblast differentiation into organized muscle tissue, which was then co-cultured with neural clusters. Functional neuromuscular units emerged as a result, validated by

observed neurite extension, innervation, and communication with muscle tissue. These novel ‘neurohybrid swimming machines’ utilized these engineered neuromuscular tissue constructs to actuate locomotion when subjected to an optogenetic stimulus. In another muscle-related application, Oh et al. [154] co-cultured human pluripotent stem cells (hPSC)-derived sympathetic neuron cells with cardiac muscle cells and observed the development of functional connections between the two phenotypes. Resultant neurons recapitulated the human autonomic neural cell development process, expressed sympathetic neural cell biomarkers, secreted the characteristic norepinephrine hormone, and electrophysiological signals. Interestingly, enhanced neuronal maturation resulted from physical interactions and biochemical communication between the two tissue types. These two examples highlight the potential of M-CELS tissues to induce novel function from biological system interactions, but further tools and methodologies are required to elucidate specific causal drivers of process outcomes. This is especially relevant for mammalian system applications, and the associated complexity and dynamic modes of regulation hamper the standardized production, monitoring, and optimization of M-CELS devices.

### *2.2.2 Cell Manufacturing*

The high-level goals of M-CELS design overlap with those of Cell Manufacturing. The field of cell manufacturing arose from initial cell transplant therapeutic success, and mainly focuses on the large-scale requirement for safe, cost-effective, and readily available cell and tissue therapeutic devices or materials. There are various hurdles associated with each requirement, and field progress depends on the solutions to these issues. Product safety is defined in clinical applications as the requirement for the designed product to not induce harm to the body. One of the biggest hurdles facing this requirement is the immunogenic potential of the introduced cells. In one preclinical study, van Laake et al. [27] transplanted hiPSC-derived cardiomyocytes (hiPSC-CMs) into the myocardium of

immunocompromised mice. Notably, the transplanted cell population was composed of multiple phenotypes and was only ~20-25% cardiomyocytes. However, successful cell integration, phenotypic maturation of the hiPSC-CMs, as well as the loss of stem cell population occurred in the tissue over the course of observation. However, this effect was not long-lasting, as the graft failed 12 weeks after transplantation. In another study [28], hESC-CMs were introduced into a guinea-pig model of myocardial injury and successfully engrafted, along with synchronous contraction with host tissue and protection against arrhythmias.

The previously mentioned studies in smaller animals showing a therapeutic response for the treatment of myocardial infarction (MI) motivated one group [29] to extend hiPSC-CM animal model efforts to large nonhuman animal primate models. The researchers cultured a heterogenous mixture of smooth muscle cells, cardiomyocytes, and endothelial cells in a fibrin scaffold for 7 days under dynamic stimulation and found that the dynamic induced co-culture functional maturation or the differentiated cardiac tissue. They subsequently engrafted the scaffold in a porcine MI model and observed improvements in cardiac function, infarct size, and wall stress. Importantly, no arrhythmogenic complications were observed. Despite these numerous examples of successful integration into *in vivo* animal model studies, most of these animals were immunocompromised. This is a critical point, because immune rejection poses one of the greatest challenges for cell therapies in humans. More specifically, allogenic cell sources face the potential for immune rejection. One group proposed a hiPSC haplobank as a potential solution [30; 31]. Human leukocyte antigen (HLA) matching between patients and donors would alleviate the potential immune rejection; however, this potential solution would require a large donor pool and would require extensive resources. Furthermore, iPSC reprogramming with non-viral vector is preferrable to viral transduction, as viral vectors have the potential to integrate into the recipient genome and harmfully alter

physiology. The development of an effective non-viral approach would tremendously boost cell manufacturing efforts, as Lonza has designed a protocol to produce iPSCs at a clinically relevant scale [32].

The next major hurdle in cell manufacturing is scalability. Potential transplant applications of cell therapies will require vast numbers of generated cells. For example, some estimates suggest that successful transplant injection outcomes require at least 1 billion cardiomyocyte cells [28]. Many early approaches to this hurdle involved the use of bioreactor-based culture systems. Large-scale hiPSCs-CM differentiations have been successfully performed in both 2D [33] and 3D cultures [33]. Furthermore, this same group developed a metabolic-based phenotypic purification protocol to eliminate residual undesired hPSCs from culture and mature remaining CMs. This "lactate purification step" was a very important discovery, as potential cell therapeutic applications often seek to avoid immature populations due to their teratoma-forming potential.

The final hurdle associated with cell therapy-based cell manufacturing efforts is functional efficacy. It is not only critical to replicate desired phenotypes in cell-based therapies, but the utilized iPSC-derived differentiated cells or tissues must behave in a similar manner to their healthy, *in vivo* counterparts. One major hurdle limiting the application of hiPSC-derived cardiomyocytes to clinical applications is the immature electrophysiological characteristics of iPSC-derived cardiomyocytes, which introduces the potential for lethal cardiac arrhythmias. Future field progression and desired clinical translation requires novel solutions to these presented hurdles.

### 2.3 Metabolic and Bioelectric Cell Fate Regulation

The robust patterning and organization achieved during the gastrulation and organogenesis development processes support the notion that cell-level phenotypic trajectories occur due to intrinsic regulatory mechanisms. These regulatory mechanisms

often take the form of transcriptional drivers, but post-transcriptional drivers can also influence emergent behaviors [35]. To truly realize the potential of hiPSC application to M-CELS and cell manufacturing, holistic understanding of these parallel, multi-level regulatory systems must accommodate designs that will inevitably only increase in complexity. This is especially important in the context of hiPSC-CM differentiation, as supportive cardiac stromal phenotypes may help increase differentiation efficacy. Multiple differentiation protocols have been developed for the potential treatment of cardiovascular diseases [36; 37; 38; 39; 40] and take advantage of different signaling cues that replicate *in vivo* developmental processes [41] [42] [36] [43]. One of these protocols [36] involves a precisely timed modulation of the Wnt signaling pathway, and results in high cardiomyocyte yield, as validated by cTnT expression (~80-98%). Despite this impressive yield, these cells still possess an immature phenotype, like that of neonatal cardiomyocytes [155]. Thus, alternative, non-signaling based strategies are required to optimize cell phenotype and functional maturation to realize potential application to cell therapies.

Cell metabolism refers to the set of biochemical reactions responsible for interconverting energy present in food to cell biomolecular building blocks (i.e., proteins, nucleic acids, carbohydrates). These building blocks are produced from the interconverting activity of specific metabolic pathways, and cells possess the capacity to regulate pathway use in accordance with cell needs. For example, rapidly proliferative cells require enhanced nucleic acid production to support DNA synthesis for dividing cells. Cellular metabolism has been shown to indirectly modulate cell phenotypic trajectories in multiple studies. For example, Moussaieff et al. [44] observed that histone acetylation was essential for maintenance of pluripotency and this effect was mediated by glycolysis-associated acetyl-CoA production in mouse and human PSCs. Removal of acetate from culture media induced differentiation and acetate supplementation delayed pluripotency loss and differentiation. Furthermore, Tohyama et al. [45] exploited knowledge of differential

metabolic network composition/topology between hiPSCs and differentiated hiPSC-CMs in the creation of a novel lactate-based media formulation, designed to eliminate residual hPSCs while maintaining differentiated CM progeny. These examples highlight the potential of metabolic-based hiPSC-CM maturation and purification in cell therapeutic applications.

Bioelectric signals refer to information carried between cells and tissues in the form of microscopic and mesoscopic field voltage potentials, ion fluxes and ion concentration gradients. Bioelectric signals have previously been shown to modulate cell-level fate decisions in both cancer [46] and stem cells [47] and tissue-scale anatomical and morphogenic outcomes in multiple development and regenerative contexts [48; 49]. On the single-cell level, proliferative phenotypes are usually relatively depolarized and terminally differentiated cells are usually relatively hyperpolarized. This phenomenon has also been observed in cancer cells, where induced cell hyperpolarization stopped cell proliferation in cancer phenotypes [156]. Interestingly, cell depolarization induced mitotic activity in mature central nervous system (CNS) neurons [157]. The canonical nature of this relationship makes bioelectric signaling an attractive potential control mechanism in both M-CELS and cell manufacturing applications. As previously stated, long-range bioelectric signaling also directly modulates morphogenic process outcomes. Vandenburg et al. [158] found that regions of relative hyperpolarization existing within *Xenopus* embryos serve as bioelectric pre-patterns for downstream eye placement during craniofacial development; if the hyperpolarized regions were extrinsically perturbed downstream eye development would proceed to produce non-natural anatomical outcomes [49]. Similarly, Atsuta et al. [50] found that developing chick and mouse limb buds must maintain a depolarized bioelectric state during the chondrogenesis process; more specifically, they linked bioelectric signaling cues to transcriptional outcomes that explained larger-scale phenotypic and morphogenic trajectories. A specific voltage-gated calcium ion channel,

$Ca_V1.2$, was responsible for this behavior, as $Ca^{2+}$ signaling via $Ca^{2+}$ cytoplasmic influx through the mentioned channel. The authors observed downregulation of many essential genes for chondrocyte differentiation upon application of a L-type voltage-gated $Ca^{2+}$ channels specific blocking agent, supporting the essential role of the channel in morphogenic outcomes. Overall, both bioelectric and metabolic regulatory systems may be leveraged in hiPSC-CM functional improvement strategies, but desired ultimately control depends on holistic understanding of both the system components and the emergent properties that result from their interaction and with the surrounding microenvironment.

## 2.4 Computational modeling of multicellular systems

Recent developments in tissue engineering through control and manipulation of the extracellular environment and/or cell–cell communication have yielded success in producing organoids. These functional microtissues provide attractive platforms for iPSC-derived organ-on-chip screening, interrogation of developmental principles of organization and lineage specification, and may provide a springboard for future engineering of at-scale organs from modular components. To date, the strategies for yielding self-assembled organoids from pluripotent precursors have not been guided by computational prediction or design. Simulation of complex behavior arising in multicellular constructs could provide critical insight in improving reproducibility [51] or guidance toward desired form and function [52] within an experimentally insurmountable search space. Engineering of inducible transcription factors, precise morphogen presentation, and novel biomaterial surfaces provide examples of the numerous potential experimental factors available for deriving organoid systems.

### *2.4.1 Modeling two-dimensional cultures vs. three-dimensional organoids*

Multiple cell types undergo proximal (direct neighbor) and distal interactions from the diffusion of morphogens across tissue scales that affect cell fate decisions. While morphogen reaction-diffusion has long attracted mathematical analysis, other drivers of differentiation, such as mechanosensing, membrane voltage, or gap junction communication, can be interrogated through simulations that uncouple these mechanisms from other environmental cues. Bioelectric gradients can predispose the development of multicellular oscillations or ensemble level behavior within non-excitable tissues [66]. Dynamic gap junction-based transport networks as a function of asynchronous cell cycling have been attributed to multicellular patterning by creating an intercellular flow of small molecules [67]. Each of these modeling examples explored fundamental mechanisms of

cell-cell communication by limiting the scope of the simulations to a single mode of signaling. While the above examples are useful for computational modeling and testing properties of spatial organization or symmetry breaking within a population, a challenge to computationally addressing organoid development lies in its intrinsic complexity, which may not be fully represented in 2-dimensional culture systems. Furthermore, organoid development naturally is a 3-dimensional process. Organoid cultures have been enabled using a variety of methods to leverage surface tension and adhesive forces (or lack thereof) to encourage cell-cell interactions. Consequently, the appropriate computational modeling description must reflect these changes in biophysical forces. Agent-based modeling (ABM) uses autonomous agents to represent cells capable of making independent, context-dependent decisions with respect to their position and state [159]. In agent-based modeling (ABM) of cells attached to a planar surface, a descriptor for colony growth dictates the choice of dividing cells to seek out open surface versus piling up on top of each other. These features are observed to different degrees in various phenotypes and are generated by physical confinement (such as micropatterned areas). In contrast, computational models of 3D organoids require that the cell aggregate volume expands upon cell divisions [53; 54], as the addition of new agents dictates a "jostling" effect outward to maintain the neighbor-to-neighbor distances that are a consequence of Hookean forces between cells. When authors changed a spring constant parameter, they observed that it can result in unique degrees of cellular packing that emulates organoid growth *in vitro*.

### *2.4.2 Understanding Developmental Processes*

Several efforts focusing on cell-cell and cell-environment interactions in the context of organoid development elucidated how molecular regulators of emergence can positively or negatively affect cell fate outcomes, principles that inform fundamentals of developmental biology. We refer the reader to comprehensive reviews [159; 55] that cover a variety of developmental systems modeled through agent-based simulations and the

utility of this modeling approach for integrating the Turing reaction-diffusion phenomenon with positional information. A multipurpose biomechanical modeling platform to study optic cup morphogenesis relied on biophysical laws of mechanical interactions between cells in geometrically confined conditions [56]. This computational modeling approach used experimentally derived physical parameter metrics, such as height, volume, curvature, proliferation/apoptosis rate, to parameterize their model, specifically to replicate a self-invagination morphogenic process and subsequent boundary formation between regions of organizing clusters. The authors successfully simulated the dynamic mechanical bending process that dynamically modulates shape outcomes based on individual cell-cell interactions at the regional interface and the robustness of the spatiotemporal outcomes *in vitro*. Other groups have also attempted to create synthetic emergent multicellular structures or organoids, to functionally improve existing methods and predictively control emergent patterning. Structurally, the formation of sheets, tubes, rings, and other macroscopic forms can be guided by modular building with organoid subunits. For example, kinetic Monte Carlo, lattice-based simulations of multi-aggregate fusion predicted time-evolved configurations that could arise with cell migration and lumen polarization [57]. The use of this lattice-based, stochastic modeling method could provide distributions of collective spatiotemporal behavior from many simulations; however, this study did not evaluate questions of reproducibility or yield from their initialized structures. Additionally, cells have been represented as Voronoi tessellations in computational modeling efforts to describe physics-based self-organization [58].

### *2.4.3 Model Validation*

The utility of computational models is ultimately defined by the extent to which they satisfy initial questions of critical interacting roles of determining morphogenic and functional emergent fates. Several groups developed methods that incorporate time-

resolved experimental datasets and custom image processing algorithms to define emergent dynamics and confirm simulation outcomes. Time-lapse microscopy of mixed cell populations with fluorescent reporters of the phenotype is non-invasive and ideal for monitoring the evolution of patterns [68; 26]. Other validation methods characterize organoids with assays at multiple spatial levels. For example, single-cell biomechanical metrics, such as cell type dependent strain and matrix curvature induction, were determined using particle image velocimetry and droplet contraction assays for parameterization of FEMs [59]. In bioelectric studies, e.g., [60], fluorescent confocal microscopy in parallel with whole-cell patch clamp quantified membrane potential and spatiotemporal spread across multicellular clusters, validated predicted functional features of bioelectric gradients that preceded neural morphogenesis. Furthermore, canonical variate analysis enabled the authors to incorporate unbiased statistical metrics to study differences between control and pathological conditions. Multiple images were selected for biologically relevant morphologic features; the distances between "landmarks" of organ features in tadpoles were quantified by a statistical metric that relates shape differences, Procrustes distances [60]. The resulting scores yielded information on spatial variation across image sets and showed how much a given perturbation changed emergent patterns. Machine learning approaches are rapidly being adopted to facilitate more challenging validation efforts in models of multicellular systems. In Villoutreix et al. [61], the authors created a platform that can handle heterogeneous datasets, meaning that multiple target developmental targets (i.e., gene expression, protein localization, and phosphorylation, and tissue morphogenesis) can be defined as state variables assessed in parallel. Merging state variables in a completion matrix enabled *Drosophila* embryo measurements at distinct timepoints, which

helped them test mechanistic model predictions. Machine learning algorithms were used to fill the missing spaces of the matrix and fully define the multivariate trajectories present within that system. Sparse data matrices are a critical problem in multicellular model validation. Data learning techniques can help to address this problem, improving predictive accuracy. Oyetunde et al. [62] used data learning to improve the predictive power of an underdefined mechanistic genome-scale metabolic model. The large solution space satisfying their physiological constraints did not provide enough insight into optimal bioproduction conditions, so the authors utilized data augmentation and stacked regression techniques to artificially expand their dataset amount and variability. This expanded set was used with ensemble learning techniques to determine the best machine learning approach and critical factors influencing bioproduction. The utility of machine learning techniques is not limited to mechanistic models but also can be incorporated to handle stochasticity. For fitting multicellular patterning outcomes from an ABM of mixed iPSC populations [68], machine learning algorithms were employed in image classification efforts and exploration of the possible parameter solution space. Particle swarm optimization helped pinpoint optimal parameter combinations within a defined experimental design space that produced desired patterns. To match desired *in silico* patterns to experimental data, the authors used Tree Spatial Superposition Logic, a quadtree data structure, to capture detailed local and global spatial relationships in an image [90; 110]. Quantitative measurements of image-image similarity were accomplished by employing a rule-based machine learning algorithm (RIPPER) to give similarity scores to image sets, indicating how strongly simulation patterns correspond to experimentally produced patterns [90; 110].

# CHAPTER 3. IDENTIFICATION OF DISTINCT, QUANTITATIVE PATTERN CLASSES FROM EMERGENT TISSUE-SCALE BIOELECTRIC PROPERTIES OF HIPSCS

## 3.1 Introduction

The advent of induced pluripotent stem cell technologies has facilitated studies of developmental trajectories and multicellular system processes. An initially homogeneous population of hiPSCs represents an ideal system to study and probe development, mimicking embryonic tissue in the ability to differentiate to the three extraembryonic lineages and self-organize into organoid structures in a robust manner [63; 64]. Understanding the interactions between intrinsic biochemical, bioelectric, and biomechanical cues driving multicellular emergent features would enable directed, novel morphogenic trajectories, given the proper tools and biotechnologies [52]. Multi-scale computational model simulations are well-suited for uncoupling roles of specific system components from interactions with other larger- or smaller-scale system components [70; 67] that would be difficult, if not infeasible, to perform experimentally. Previous studies have elucidated individual biochemical and biomechanical spatiotemporal regulators of development through computational modeling [68; 69; 56; 71]. While these modeling and experimental characterizations have successfully addressed individual aspects of biochemical and biomechanical cues [26], analogous hiPSC modeling/experimental

studies of bioelectric signals have been performed. It is known that ion channels, gap junctions, and ion pumps coordinate activities to create and affect cellular membrane voltage potential ($V_{mem}$) and steady-state $V_{mem}$ patterns in interconnected cell clusters of non-excitable cells. Embryonic channelopathies lead to morphological deformities in lower-level complexity organisms, such as *Drosophila* and *X. laevis*, and higher-level complexity mammals, such as chick and human embryos [72]. Computational modeling has already helped to elucidate the role of an ion channel in the emergent bioelectric pre-patterns in other organisms [60]. A study done on multi-scale bioelectric controls of development in lower-complexity species [60] found that spatial long-range $V_{mem}$ gradients were critical 'pre-patterns' for neural crest morphogenesis in *X. laevis* embryogenesis, and the authors established interconnected roles for bioelectric machinery that was responsible for creating and maintaining that pattern. The authors integrated quantitative cell electrophysiological and functional data to parameterize the bioelectric computational model to their specific developmental context and validated the criticality of a particular voltage-gated $K^+$ channel isoform, HCN2. While this study was instrumental in setting a precedent for studying bioelectric signaling in multicellular modeling, subsequent extension to the human developmental processes has not been performed due to the challenges of parameterizing human iPSC ionic flux regulation on more than one level of spatial scale (cellular or subcellular) [73; 74]. Computational simulations of non-excitable cells highlight the critical role gap junctions possess with respect to intercellular coupling and elucidates potential mechanisms by which bioelectric state information propagates from the single- to multicellular scale [66; 70; 75]. The disruption of intercellular communication has been shown to disrupt morphological outcomes in various multicellular

systems [48; 67] and this philosophical view of gap junctions as information processing conduits has experimental support [76]. If we better understood how these signals propagate in human bioelectric multicellular systems, we could possibly engineer specific cell types to occupy specific regions within a cluster and enhance their desired functional characteristics for cell transplants in cell manufacturing and regenerative medicine applications. However, previous characterizations of human electrophysiology have either focused on ion channel expression or whole cell ionic current, while none have focused on multicellular electrophysiology. This knowledge inspired a novel research effort to further understand bioelectric signaling in human multicellular systems across molecular, cellular, and multicellular scales. This holistic system analysis is prerequisite for future bioelectric signal exploitation in synthetic biology and cell manufacturing.

We developed a novel, multi-scale modeling characterization of bioelectric patterning. We parameterized a previously developed physics-based simulation engine, Bioelectric Tissue Simulation Engine (BETSE) [148], in a novel effort to predict hiPSC bioelectric patterns and holistically understand the influence of bioelectric system component perturbations on resulting patterns. The mechanistic model is a bottom-up scheme that utilizes known basic relationships between ion flux, $V_{mem}$, and cell-cell communication to form predictions on the 2-D bioelectric patterns that form from the intrinsic interplay between system components and the external environment under differing monolayer cell culture conditions. Our approach takes advantage of pharmacological compounds, cell culture media alterations, and CRISPRi to influence specific components of the multiscale bioelectric system and experiment- or literature-based characterization of the intra- and extracellular bioelectric environment (Error!

Reference source not found.). Machine learning-based algorithms were trained to identify unique 'rules' that represent spatial features distinct to each bioelectric pattern condition. We report that quantitative image similarity comparisons showed that computational simulations were able to capture specific features of emergent bioelectric patterns under various conditions, and even adequately recapitulate patterns arising from differing cell types exhibiting distinct bioelectric pattern signatures.

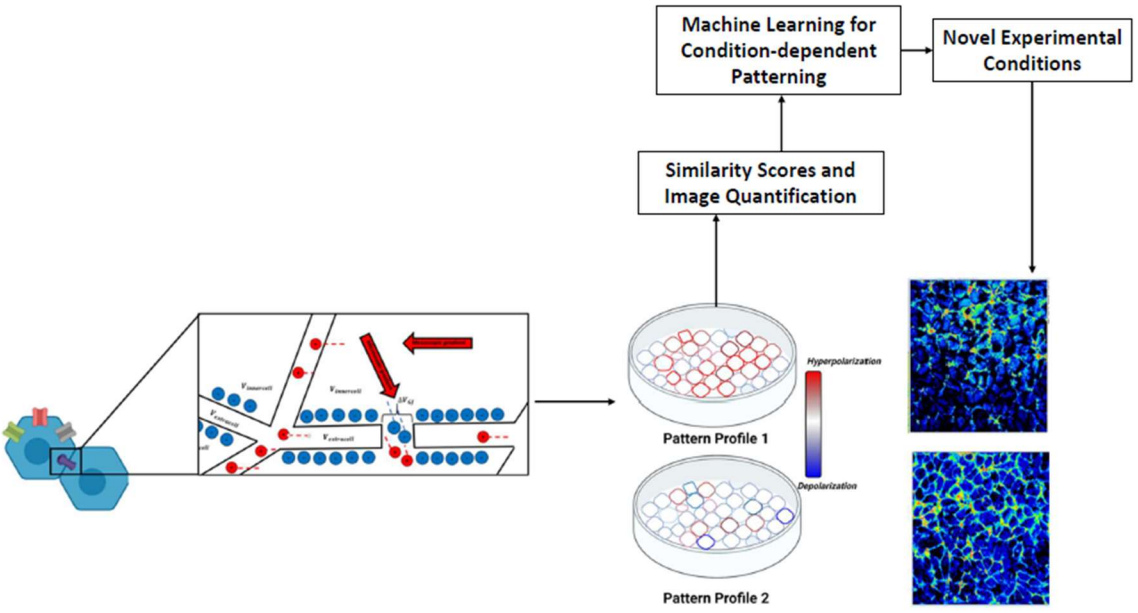


**Figure 3-1. Schematic showing the overall steps taken to predict and control bioelectric patterns. (left) The bioelectric model is populated with hiPSC-specific electrophysiologic data; (bottom, middle) The model was then used to generate predicted bioelectric pattern profiles, which differed based on cell culture conditions. Next, generated pattern profiles were quantitatively compared for similarity against experimentally produced bioelectric patterns under similar cell culture conditions (bottom right). Finally, machine learning was utilized to determine prerequisite system conditions for specific bioelectric pattern feature creation *in vitro*.**

This predictive utility under a variety of simulated contexts supports the approach of this bottom-up modeling characterization for investigating multicellular bioelectrical phenomenon.

## 3.2 Methods

### *3.2.1 Experimental Methods*

#### 3.2.1.1 WTC11 hiPSC cell culture

The human induced pluripotent stem cell line (WTC11, Coriell) was maintained between passages 50 and 70 in GFR-Matrigel coated 6-well plates (Corning). mTeSR PLUS (Stemcell Technologies, Canada) media was used to maintain cells; cells were fed daily until passage (3-4 days), when they were dissociated using Accutase solution and subsequently seeded at 90,000 cells per well (~9400 cells/cm$^2$) or into FluoroDish culture plates (Fisher Scientific) at 100-110,000 cells per well (10,400-11,500 cells/cm$^2$). The cell cultures were incubated at 37 °C and 5% $CO_2$.

#### 3.2.1.2 Contribution of Active Ionic Transport to Steady-state $V_{mem}$ Maintenance

Fluorescence intensity measurements were recorded in unaltered mTeSR (Stemcell Technologies, Canada) control samples and PFA-fixed (4%) iPSCs in mTeSR. Ouabain (Sigma-Aldrich) was then pipetted into the control sample FluoroDish, which binds to the extracellular domain of the $Na^+/K^+$-ATPase $\alpha 3$ helix to inhibit the enzyme's ionic transport activity. The change in fluorescence intensity that accompanied the Ouabain addition was compared against those of the control and depolarized iPSC sample measurements after post-background correction. This allowed quantitative estimation of active transmembrane ionic flux contribution to the establishment and creation of resting $V_{mem}$ in iPSCs and was used in the model parameterization of active ion pump ion flux dynamics in the bioelectric model.

#### 3.2.1.3 DiBAC Confocal microscopy characterization

Initially, cells were grown to 75-90% confluency. Cells were then washed with mTeSR and replaced with a DiBAC-infused media solution and incubated in the dark for 30 minutes. The control FluoroDish received 0.5 $\mu$M DiBAC and PFA-fixed FluoroDishes received concentrations of 0.5, 1, 1.5, and 2 $\mu$M. Multiple ROIs (n≥3) were captured for each plate/DiBAC concentration. ROI confocal images were subsequently exported as TIFF files for downstream image correction and intensity analysis. The method, previously utilized by [160], assumed a direct relationship between $V_{mem}$ and fluorescence intensity given the equilibrium Nernstian charge distribution assumptions of equal intra- and extracellular free dye concentration ([$DiBAC_4(3)$]). Output FIs were exported to Microsoft Excel as .xlsx files.

#### 3.2.1.4 Whole-cell Electrophysiological Patch Clamp of WTC11 hiPSCs

To assess the voltage dependence of transmembrane ionic current density, the cells were seeded on a coverslip, bathed with saline buffer solution in the patch clamp chamber, and perforated with microelectrode pipettes for current or voltage measurement recordings. The gigaseal pipette membrane suction attachment provided the access to the cell interior, thus allowing control of extracellular and intracellular ionic concentrations during an experiment. All recordings were performed in a HEPES buffer solution consisting of (in mM): 120 NaCl, 3 KCl, 1.8 $NaH_2PO_4$, 26 $NaHCO_3$, 2 $CaCl_2$, 2 $MgCl_2$ and 10 dextrose, pH adjusted to 7.4 with NaOH. The internal solution contained (in mM): 120 K-gluconate, 10 HEPES, 10 KCl, 0.2 EGTA, 2 MgATP, 0.3 NaGTP. The patched cell was subjected to a step voltage protocol in which the cell-attached micropipette was increased in a stepwise

manner to varying $V_{mem}$ magnitudes from -70 to 20 mV in 10 mV increments. The measured single-cell current magnitude at each step voltage value was then plotted on a characteristic current-voltage (I-V) graph, which enabled downstream parameterization of the bioelectric model for determination of single-cell $V_{mem}$-dependent transmembrane ionic flux magnitudes.

#### 3.2.1.5 GJA1-modified hiPSC Cell Culture and Experiment Preparation

The LBC2 cell line (parental iPSC) was used as a control and the LBC2-GJA1-CRISPRi cell line (both gifts of Todd McDevitt, Gladstone Institute) were used to investigate perturbed intercellular ion transport in stem cell colonies. The LBC2-GJA1-CRISPRi cells were initially thawed and maintained in Doxycycline-treated mTeSR culture media for 7 days to achieve full GJA1 dCas9 silencing, then subsequently transferred to FluoroDishes for experiment preparation. Both doxycycline-treated and untreated GJA1-CRISPRi cultures were maintained in FluoroDishes (n = 3 dishes per condition) and imaged using the same DiBAC-mTeSR media solution as described above. Untreated GJA1-CRISPRi images were compared to control WTC11 DiBAC image networks downstream for class similarity comparison.

#### 3.2.1.6 Gap Junction Pharmacological Molecule Inhibition

WTC11 hiPS cells were seeded at an initial density of 90,000-110,000 cells per FluoroDish and grown to 80-90% confluency. Cells were then rinsed with mTeSR and subsequently incubated fed with a DiBAC-infused mTeSR media solution (1 $\mu$M), then were incubated in the dark for 30 minutes prior to imaging at 37 °C. PerkinElmer Spinning Disk and Nikon W1 Spinning Disk Confocal microscopes were used to captured DiBAC-

stained cell colony image samples both prior to and 10 minutes following 10 or 60 $\mu$M 18β-Glycyrrhetinic acid (Sigma-Aldrich) media addition. This time interval was chosen to capture cell 2 colonies in the period where the drug molecule maximally exerts its effects on cell-cell current, as previously shown by [84]. After experiment conclusion, images were exported in TIFF format to ImageJ for postprocessing and analysis.

#### 3.2.1.7 K+ supplementation to DiBAC Experiment

WTC11 hiPS cells were seeded at an initial density of 90,000-110,000 cells per FluoroDish and grown to 80-90% confluency. Cells were aspirated and rinsed with dPBS before DiBAC-mTeSR application and incubation. Then, cells were placed in a modified $K^+$-supplemented DiBAC-mTeSR solution and subsequently incubated in the dark prior to fluorescent confocal imaging. The modified media preparation involved initial DiBAC serial dilution to 100x working concentration. However, a separate 100 mM $K^+$-supplemented mTeSR solution was prepared during the second serial dilution step. Subsequent DiBAC-mTeSR solution dilution to the final culture concentration (1 $\mu$M) was combined with the previously prepared 100 mM $K^+$-supplemented mTeSR stock solution in proportion to the final imaging concentrations of 10 and 20 mM [$K^+$]. Cells were then incubated in the dark for 30-60 minutes prior to imaging. All sample images were collected on a Nikon W1 Spinning Disk Confocal Microscope at 60x magnification. Sample images were obtained at different ROIs throughout the FluoroDish and stored for downstream post-processing and image analysis.

#### 3.2.1.8 Immunocytochemistry and imaging

LBC2 and LBC2-GJA1 hiPSCs were grown to 85-90% confluency on FluoroDishes, then fixed for 15 minutes at room temperature with 4% paraformaldehyde (Electron Microscopy Sciences). Fixed colonies were subsequently washed 2 times with dPBS. Colonies were then blocked and permeabilized in 1X PBS and 0.3% Triton X-100 (Sigma-Aldrich) and 5% Normal Donkey Serum (Sigma-Aldrich) for 60 minutes at room temperature. hiPSC colonies were subsequently incubated with primary antibody Cx43-CST (Sigma-Aldrich) in a 1X PBS blocking buffer solution with 0.3% Triton X overnight at 4 °C. The following day cells were washed with PBS 2 times, then were incubated with secondary antibody solution of goat anti-rabbit Alexa Fluor 647 (Thermo Fisher Scientific, 1:200) in antibody dilution buffer for 60 minutes in the dark at room temperature. The colonies were then counterstained with Hoeshst 33342 for 5 minutes before samples were transported to the confocal microscope (Nikon W1 Spinning Disk Microscopy) for imaging. All images were taken at 60x magnification.

### *3.2.2 Computational Methods*

#### 3.2.2.1 Computational bioelectric model framework

The model is designed to simulate bioelectrical patterns that arise from single-cell bioelectric dynamic parameters implemented in a multicellular colony. Modeling simulations are performed in the computational platform, Bio-Electric Tissue Simulation Engine (BETSE) [148]. Ion fluxes are generated by transmembrane transport via ion channels and active pumps. The combined action of fluxes shown above leads to changes in individual cellular spatial ion concentrations. The fundamental charge property of the modeled ions assumes an accompanying change in spatial intracellular charge density and

ionic current density ($\vec{J}$). The model assumes "passive electrodiffusive mass transport" that can utilize three distinct pathways: ***(1) transmembrane:*** via intra- and extracellular spaces across the plasma membrane; ***(2) intercellular (GJ):*** between cellular spaces via gap junctions; and ***(3) extracellular:*** within the global environment and extracellular spaces. The model's mathematical strategy incorporates electrochemical mass transport biophysical characterizations to describe how ions move within a multicellular cluster. Passive electrodiffusive ionic flux is mathematically characterized by the Goldman–Hodgkin–Katz Flux equation (GHK Flux equation), where electric field-mediated flux between local intra- and extracellular spaces dictates spatiotemporal ion dynamics**.** Changes in concentration are determined by assuming the concentration change in an ion *i* depends on the divergence of the net ($\Phi_{Total,i}$) sum of all fluxes of the ion entering or changing in a particular region of the space (i.e., cells or environment).

$$I_{Total} = \sum F z_i \Phi_i = I_{pump} + I_{Na+} + I_{K+} + I_{Cl-} \tag{3.1}$$

This characterization of whole–cell ionic current as a summation of individual ionic contributors has been explored and experimentally validated in a study from [82]. This assumed structure suggests that experiments aimed at specific knockdown/inhibition of the involved ionic currents can elucidate the magnitude of each component to whole-cell current dynamics at resting $V_{mem}$ and other physiologically relevant $V_{mem}$s (-70 to +20 mV). This relation importantly allows for precise and easy transformation between experimentally measured and *in silico* ion currents.

#### 3.2.2.2 Estimated single-ion flux contribution

The relative contribution of $I_K$, $I_{Na}$, $I_{GJ}$, and $I_{pump}$ at a $V_{mem}$ was estimated via linear regression; specifically, $K^+$-ion flux was assumed to be the difference between measured transmembrane ionic current density and simulated collective passive $Na^+$ and Cl- ion fluxes, $Na^+/K^+$-ATPase associated active ion fluxes, and averaged gap junction ion flux ion fluxes at each holding potential or simulated $V_{mem}$ value. These particular measurements differ from the conventional procedure in its utilization of varying external and internal buffer solution compositions. For example, the role of $K^+$ was determined in preliminary experiments by replacing it with N-methyl-D-glucamine in the external buffer solution and comparing control current measurements to measurements under the altered buffer conditions. These current estimates are used downstream in parameterization of permeability values ($P_i$) for each substituted ion.

#### 3.2.2.3 Experimental Image Transformation and Analysis

To convert the DiBAC experiment output images to grayscale bioelectric cell pattern representations, we initially performed background and noise correction on raw image data in ImageJ. Corrected images were subsequently exported to CellProfiler, where they underwent a fluorescence intensity-based transformation procedure. The cells were identified as objects within each image, based on the fluorescent labeling of the cell lipid membrane bilayer. Specifically, a custom script used the roughly circular cell fluorescent border to mark the boundary of a particular cell object and the enclosed region represented the cell interior. Next, cell objects were expanded until touching adjacent cell object borders and calculations were performed over the encompassed cell object region and normalized by cell circumference to obtain a normalized cell fluorescence intensity value; this value represented the quantitative cell $V_{mem}$ observation. A grayscale colormap was

applied to the resultant image to identify cell $V_{mem}$ state, synonymous to the manner in which BETSE output image cell $V_{mem}$ is visually defined. Finally, transformed grayscale images were autoscaled to image minimum and maximum pixel intensities and exported for downstream quad-tree decomposition and pattern analysis.

#### 3.2.2.4 Computational Simulation Image Analysis

Simulation-generated output pattern images were cropped to exclude x/y-axes and scale bars and to only include square cell cluster ROIs. Additionally, auto-scaled colormap settings were chosen for each generated pattern image; this was done to ensure a standardized format between the *in silico* and *in vitro* domains and to elucidate distinct local and global pattern features that may be otherwise lost. Simulated image sets were stored in directories labeled in accordance with the simulated cell culture condition for downstream quad-tree decomposition, pattern identification, and quantitative pattern similarity comparison.

#### 3.2.2.5 Model Core Mathematical Strategy

BETSE utilizes a Voronoi diagram-based cell grid to define cells as irregularly shaped objects, nested within a square environmental grid. This hierarchical arrangement provides flexibility in cell morphology while the grid provides the basis for a Cartesian-like reference coordinate frame. Each cell modeled contains an identifying centerpoint, where scalar parameters (i.e. $V_{mem,intercellular}$ and [ion species]) are defined for the object. The Voronoi diagram-based cell representation allows individual membrane segments to be assigned values for cell perimeter and volume. Furthermore, the membrane segments possess defining tangent and unit vectors at their midpoint, where cell scalar and vector

properties are defined. This enables $V_{mem}$ to be defined for each unique membrane segment. The membrane segment midpoints interface with the environmental grid to enable the use of a nearest-neighbor interpolation function. A weighing function counts the number of membrane segments per environmental grid square in a given region and quantitatively assesses a mole fraction for mass transfer between the cell and environment. This is done to prevent the system from violating charge and mass distribution physical laws.

*Gradient ($\nabla s_j$)* – measures amount of change in some property over space at a specific point (j).

*Divergence ($\nabla \cdot F \rightarrow_j$)* – measures change in flux (outward or inward) of a vector field from a spatial point (j); essentially assigning each point a designation as a source or sink.

*Laplacian ($\nabla^2 s_j = \nabla \cdot \nabla s_j$)* – measures divergence of a gradient of some scalar property (relating $V_{mem}$ to ionic charge density via Poisson's Equation). Standard finite volume method techniques were utilized to solve discrete versions of the divergence, gradient, and Laplacian/inverse Laplacian operators and differential expressions for ion flux on both cell and environmental grids. Then, each core operator was integrated into differential expressions defining bio-electrochemical mass transport. Ion transport was assumed to be influenced by both ion concentration gradients ($\nabla c$) and local or global voltage potential gradients ($\nabla V$) in a transport phenomenon known as electrodiffusion. In general, the process can be mathematically characterized via the Nernst-Planck flux expression:

$$\frac{dc_i}{dt} = \nabla * (D_i \nabla c_i + \frac{D_i z_i q}{k_B T} \nabla V - \vec{u} c_i) \tag{3.2}$$

where *u* represents osmotic fluid flow [162], q represents the charge constant for electrons, $k_B$ is the Boltzmann constant, and *T* is the temperature in Kelvins. Alternatively, the GHK flux equation [161] can be utilized to estimate individual ionic transmembrane currents, as shown below:

$$\Phi_i^{mem} = \frac{z_i V_{mem} F P_{i,mem}}{RT}\left(\frac{c_i^{cell} - c_i^{env} exp\left(-\frac{z_i V_{mem} F}{RT}\right)}{1 - exp\left(-\frac{z_i V_{mem} F}{RT}\right)}\right) \quad (3.3)$$

The collective $K^+$, $Na^+$, and $Cl^-$ $\Phi_{memi}$ voltage-dependent currents, and active ion pump flux ($\Phi_{pumpi}$) and intercellular gap junction currents ($\Phi_{gji}$), establish voltage-dependent transmembrane ion flux dynamics, as shown below:

$$\Phi_i^{tot} = \Phi_i^{mem} + \Phi_i^{gj} + \Phi_i^{pump} + \Phi_i^{channel} \quad (3.4)$$

*GJ Ion Flux Parameters (general)*

$$\Phi_i^{mem} = \frac{z_i V_{mem} F P_{i,mem}}{RT}\left(\frac{c_i^{cell} - c_i^{env} exp\left(-\frac{z_i V_{mem} F}{RT}\right)}{1 - exp\left(-\frac{z_i V_{mem} F}{RT}\right)}\right) \quad (3.5)$$

BETSE Parameter and WTC11 Parameter Values and Derivation

*GJ Ion Flux Parameters*

$$I_{GJ,i} = (P_{GJ} * bloc * \beta_{GJ}^{o}) z_S^2 \frac{V_{mem} F^2}{RT} \frac{[Ion]_i - [Ion]_{i,neighbor} exp\ (-\frac{z_S V_{mem} F}{RT})}{1 - exp\ (-\frac{z_S V_{mem} F}{RT})} \quad (3.5)$$

where block or open % determined by [79] conductance-regulating parameters. Steady-state gap junction conductance is defined below:

$$g_{SS} = \frac{g_{max} - g_{min}}{1 + exp\ [A * (V_j - V_0)]} + g_{min} \quad (3.6)$$

where $g_{max/min}$ is the max/min value that can be reached given high $V_{intercell}$, $g_j$ is gap junction instantaneous series conductance, $V_0$ is the voltage at which conductance is halfway between its minimum and maximum values, $g_{SS}$ represents steady-state conductance value, and $A$ is the constant for voltage sensitivity.

$$g_j = g_{SS} + (g_0 - g_{SS}) exp\ (-t/\tau) \quad (3.7)$$

where $\tau$ is a time constant and $g_0$ is the initial conductance value of the gap junctions. Normalized steady-state conductances were calculated by utilizing open and close rates $\alpha$ and $\beta$.

$$\alpha = \lambda * exp\ [-A_\alpha * (V_j - V_0)] \quad (3.8)$$

$$\beta = \lambda * exp\ [A_\beta * (V_j - V_0)] \quad (3.9)$$

where $A_{\alpha/\beta}$ represent open and close voltage sensitivities, $\lambda$ represents a magnitude scaling parameter, $\alpha/\beta$ represent the channel open/close rates, and $\beta$ was set to asymptotically approach a maximum value of 20/sec, which ensures a situation in which calculated current pulse responses demonstrating exponentially increases terminal phases does not occur. $\beta'$ is a correction factor that prevents $\beta$ from exponentially increasing at large $V_j$ values.

$$\beta' = \frac{\beta}{1 + 50\beta} \tag{3.10}$$

In accordance with experimental data provided from [85], we iteratively simulated 25 and 75% cell-cell ion flux inhibition (or more simply put relative channel block strength) conditions. Furthermore, we set voltage sensitivity parameters in accordance with Cx43s from [109]. The Boltzmann sigmoid used to represent voltage-dependent steady-state gating was fit to the [79] representation (Equations 5-13b).

$\beta$-GA effect estimation

The addition of $\beta$-GA was approximated by a 25 or 75% magnitude reduction in cell-cell ionic conductance; this approximation was applied because $\beta$-GA has been shown to partially inhibit cell-cell ionic conductance in adjacent cells [92; 93]. In these studies authors observed no change to the shape of the bell curve defining transjunctional voltage-dependent current transfer, so the only parameter changed from the initial settings is the surface area as a fraction of cell membrane surface area ($\beta_{GJ}^{o}$). The original value (1e-7) was adjusted to 25 or 75% of the difference between the original value and the completely closed value (1e-9).

*25% magnitude reduction*

$$[(1 * 10^{-7}) - (1 * 10^{-9})] * (.75) = 7.425 * 10^{-8} \quad (3.11)$$

$$(1 * 10^{-9}) + (7.425 * 10^{-8}) = \beta_{GJ}^{o} = 7.525 * 10^{-8} \quad (3.12)$$

*75% magnitude reduction*

$$[(1 * 10^{-7}) - (1 * 10^{-9})] * (.25) = 2.475 * 10^{-8} \quad (3.13)$$

$$(1 * 10^{-9}) + (2.475 * 10^{-8}) = \beta_{GJ}^{o} = 2.575 * 10^{-8} \quad (3.14)$$

*Single-ion flux parameters*

$$(1 * 10^{-9}) + (2.475 * 10^{-8}) = \beta_{GJ}^{o} = 2.575 * 10^{-8} \quad (3.15)$$

The permeability is the adjustable parameter used to control voltage-dependent ionic flux; these values have been matched to our in-house whole-cell patch clamp data.

*Na+/K+-ATPase*

The $V_{mem}$-dependent $Na^+/K^+$-ATPase pump rate was estimated, based on the previous characterization by [82]. The $Na^+/K^+$-ATPase pump Gibbs free energy ($\Delta G_{pump}$) formula is shown below:

$$\Delta G_{pump} = \Delta G_{ATP}^{0} + RT * ln\,(Q) - FV_{mem} \quad (3.16)$$

where $\Delta G^0_{ATP} = -36e^3 \frac{J}{mol}$ represented standard free energy for the ATP hydrolysis reaction, $Q$ represented the reaction quotient, and $F$ is Faraday's constant.

$$Q = \frac{[ADP_{cell}][Pi_{cell}][Na_{env}]^3[K_{cell}]^2}{[ATP_{cell}][Na_{cell}]^3[K_{env}]^2} \tag{3.17}$$

where $Na_{env}$ and $Na_{cell}$ represent cell and environmental sodium concentrations, $K_{env}$ and $K_{cell}$ represent cell and environmental sodium concentrations, and $ADP_{cell}$and $ATP_{cell}$ as cell ADP and ATP concentrations.

$$K^{eqm}_{NaKATP} = exp\ exp\left(\frac{-\Delta G^0_{ATP} + FV_{mem}}{RT}\right) \tag{3.18}$$

where $K^{eqm}_{NaKATP}$ represents the Na+/K+-ATPase reaction equilibrium constant.

$$\Phi_{NaKATP} = \Phi^{max}_{NaKATP}\left(r_f - \frac{Q}{K_{eqm}} r_r\right) \tag{3.19}$$

where $\Phi^{max}_{NaKATP}$ represented the max pump rate, which we estimated from the values provided in [82], $r_f$ represented forward reaction pump rate constant, and $r_r$ represented reverse reaction pump rate constant.

$$r_f = \frac{\frac{cATP}{K_{ATP}}\left(\frac{cNa_{in}}{K_{Na}}\right)^3\left(\frac{cK_{out}}{K_K}\right)^2}{\left(1 + \frac{cATP}{K_{ADP}}\right)\left(1 + \left(\frac{cNa_{in}}{K_{Na}}\right)^3\right)\left(1 + \left(\frac{cK_{out}}{K_K}\right)^2\right)} \tag{3.20}$$

where $K_K = 0.2\ mol/m^3$, $K_{Na} = 5\ mol/m^3$, $K_{Cl} = 1.0\ mol/m^3$ represent chloride, potassium, and sodium rate constants.

$$r_r = \frac{\frac{[ADP]}{K_{ADP}}\frac{[Pi]}{K_{Pi}}\left(\frac{[Na_{out}]}{K_{Nao}}\right)^3\left(\frac{[K_{in}]}{K_{Ki}}\right)^2}{\left(1+\frac{[ADP]}{K_{ADP}}\right)\left(1+\frac{[Pi]}{K_{Pi}}\right)\left(1+\left(\frac{[Na_{out}]}{K_{Nao}}\right)^3\right)\left(1+\left(\frac{[K_{in}]}{K_{Ki}}\right)^2\right)} \tag{3.21}$$

where $K_K = 0.2\ mol/m^3$, $K_{Na} = 5\ mol/m^3$, $K_{ATP} = 0.15\ mol/m^3$, $K_{ADP} = 1.0\ mol/m^3$, $K_{Pi} = 1.0\ mol/m^3$, $K_{Nao} = 140.0\ mol/m^3$, $K_{Ki} = 120.0\ mol/m^3$ represent reaction rate constants [87].

WTC11 hiPSC parameters

The hiPSC steady-state ionic diffusivities were set in accordance with $K^+$:$Na^+$:$Cl^-$ diffusivity ratios reported in [82] and target $V_{mem}$ values of -40 and -60 mV.

hiPSC ionic profile 1:

$$D_{mem_{K+}} = 1.274 * 10^{-17}\ m^2/s$$

$$D_{mem_{Na+}} = 4.478 * 10^{-1}\ m^2/s$$

$$D_{me\ _{Cl-}} = 1.973 * 10^{-19}\ m^2/s$$

hiPSC ionic profile 2:

$$D_{mem_{K+}} = 2.7438 * 10^{-17}\ m^2/s$$

$$D_{me\ _{Na}} = 4.478 * 10^{-18}\ m^2/s$$

$$D_{mem_{Cl}} = 1.973 * 10^{-1} \ m^2/s$$

WTC11-specific voltage-gated K+ ion channel parameters

$$P_i^{channel} \sim g_k = (m_\infty - m)/(m_\tau) \tag{3.22}$$

where

$$m_\infty = \frac{1}{1 + \exp\left(\frac{V_{mem} - (-30)}{-14.7}\right)} \tag{3.23}$$

$$m_\tau = \frac{1}{1 + \exp\left(\frac{V_{mem} - (-46.56)}{-44.14}\right)} \tag{3.24}$$

$$g_{K+,max} = 6.71 * 10^{-16} \frac{m^2}{s}$$

**Table 3-1. Main Bioelectric Model Parameters**

| Parameter | Description | Typical Value | Units |
|---|---|---|---|
| $i$ | Ion index (i=Na, K, Cl, Ca, H, M) | | |
| $D_{o_i}$ | Free diffusion coefficient for ion i | $1.0 * 10^{-9}$ | $\frac{m^2}{s}$ |
| $t$ | Time | 1-10 | s |
| $x, y$ | Spatial coordinates | 500 | $\mu$m |
| $h$ | System height | 10 | $\mu$m |
| $\Delta G^o_{ATP}$ | Standard free energy of ATP hydrolysis | 37 | kJ/mol |

| | | | |
|---|---|---|---|
| $T$ | Temperature | 310 | K |
| $F$ | Faraday's constant | 96,485 | C/mol |
| $R$ | Ideal gas constant | 8.3145 | J/K mol |
| $q$ | Electron charge constant | $1.6 * 10^{-19}$ | C/ion |
| $k_b$ | Boltzmann constant | $1.38 * 10^{-23}$ | J/K |

Table 3-2 (cont'd)

| | | | |
|---|---|---|---|
| $v_{cell}, v_{ecm}$ | Cell and extracellular | $7.85 * 10^{-16}$ | $m^3$ |
| $\sigma_{cell}, \sigma_{mem}, \sigma_{ecm}$ | Cell, membrane and extracellular surface area | $3.14 * 10^{-10}$ | $m^2$ |
| $c_{mem}$ | Membrane capacitance | 0.022 | F/$m^2$ |
| $c_{self}$ | Electrolyte-induced self-capacitance | 0.86 | F/$m^2$ |
| $\alpha_{pump}$ | Max rate constant for pump | $2.0 * 10^{-7}$ | 1/s $m^2$ |
| $v_{\frac{1}{2}^{GJ}}$ | GJ voltage-gating half-closed parameter | 50 | mV |
| $d_{mem}$ | Cell membrane thickness | $7.5 * 10^{-9}$ | m |
| $d_{gj}$ | Intercellular spacing | $26.0 * 10^{-9}$ | m |
| $\mu$ | Water viscosity | $5.0 * 10^{-3}$ | Pas |
| **Variable** | **Description** | **Typical value** | **Units** |
| $c_{i_{ext}}$ | Extracellular concentration | 1 - 150 | $\frac{mol}{m^3}$ |

| | | | |
|---|---|---|---|
| $c_{i_{int}}$ | Intracellular concentration | 1 - 150 | $\frac{mol}{m^3}$ |
| $D_{mem_i}$ | Membrane diffusion coefficient for ion i | $1.0 * 10^{-18}$ | |
| $P_{mem_i}$ | Membrane permeability for ion i | 0.13 | nm/s |
| $V_{cell}, V_{env}$ | Voltage in cell and environment | -10 to -80 | mV |
| $V_{mem}$ | Cell transmembrane voltage potential | -10 to -80 | mV |
| Table 3.1 (cont'd) | | | |
| $\overrightarrow{\Phi_i}$ | Mass flux of ion i | 1.0 | $\frac{\mu mol}{s - m^2}$ |
| $\rho_e$ | Ionic charge density | 600 | $\frac{\mu mol}{s - m^2}$ |
| $\vec{J}$ | Ionic current density | 10-500 | $\frac{C}{m^3}$ |
| $\beta_{GJ}^o$ | GJ diffusion scaling-coefficient | $5.0 * 10^{-7}$ | |
| $\beta_{TJ}$ | TJ diffusion scaling-coefficient | $1.0 * 10^{-7}$ | |
| $D_{NaV}, D_{KV}$ | Max membrane diffusion for voltage-gated channel | $1.0 * 10^{-14}$ | $\frac{m^2}{s}$ |
| $\vec{E}$ | Electric field | $1.0 * 10^5$ | V/m |

*Image Analysis pipeline extended*

CellProfiler (http://cellprofiler.org/) was utilized to transform experimental DiBAC fluorescent images into a grayscale recapitulation. The pipeline initially utilizes a cell

masking function to identify cells for later identification as objects. Then, those objects are expanded to create adjacent boundaries. Next, infinitesimal fluorescence intensities (FIs) measured over the object area, summed, and divided by cell area; the resultant quantity was an averaged object FI value per cell. This FI served as a directly proportional qualitative metric to average cell $V_{mem}$. This method of initial transformation was done to ensure qualitative proximity to BETSE output images. The resultant grayscale images are exported to python for further image processing. The images were initially loaded as NumPy arrays, which are amenable to a variety of colormaps. An RGB colormap is customized to have 3 discrete bins that separate colors and their respective intensities. This bin breakdown is used for both *in vitro* and *in silico* images for standardization of use in the downstream image quad-tree decomposition and analysis.

## 3.3 Results

### *3.3.1 A Human iPSC-Specific Bioelectric Computational Model*

We initiated our model development by focusing on the lower-scale components of the multicellular bioelectric system. More specifically, we sought to first identify each molecular component's hiPSC-specific $V_{mem}$-dependent ion flux activity. For non-excitable stem cells, the critical determinants of cellular resting $V_{mem}$ are ion channels, gap junctions, and ion pumps, and multiple studies [77; 74; 79] have experimentally validated these system components coordinating their activities to create and maintain cell resting $V_{mem}$ state. We hypothesized that this conserved single-cell bioelectric system relationship would also extend to multicellular system dynamics via intercellular conduits. Specifically,

single-cell states have been shown to directly influence the $V_{mem}$ of neighboring cells via gap junctions, thereby influencing the development of 'long-range' voltage gradients across multicellular clusters or tissues, ion fluxes, and ion concentration domains [80; 49; 163] both *in vitro* and *in vivo*. However, both levels of ion channel and connexon expression and functional capacities differ for both specific species and physiological niches, making efforts to create an all-inclusive non-excitable bioelectric model infeasible. Thus, we started the hiPSC-specific bioelectric system model with a holistic single-cell bioelectric characterization based on transcriptomic, electrophysiological, and literature-based data, inspired by the fact that multiscale physics modeling can capture these dynamics at all three levels for a particular species or phenotype if its representative system component characteristics are accurately depicted mathematically (i.e. mathematical representation of ion transporter dynamics and their associated $V_{mem}$-dependence). Bioelectric Tissue Simulation Engine (BETSE) has been applied in previous top-down computational bioelectric system characterization involving bioelectric pre-patterns preceding frog neural crest development [60], which enabled elucidation of an ion channel that is critical for both single-cell hyperpolarization and multicellular bioelectric electric field gradient maintenance. Importantly, this effort was made possible by *a priori* knowledge of (species) cell spatial distribution and cell subpopulation bioelectric properties. In contrast, hiPSC-specific bioelectric characterizations have been sparse in literature and are usually limited to transcriptomic or cellular patch-clamp electrophysiologic characterization [73; 74]. Therefore, we sought to combine single-cell RNA sequencing hiPSC characterization with whole-cell electrophysiologic patch-clamp measurements and literature-derived gap junction bioelectric activity characterization to

parameterize BETSE with hiPSC-specific bioelectric data prior to predictive simulations. Multiple ionic currents ($K^+$, $Na^+$, $Cl^-$, gap junction, $Na^+/K^+$-ATPase) collectively comprise and control whole-cell current; these individual ionic currents not only regulate $V_{mem}$ but are themselves regulated by $V_{mem}$ (**Figure 3-2B**). The resulting interdependency (feedback) between membrane potential and ionic currents and introduced non-linear system dynamics is a distinguishing feature of BETSE that makes it conducive to insights gained from multicellular simulations. Furthermore, gap junction-mediated intercellular communication enables neighboring cells to influence each other's $V_{mem}$ dynamics. BETSE's model architecture also enables data-driven gap junction bioelectric dynamics and integrates this behavior with the previously mentioned cellular system dynamics to model this complex phenomenological aspect of bioelectric system dynamics. Therefore, the model is uniquely structured for bioelectric pattern predictions, similar to the manner in which accurate electrical circuit component characterization enables predictive mathematical characterizations of downstream circuit steady-state behavior. The following section describes how experimental outcomes have been used to derive critical hiPSC-specific sub-cellular and single-cell model parameters.

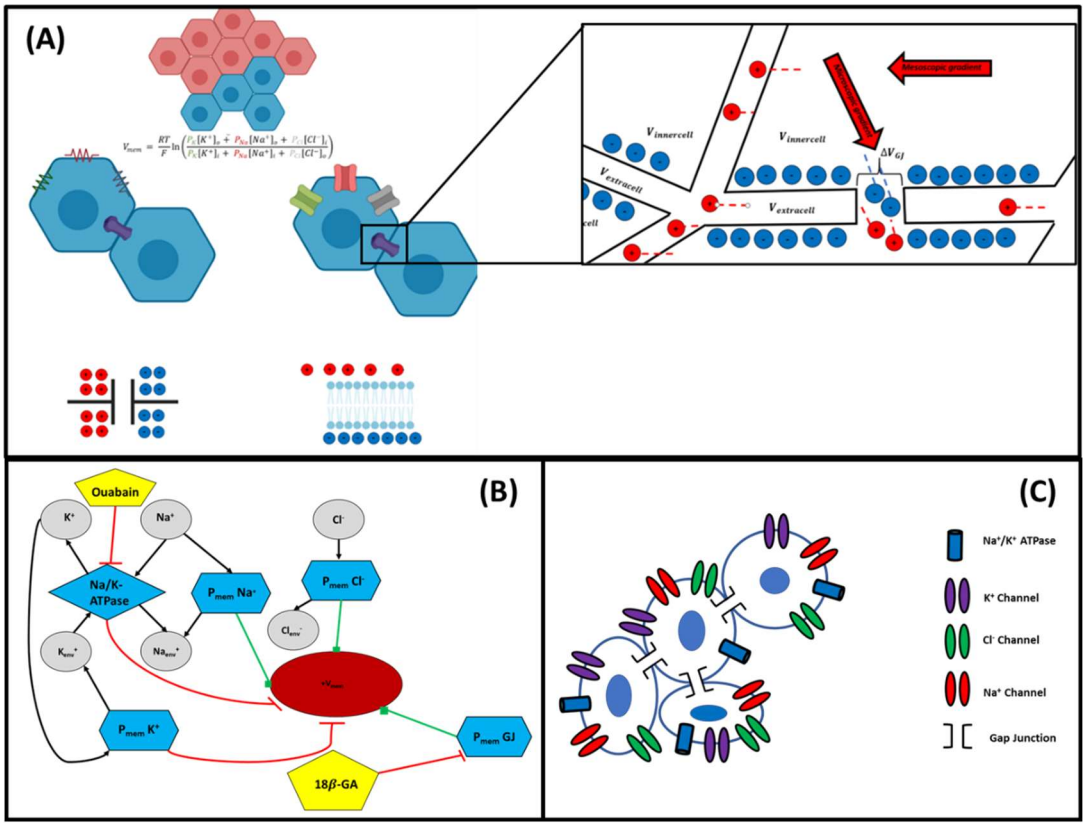


**Figure 3-2. Schematic showing the core components of the bioelectric computational model interacting to create multicellular bioelectric patterns. (A) The bioelectric model components behave similarly to the components of an equivalent electrical circuit; (B) The bioelectric system component schematic shows mode of regulation with respect to $V_{mem}$; specific mechanisms of system perturbation and the resultant effect on cellular $V_{mem}$ are indicated by yellow pentagons and red/green edges, respectively; (C) the main components that comprise cellular $V_{mem}$ *in vitro* and *in vivo* are shown.**

Single-cell model bioelectric component dynamics were constructed piecewise from the available literature concerning each component's $V_{mem}$-dependent ionic transport properties [81]. Previous studies have utilized whole-cell patch clamp voltage-clamp assay measurements to identify and quantitatively estimate individual ionic currents elicited from the cell [82; 83]. Briefly, they substitute ions in the external media solution with neutral or oppositely charged replacements to quantify contributions to resting $V_{mem}$ at differing voltages and found the resulting totality of the currents ($K^+$, $Na^+$, $Cl^-$, and $Na^+/K^+$-ATPase) to equal the whole-cell ion flux. We extended this logic to our single-cell hiPSC model parameterization. At the single-cell level, the computational recapitulation of the whole-

cell step voltage protocol should accurately estimate the whole-cell currents elicited at different resting $V_{mem}$ values as a result of collective subcellular/cellular system component ion fluxes. The Na+ and Cl- ionic currents are defined with passive diffusion-based voltage-dependent behaviors, but the K+ ion flux is modeled to fit the missing ion magnitude that would create alignment between the BETSE and experimentally produced hiPSC current-voltage (I-V) curve via linear regression (Error! Reference source not found.). We justified this assumption because K+ voltage-gated ion channels showed physiologically relevant levels of expression with respect to the other main ionic components' respective channel expression levels (**Figure A 2**). The cells form dynamically interacting networks due to the ability to form cell-cell gap junction pathways; therefore, we investigated the most abundant and functional gap junction expressed in human embryonic development, Connexin 43 (Cx43) [84] (**Figure A 3**). We estimated hiPSC intercellular ion conductance dynamics based on dual-cell patch clamp characterizations [85] and fit Na+/K+-ATPase maximum reaction rates to published conductance values [86; 87]. Finally, we parameterized the model external conditions to mimic the ionic composition of mTeSR cell culture media, completing the environmental, electrophysiologic, and transcriptomic definition of the 'hiPSC-specific' bioelectric environment. We next defined specific culture conditions amenable to simulation and designed to predictably alter specific components of the bioelectric system. The previously defined system conditions characterized the baseline 'Control' culture condition in which the mTeSR culture media is unaltered. The media addition of a specific pharmacological gap junction blocker defined two simulated culture conditions: one condition for 25% gap activity inhibition and another for 75% activity inhibition. Finally, the media addition of

10- and 20-mM $K^+$ salt formed two simulated culture conditions. The comparison between simulated and experimental image domains was facilitated by $DiBAC_4[3]$ experimental confocal microscopic assays [88]. The anionic fluorophore partitions the cell membrane leaflets in accordance with cell membrane depolarization or hyperpolarization, enabling steady-state qualitative observation of both cellular and multicellular $V_{mem}$ patterns. The dye possesses the advantage of minimal interference with cellular processes and no induced cytotoxicity; furthermore, $DiBAC_4[3]$ enables the non-invasive observation of long-term bioelectric pattern behaviors and subcellular resolution micro-domains.

### *3.3.2 Single-cell bioelectric dynamics enable hiPSC multicellular pattern prediction under varying cell culture conditions*

We next defined specific culture conditions that are amenable to simulation and designed to predictably alter specific components of the bioelectric system. The previously defined system conditions characterized the baseline 'Control' culture condition in which the mTeSR culture media is unaltered. The media addition of a specific pharmacological gap junction blocker defined 2 simulated culture conditions: one condition for 25% gap activity inhibition and another for 75% activity inhibition. Finally, the media addition of 10- and 20-mM $K^+$ salt formed 2 simulated culture conditions. The comparison between simulated and experimental image domains was facilitated by $DiBAC_4[3]$ experimental confocal microscopic assays [88]. The anionic fluorophore partitions the cell membrane leaflets in accordance with cell membrane depolarization or hyperpolarization, enabling steady-state qualitative observation of both cellular and multicellular $V_{mem}$ patterns. The dye possesses the advantage of minimal interference with cellular processes and no induced cytotoxicity; furthermore, $DiBAC_4[3]$

enables the non-invasive observation of long-term bioelectric pattern behaviors and subcellular resolution micro-domains. of $V_{mem}$ in differing regions of a single cell's membrane. We observed distinct pattern properties under the 5 experimental culture conditions, indicating that the disruption of ion distributions by pharmacological blockers or increased extracellular ion concentrations yield new stable $V_{mem}$ features on a tissue scale (Error! Reference source not found.**B**). $DiBAC_4[3]$ fluorescence intensity images were pre-processed to yield grayscale outputs for further analysis. We describe below our pipeline for experimental/simulation comparison before discussing detailed results of the cell culture conditions.

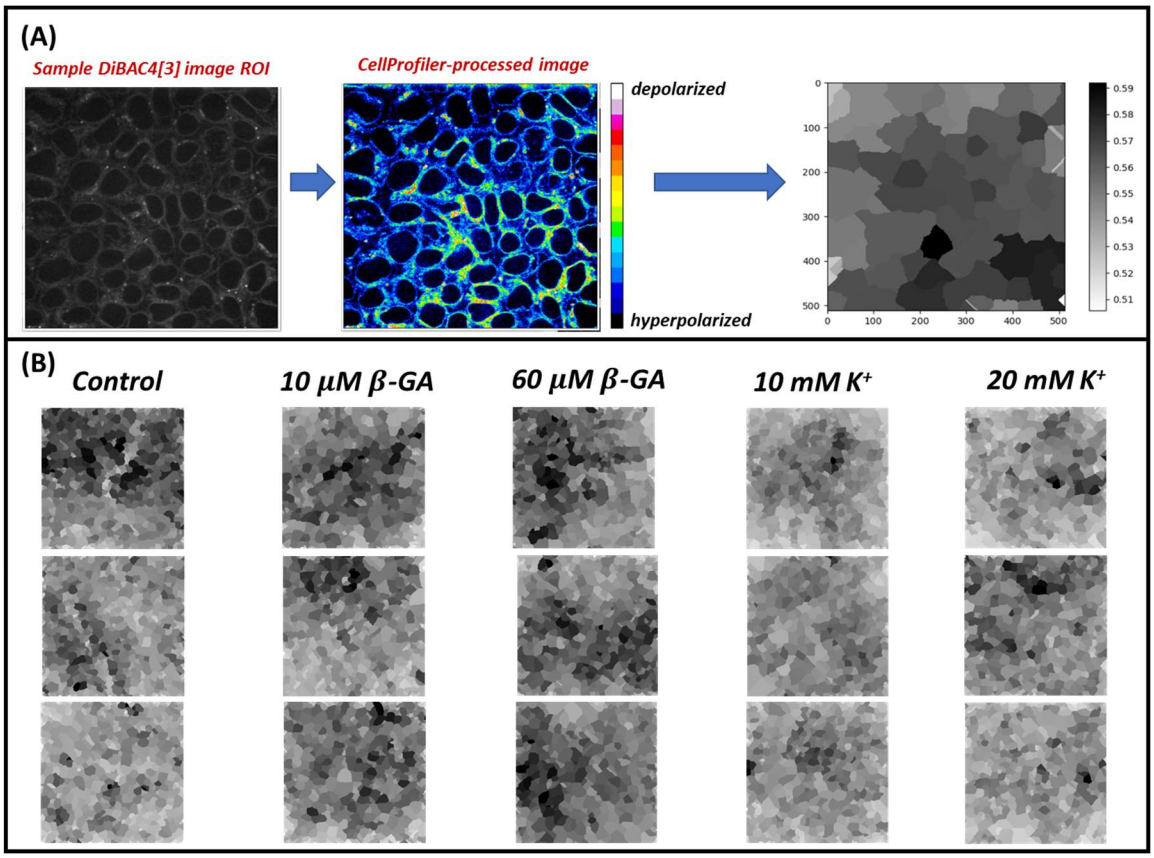


**Figure 3-3. Experimental DiBAC image transformation pipeline outlined for a sample image ROI. (A) The raw output image initially undergoes pre-processing upon export to ImageJ. A pseudo-colored representation of a DiBAC4[3] image elucidates local and global features of $V_{mem}$ heterogeneity in a**

**particular image ROI. The CellProfiler transformed image ROI contains a singular grayscale intensity for each cell, representing the averaged relative $V_{mem}$ for that particular cell. (B) 3 sample output images from each representative *in vitro* culture condition specific $V_{mem}$ patterns highlight the complexity and inconspicuous differences in resultant bioelectric patterns.**

We next generated hundreds of BETSE simulated images for downstream pattern identification and comparison to the microscopy data (**Figure 3-4**). Once the single-, inter-cellular, and environmental hiPSC parameters were set, iterative simulations were run for each described culture condition. Initial simulated pattern outcomes showed heterogeneity in $V_{mem}$ patterning across cell clusters. This observed heterogeneity served as the baseline pattern against which other generated pattern types were compared. Furthermore, the novel bottom-up nature of this bioelectric pattern characterization also necessitated the capability to compare predicted simulated pattern outcomes to those resulting from the experimentally reproduced culture conditions. To this end, we developed a bioelectric pattern characterization pipeline to recognize distinct spatial features of various bioelectric patterns based on a prior algorithm designed for investigating multicellular adhesion [68]. The first input to the pipeline is the processing of simulation pattern images or processed experimental pattern images as described above to be interpreted similarly by a classifier. Tree superposition spatial logic (TSSL) utilizes formal language pattern descriptors, or pattern classifiers, to define local and global pattern features of an image or image set. TSSL is powerful for quantitatively capturing complexity in images at different scales and therefore useful here in identifying pockets of ion flow and regimes of isolated cells within the iPSC colony. The quadtree recursively partitions two-dimensional spatial regions of an image into quadrants of increasing levels of spatial resolution. These partitions specifically contain pixel region-

specific (**Figure 3-4**) intensity information, which would biophysically correspond to a spatial concentration and relative variance of $DiBAC_4[3]$ fluorescence (experimental) or relatively depolarized BETSE-estimated $V_{mem}$ (computational). Generated quad transition systems were translated into condition-specific classifier rules by a supervised machine learning algorithm, RIPPER [89], and these condition-specific rules served as the means for quantitative pattern comparison between simulated culture conditions and their experimental condition analogs.

Each simulated culture condition-specific pattern image set was named in accordance with its proposed system effects and subsequently utilized as inputs to train the rule-based machine learning algorithm (RIPPER). RIPPER compares images comprising the desired target pattern type (+) against the remaining simulated image sets (-) to determine descriptive 'rule sets' for each culture condition-specific output image set. Each rule set is a tuple of translated TSSL formulae, comprised of formal language descriptors of multiresolution patterns features present in (+) images; interpreted as nested if-else statements, they allow spatial features on bioelectric patterning (i.e. iso-potential cell clusters or highly heterogeneous $V_{mem}$ patterns) to be identified and stored for downstream image pattern comparison (**Figure 3-4**). Once a desired pattern type is identified, RIPPER enables quantitative similarity assessment for input images representing differing culture condition patterns outcomes. Specifically, pattern classification rules specific to a target simulated culture condition served as the 'goal' for desired image pattern similarity, and 16 input experiment or simulated images were assessed a similarity score ranging from -1 to +1 based on how similar or dissimilar they

are to the target pattern. In this manner, pattern similarity between simulated and analogous experimental culture condition images can be quantitatively assessed and ranked against other condition-associated pattern outcomes.

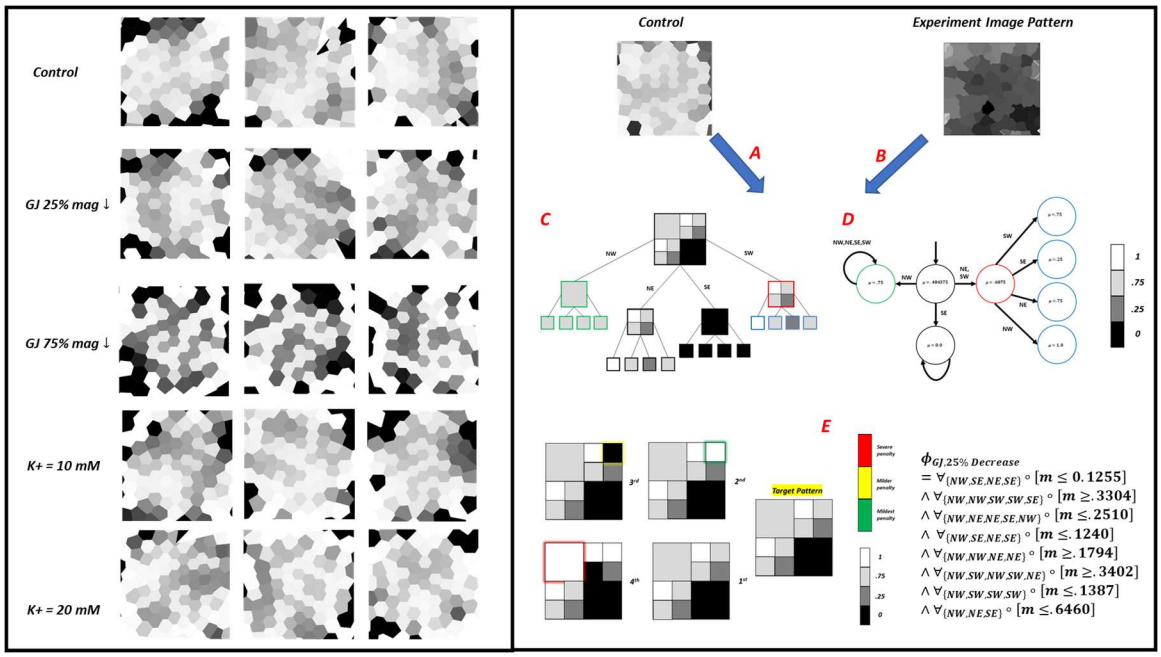


**Figure 3-4. The TSSL Image analysis pipeline for quantitative image similarity comparison. Left: BETSE simulation output images represent each cell as a colored object, where the degree of lightness and darkness represent relatively hyperpolarized and depolarized cells, respectively. Right: The initial generated DiBAC4[3] microscopy image undergoes post-processing in ImageJ to obtain a grayscale representation of relative averaged $V_{mem}$ for each cell (A); fluorescence intensity values are obtained for infinitesimal sections of each cell membrane and summated, then subsequently divided by cell circumference. This process standardizes pattern image outputs to a format similar to that of simulated outcomes from BETSE, shown in (B). The output images are initially transformed into quad-trees (C), data structures in which spatial regions of an image are sequentially subdivided into quadtrees until a particular region only contains a singular pixel intensity; value nodes and edges contain data specific to each image or image set. Each node contains the average grayscale intensity value and variance present in a particular spatial quadrant region and the edges contain information on the quadrant's spatial region coordinates and level of resolution. (D) The quad transition system (QTS) accepts input quad-trees and generates a tuple containing information about color present in a specific spatial region and level of resolution. (E) Similarity scoring is performed in accordance with a metric known as 'distance to satisfaction'; briefly, each input image is compared against the TSSL formula describing a target pattern of interest (F). If the image violates a particular rule at a lower level of image resolution (i.e. whole image), a greater penalty (similarity score reduction) is given than if occurred at a higher level (zoomed in) of resolution. The more different a color for a spatial region is from the target's color in that region, the greater the assessed penalty.**

Previous use in multicellular pattern identification and parameter optimization efforts have validated the ability of this algorithm to distinguish complex image pattern

features within biological multicellular systems [68; 90]. We ran each simulated culture condition (control, 25/75% GJ magnitude inhibition, 10/20 mM K+ addition) (n = 200 per condition) through the pipeline and compared desired pattern conditions against other simulated bioelectric patterns (n = 1000+). We started by creating a target pattern class for the simulated control conditions. Each simulated condition (i.e., control, gap-junction block, etc.) was compared against the other simulated pattern image sets to determine the pattern classifiers which distinguish each condition; the resulting pattern classification outcomes are shown in **Table 3-3** below:

**Table 3-3. Pattern recognition classification accuracy outcomes from supervised machine learning approach**

| Simulated Culture condition | Classification accuracy | Sample size |
|---|---|---|
| **Control** | 97.4% | 200 |
| **GJ 25% mag. ↓** | 94.7% | 200 |
| **GJ 75% mag. ↓** | 94.7% | 200 |
| **$K^+$ 10 mM** | 91.9% | 200 |
| **$K^+$ 20 mM** | 97.0% | 200 |

No pattern classes had a classification accuracy lower than 91%, indicating that the image analysis pipeline could adequately discern differences in patterns amongst simulated conditions. These high classification accuracies were comparable to those observed when applied to reaction-diffusion based [90] and cell mechanics-based [68] multicellular pattern identification, which gave us confidence to utilize the pattern

descriptors downstream. Therefore, these observed pattern classifiers were used for downstream target pattern designation and comparison to experimental patterning outcomes.

### *3.3.3 Unperturbed cell culture conditions preserve heterogeneity amongst hiPSC colonies*

To observe the differences amongst experimentally produced pattern classes we first sought to compare output image classes from the simulated 'Control' condition to those containing alterations (i.e., perturbation conditions). Each produced pattern rule set possessed a distinct difference in its bioelectric pattern 'signature', as validated by the rules that comprise each condition's pattern classifier. Therefore, we used the computationally simulated 'control' bioelectric pattern class image set as the target rule set (positive, +) against which other perturbation-induced pattern conditions (negative, -) images were compared. The machine learning algorithm (RIPPER) was subsequently utilized to generate a 'Control' classifier rule set, based on the provided training and testing 2 set image data. The resulting rule set described distinct local and global spatial features of 'Control' bioelectric pattern images. This rule set was used as the target pattern description for quantitative pattern similarity scoring against experimentally produced bioelectric pattern image sets. The unperturbed 'Control' class produced from the experimental recapitulation of the hiPSC computational model 'Control' simulation conditions provided the highest robustness score when compared to the other experimentally produced pattern classes. This outcome supports our hypothesis that bioelectric patterns can be accurately predicted, given adequate system component characterization. Furthermore, there are statistically significant differences in the

'Control' and 'β-GA 10 uM' population similarity score means (**Figure 3-5**), suggesting that these opposing culture conditions lead to considerable differences in features of their bioelectric patterns.

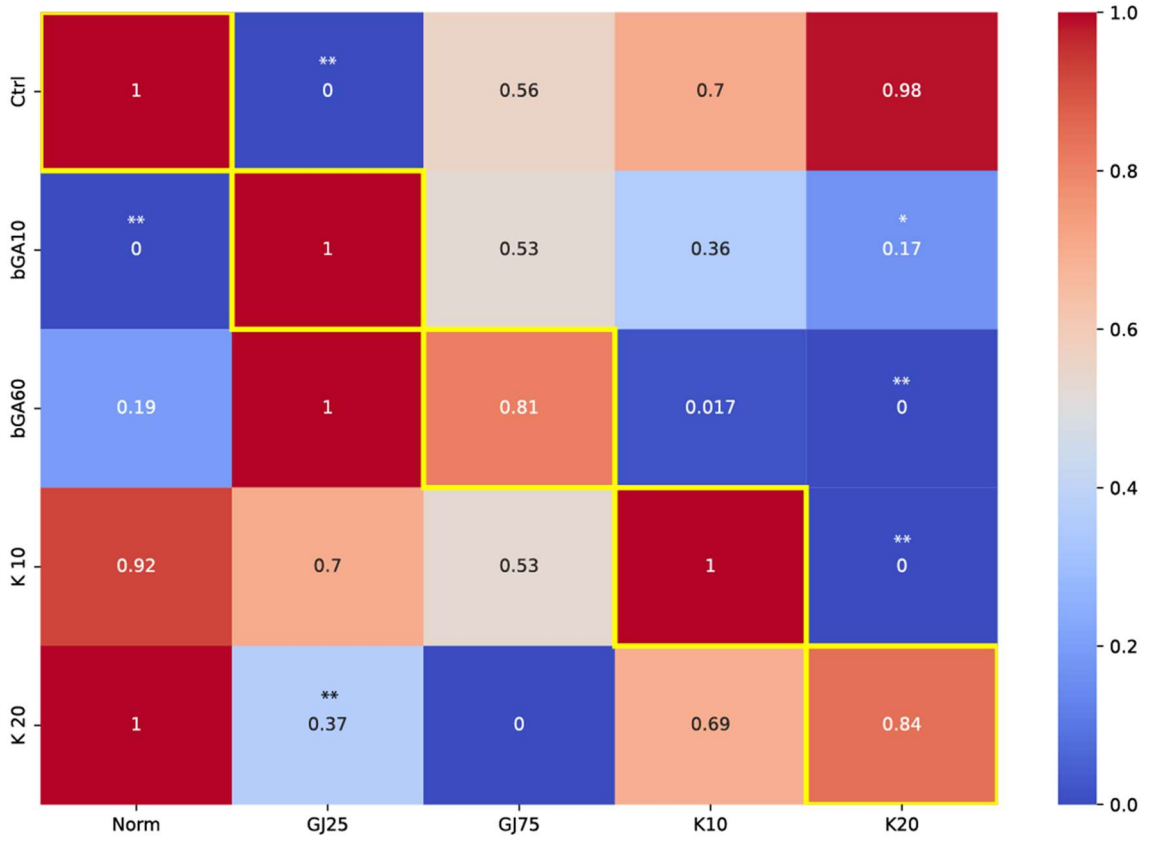


**Figure 3-5. Scaled similarity scoring outcomes are shown; each simulated culture condition (columns) is compared against *in vitro* patterns from the selected culture conditions (rows). Culture conditions analogous between the 2 domains (i.e. BETSE 'control' vs. *in vitro* 'control') are denoted by values on the matrix diagonal, surrounded by a yellow border. Statistically significant differences are indicated by double ($p < 0.05$) and single ($p < 0.1$) asterisks (located above score values).**

Both β-GA classes produced lower pattern similarity scores than the 'K+ supplement' condition pattern similarity scores. This ordering of pattern similarity aligns with our expected pattern similarity outcomes, as K+ supplementation should not necessarily alter large-scale (multicellular) $V_{mem}$ heterogeneity and β-GA, the gap junction uncoupling agent, increases the likelihood of iso-potential cell cluster formation throughout colonies.

### *3.3.4 Relative inhibitory relationships between gap junction activity and emergent bioelectric patterns are elucidated*

We next sought to validate the model-predicted changes in hiPSC bioelectric patterning because of partial simulated gap junction conductance inhibition. A study conducted by [79] reported that connected amphibian blastomere gap junctions possess a specific voltage-gated relationship, where transjunctional conductance reaches its maximum value when cell pairings are 'iso-potential' and decreases as cells increase their transjunctional voltage difference. Furthermore, current transients (endogenous and externally modulated) have been shown to induce long-term changes in cell-cell coupling dynamics. These combined effects direct multicellular steady-state patterning outcomes in multiple developmental [60; 91] and regenerative [48] contexts. This direct relation between gap junction activity and large-scale bioelectric pattern states motivated us to simulate hiPSC clusters with partially inhibited cell-cell gap junction conductance. To this end, we sought an intrinsic or pharmacological compound to experimentally replicate this gap junction mechanism of action. 18β-Glycyrrhetinic Acid (18-β-GA) has been reported [92; 93] to partially inhibit transjunctional ion flux between neighboring 2 cells, and this relationship spans physiological values of transjunctional $V_{mem}$ (-60 to +60 mV); however, patch-clamp characterizations have shown that transjunctional gating voltage sensitivity remains relatively unaffected by the compound [92; 93]. 18-β-GA empirically shifts the cell-cell current-voltage relationship to lower conductance values, consistent with its mechanism of action in which binding of the molecule uncouples gap junction functions through partial or complete disassembly [164]. To obtain a mathematical representation of partial cell-cell communication suppression, we related the literature-associated drug

effects on connexin conductance to the most similar *in silico* parameter governing gap junction conductance. Because gap junction channel partial or complete disassembly effectively decreases gap junction quantity, we modified the simulation parameter controlling intercellular ion flux magnitude ($\beta_{GJ}^{0}$), but did not alter Vmem-sensitive gating parameters. Therefore, we varied $\beta_{GJ}^{0}$ between its completely open (1e-7) and closed (1e-9) values. This has the effect of decreasing the effective connexin pore radius connecting cells, which effectively mimics the phosphorylation effect of $\beta$-GA on gap junction activity. Two distinct gap junction block classes were simulated in BETSE, namely '25% and 75% gap junction conductance decrease', which were distinguished by the respective strengths of gap junction conductance inhibition. TSSL was subsequently utilized to quantitatively assess pattern similarity between the 'BETSE 25% and 75% gap junction conductance decrease' classes and the experimental culture condition-associated classes, specifically the '*in vitro* 10 and 60 $\mu$M $\beta$-GA' pattern classes. The $\beta$-GA 10 $\mu$M culture condition had the highest similarity score in comparison to the other experimental perturbation classes, and the next closest perturbation class similarity score came from the $\beta$-GA 60 uM class (**Figure 3-5**). This quantitative similarity trend supported the multicellular pattern effect in GJ trans-junctional current decrease proposed by [85]; the 'BETSE 25% conductance decrease' class showed statistically significant differences in similarity scores over the 'Control' and 'K+ 20 mM' *in vitro* pattern classes (**Figure 3-5**). The 'BETSE 75% conductance decrease' class did not display statistically significant differences in similarity scores, but the highest similarity score was observed to come from the analog '$\beta$-GA 60 uM class' culture condition, which supports the hypothesized bioelectric patterning that arises as a result of perturbed K+ ionic flux dynamics. The $\beta$-

GA pattern class similarity scores show clear distinction over the K+ 10- and 20-mM supplementation classes, consistent with trends observed earlier concerning the relative pattern similarity between control and K+ supplemented culture pattern outcomes. Overall, the model was able to adequately distinguish local and global spatial features of bioelectric patterning that arise from lower-level changes to intercellular bioelectric system dynamics.

### *3.3.5 Cell culture K+ supplementation can modulate emergent bioelectric patterns in hiPSC clusters*

The cell electrochemical balance and ion flux [94] determines reversal potential, the $V_{mem}$ at which net ion flux across the membrane changes direction. Extracellular $K^+$ ion concentration changes shift this $V_{mem}$-dependent transmembrane ion flux in accordance with induced changes to the electrochemical potential. Previous studies reported potassium ion channel expression and currents to dominate resting and dynamic cell bioelectric behavior in embryonic/pluripotent cell phenotypes [82; 73; 74], and existing literature suggests a critical role for voltage-gated $K^+$ channels in downstream cell fate decisions in mouse embryonic stem cells [95].

More specifically, our hiPSC scRNA-Seq data indicates that the voltage-gated $K^+$ ion channels were more highly expressed than $Na^+$ or $Cl^-$ ion channels, and supports the notion that they are likely the main contributor to voltage-gated ionic fluxes in the pluripotent state. Furthermore, $K_v7.2$ was the most highly expressed voltage-gated ion channel (**Figure A 4**). These observed phenomena drove model recapitulation via the utilization of a custom voltage-gated potassium ion channel, which provided the dual effect of $K^+$ control of single-cell voltage-dependent conductance and a means to relate back to

the experimentally measured cell current-voltage relationship. Given the dominant role of $K^+$ transmembrane flux in $V_{mem}$ regulation, we hypothesized that heterogeneity in $K_v7.2$ expression will directly affect single-cell $V_{mem}$ states, but it is unknown how these cell-level changes affect emergent pattern outcomes. We expected to see a relatively iso-potential bioelectric signature behavior because high external $K^+$ supplementation theoretically affects cell $V_{mem}$ via direct changes to the potassium-specific Nernst (equilibrium) potential, and consequently, $K^+$ $V_{mem}$-dependent transmembrane ion flux, collectively bringing the cells closer to 0 mV. Therefore, we utilized simulation outcomes as a means of understanding the potential bioelectric landscape when the $K^+$ supplementation conditions are experimentally reproduced. TSSL-produced pattern classifiers for the 'BETSE 10- and 20-mM K+ supplementation' classes were compared against *in vitro* image outcomes, as shown in (**Figure 3-5, Figure A 2**). The 'BETSE K+ 10 mM' pattern class had the highest observed quantitative similarity score when compared to its experimental 'K+ 10 mM supplement' analog but did not contain statistically significant differences in similarity score when the analog-produced similarity score was compared to other culture condition-specific pattern classes. However, the second and third highest similarity scores came from the experimental 'Control' and 'K+ 10 mM supplement' classes, respectively. These outcomes supported the hypothesized effect on multicellular bioelectric pattern formation. The 'BETSE K+ 20 mM' pattern class had the highest observed quantitative similarity score when compared to the experimental 'Control' class, instead of the hypothesized experimental 'K+ 20 mM supplement' analog. The second highest similarity was observed to be the 'K+ 20 mM supplement' experimental analog. The general trend of higher similarity of 'K 20 mM', 'K 10 mM', and

'Control' scores in comparison to the '$\beta$-GA 10 and 60 $\mu$M' experiment pattern classes were preserved, and the similarity score for the 'BETSE 20 K+ mM' pattern class compared against the experimental 'K+ 20 mM supplement' class displayed a statistically significant decrease over both '$\beta$-GA 10 and 60 $\mu$M' experiment pattern classes ($p < 0.1$ and 0.05, respectively). Overall, the similarity scores indicated that the model can predict its experimentally analog's bioelectric patterns; however, the 'Control' condition outperforms the K+ experiment classes in both 10- and 20-mM cases, indicating that K+ supplementation may not significantly vary multicellular steady-state bioelectric patterns.

### *3.3.6 Particle Swarm Optimization elucidates possible parameters that lead to desired bioelectric patterns*

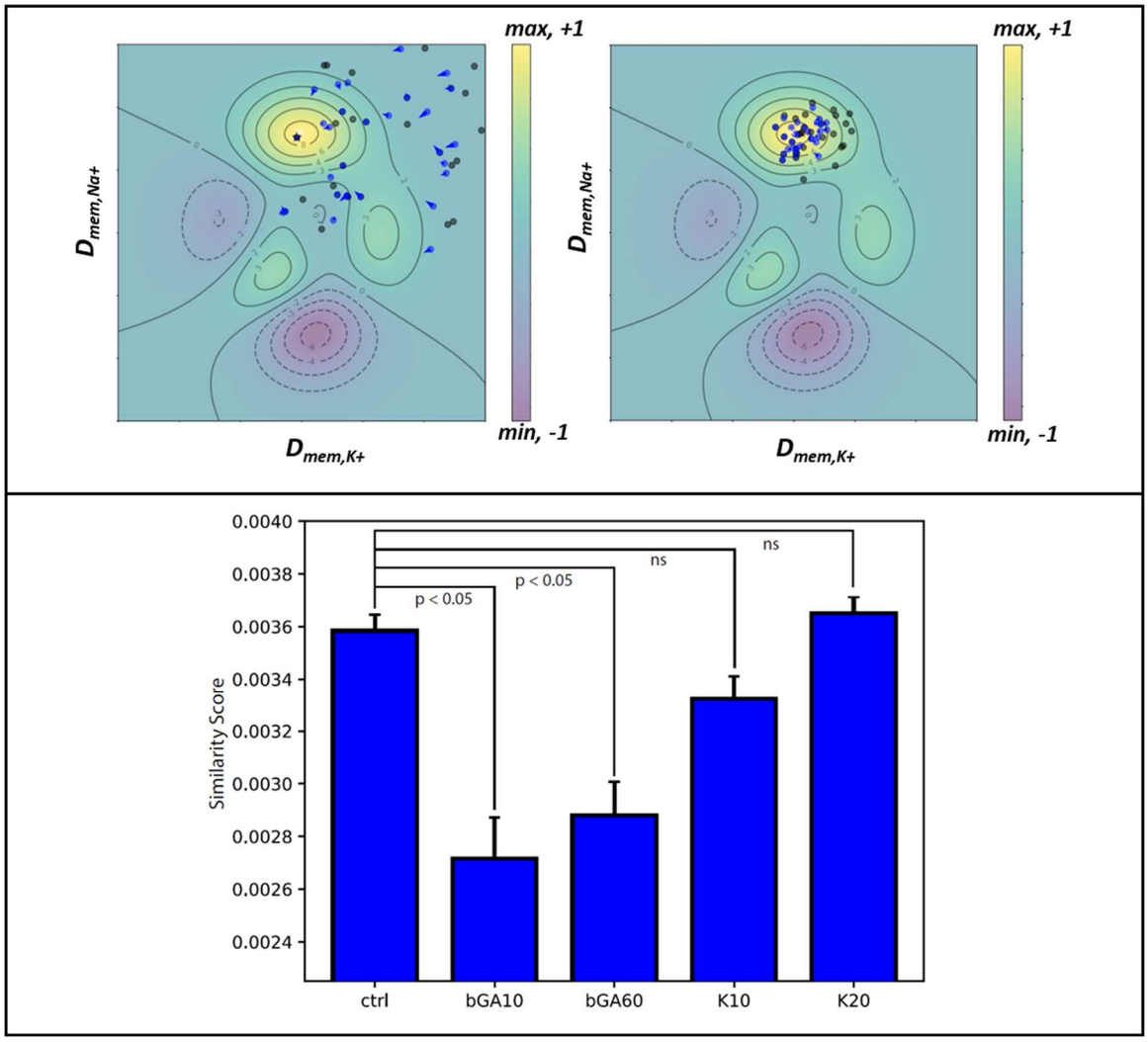


**Figure 3-6. Scheme for parameter optimization. Top: Simulations containing differing parameter combinations are run and subsequently scored for similarity to the desired target pattern; if the similarity score increases as a particle searches a certain direction it will continue to move until the maximum target similarity is obtained, at which point the algorithm stores the parameters and defines them as optimal parameters to produce a desired bioelectric pattern. Bottom: Similarity scoring between optimized-parameter associated control simulation pattern classifiers and experimental condition pattern sets from 'Case 1' is shown.**

The validation of established synthetic control over form would extend the potential use for bioelectric patterning in a variety of practical applications. For example, transmembrane ion diffusivities are bioelectric system parameters that can be pharmacologically tuned *in vitro* with ionophore supplementation. Ionophores are compounds that enhance ion transport across the cell membrane via a pore-forming channel

mechanism; different classes of ionophores selectively transport specific ions, enabling control over individual transmembrane ionic fluxes. Furthermore, integration of microelectrode arrays (MEAs) may also enable precise spatial control over concentration, which facilitates a higher degree of spatial ion flux regulation. These tools specifically allow us to experimentally probe the model predictive capabilities when its representative diffusivity parameters are increased to imitate *in vitro* cell ionic flux modifications. This inspired us to test the hiPSC-specific model's ability to produce combinations of individual transmembrane ionic diffusivities ($D_{mem,i}$). Importantly, the ability to correctly predict bioelectric system parameter combinations in physiologically reasonable search space would enable precise planning of ionophore and culture 2 media ionic composition to controllably manipulate bioelectric patterns through intrinsic/autonomous means. Since the TSSL pipeline assigns quantitative values to images based on similarity to a target image, we implemented Particle Swarm Optimization (PSO) [96] to maximize the similarity score between input image sets and the target pattern classifier (**Figure 3-6**). In essence, the algorithm initializes simulated parameters, or particles, at maximum and minimum extremes of the allowable n-dimensional parameter space, then iteratively searches for local maxima from the similarity score space and compares maximum scores amongst local swarms, and the maximum or minimum-valued scores from each group are assumed to be the optimized parameter(s). These optimized parameters are interpreted as the prerequisite 'parameter combinations' needed to ensure a desired target patterning outcome. The algorithm is described in further detail in the supplemental methods section. We initially set up 3 basic optimization scenarios in which individual ionic transmembrane diffusivities or gap junction conductance strength could vary between 1e-16 and 1e-19 $m^2/s$ for $K^+$ and

1e-17 to 1e-19 for both $Na^+$ and $Cl^-$; the fractional gap junction surface area ($\beta_{GJ}^0$) was varied between 1e-9 and 1e-7. Briefly, the first scenario entailed a $D_{mem,K+}$ or $\beta_{GJ}^0$ parameter optimization in a one-dimensional parameter space. The second scenario encompassed simulations in which $D_{mem,K+}$ and $D_{mem,Na+}$ diffusivities were simultaneously adjusted in 2-dimensional parameter space. The final scenario encompassed a simultaneous $D_{mem,K+}$, $D_{mem,Na+}$, and $D_{mem,Cl-}$ search in 3D parameter space in an effort to elucidate a potential novel combination of ionic diffusivities that could potentially satisfy the requisite bioelectric pattern features to optimally recapitulate the 'Control' target pattern classifier. For each defined optimization scenario, each parameter-specific particle was moved around in parameter 'search-space' in accordance with its own best similarity score as well as the group's best score each iteration until a defined error threshold was met or the produced pattern similarity score in comparison to the target pattern is maximized for the input parameter(s). We started the one-dimensional parameter space exploration by varying K+ diffusivity. The produced optimal $D_{mem,K+}$ parameter value was approximately 8.185e-18 $m^2/s$, a 70% difference from its original value, 2.744e-17 $m^2/s$. We repeated this procedure for $\beta_{GJ}^0$ and compared optimization results for the 'GJ 25% Decrease' and 'GJ 75% Decrease' target pattern classifiers,which both maintained constant $D_{mem,K+}$, $D_{mem,Na+}$, and $D_{mem,Cl-}$ parameter values, but only varied $\beta_{GJ}^0$ value (7.525e-8 and 2.575e-8, respectively). The PSO outcomes returned optimized parameter values of 1e-7 (46.5% difference from the initial value) and 1.377e-8 (46.5% difference from the initial value), respectively. The predicted values were on the same order of magnitude as the initial 'Control' class parameters values, but were significantly different, suggesting that the current model can estimate optimal parameters with some relative degree of precision, but

not high predictive accuracy. Next, we ran a two-parameter PSO in which $D_{mem,K+}$ and $D_{mem,Na+}$ were simultaneously varied throughout the allowable parameter spaces and simulated. Importantly, the characteristic steady-state $D_{mem,K+}$:$D_{mem,Na+}$ ratio deserves more attention than the individual $D_{mem,K+}$ and $D_{mem,Na+}$ values, due to the downstream consequences on cellular $V_{mem}$ state. The Goldman Hodgkin Katz equation asserts that when intra- and extracellular ion concentrations remain constant the ionic diffusivity ratio directly controls $V_{mem}$ state, with this trend being validated experimentally [97; 98; 99]. Therefore, we assumed that the preservation of ionic permeability ratio is the determining factor for steady-state $V_{mem}$ and hypothesized that novel $D_{mem,K+}$:$D_{mem,Na+}$ ratio would relatively recapitulate that of the original 'Control' pattern class. We obtained 2 estimated optimal diffusivity parameter sets, named 'Case 1' and 'Case 2', which produced $D_{mem,K+}$:$D_{mem,Na+}$ ratio values of approximately 10 and 12, respectively (**Figure 3-6**). These parameter ratios maintained relative closeness to that of the initial 'Control' pattern class. The relative adherence of the predicted K+:Na+ diffusivity ratios to that of the original simulated 'Control' class gave us confidence that *in vitro* recapitulation of these values would produce patterns of a similar nature to that of the unaltered mTeSR 'Control' culture condition. This led us to inquire into the quantitative pattern similarity between the novel simulated image set patterns classifiers and its 'Control' *in vitro* culture condition analog. Thus, we sought to extend this novel parameter optimization analysis to *in vitro* pattern similarity comparison. We hypothesized that the optimized $D_{mem,K+}$/$D_{mem,Na+}$ parameter sets predicted to optimally satisfy 'Control' target pattern conditions would reproduce similarity score trends when compared to *in vitro* pattern classes, analogous to the manner that the original BETSE 'Control' pattern class was compared against *in vitro* pattern

classes. To this end, we utilized the optimal ion diffusivity parameters produced from the PSO combined $D_{mem,K+}/D_{mem,Na+}$ 'Cases 1 and 2' as input conditions to iterative BETSE simulations (n = 200), and pattern classifiers were subsequently assigned to both case's image sets. Similarity scores were then measured for experimental control and perturbation class images and compared. Interestingly, both cases of pattern comparison elucidated K+ 20 mM experimental bioelectric patterns to be closer to the target PSO-induced patterns than the hypothesized 'PSO control' classes (**Figure 3-6**). Although this similarity score difference was not statistically significant, the same similarity trends with respect to the K+ supplementation experimental classes to the target control were still maintained, suggesting some order of conserved hierarchy in image bioelectric pattern similarity across recapitulated culture conditions.

Overall, outcomes from these various parameter optimization scenarios demonstrate the potential application to multicellular system bioelectric pattern control, but also highlights the need for further model improvements must first be made before reliable application to hiPSC cellular systems *in vitro*.

### *3.3.7 Disruption of intrinsic gap junction connectivity in iPSC colonies*

Given the ability to estimate patterning outcomes either when one or simultaneous bioelectric system components are being varied in parameter space, we sought to further probe the model's ability to predict multicellular bioelectric patterns when system components are selectively knocked out in certain cell subpopulations. The hiPSC-specific bioelectric model simulations and experimental $\beta$-GA dose-dependent (10 and 60 $\mu$M) results suggested that partial inhibition of gap junction communication between

neighboring hiPSCs would yield novel $V_{mem}$ patterns at the tissue scale (**Figure 3-7**). It has been shown that gap junctions not only possess dynamics pertaining to the 'like' cell population but may also isolate differing cell phenotypes or sub-populations [100; 101] in larger multicellular systems, suggesting pivotal bioelectric pre-patterning roles in development. Because we observed that pharmacological inhibition of GJCs ($\beta$-GA media addition) led to unique spatial bioelectric pattern features, we hypothesized that a heterogeneous mixture of GJC disruption would yield a more complex novel class of bioelectrical patterns. The defining feature of this novel pattern is the manner in which the bioelectric system components are altered. Rather than altering the system component's characteristics throughout the entire cell population, the dynamics would be altered for only a certain cell subpopulation within the collective. The ability to accurately predict pattern outcomes without prior assay-derived component dynamics probing would validate the model's ability to not only predict multicellular pattern outcomes under well-defined system component modifications but, would also inspire confidence to further predict and analyze previously undefined bioelectric pattern conditions *in vitro*. Importantly, the experimentally testable spectrum of culture conditions and potential combined system parameter modifications would exponentially decrease both time and required resources in laboratory settings. Thus, we wanted to test the possibility that these unexplored, simulated bioelectric system conditions could also lead to predictable multicellular bioelectric patterns in hiPSCs with subsequent experimental observation. To this end, we simulated a condition, which we named 'GJ5050CtrlorBlock', in which simulated cells were defined by two different resting $V_{mem}$ states and gap junction activities (**Figure 3-7**); one population contained normal Cx43-based gap junction dynamics, while the other implemented a

complete block of gap junction cell-cell conductance. Following the creation of a simulation image set, we utilized TSSL to define a pattern classifier for the simulated mosaic condition (n = 200). This effect could not be replicated via $\beta$-GA use, as it only provides partial conductance inhibition between adjacent hiPSCs. Therefore, we cultured two hiPSC lines (LBC2 and LBC2-GJA1) to replicate these simulated mosaic conditions *in vitro*. LBC2-GJA1 is the CRISPRi-edited version of the LBC2 hiPSC line in which GJA1 (CX43) is silenced with continuous doxycycline exposure (**Figure A 5,Figure A 6**). We cultured the cells for four passages before experimental characterization and seeded the corresponding cell populations at equal density (750,000-1e6 cells/FluoroDish) for 1 day prior to imaging; the resultant mosaic phenotypic mix was imaged using DiBAC.

We specifically compared this LBC2/LBC2-GJA1 CRISPRi mosaic condition to the other *in vitro* perturbation and control image sets (**Figure 3-7**). Ideally, the knockout of this specific isoform would ablate all intercellular ion flux, but multiple studies have shown the existence of other expressed connexin isoforms, which can form homotypic of heterotypic connexon intercellular ion channels [102]. This indicates the possibility of residual intercellular ion fluxes, but the majority of intercellular fluxes are still inhibited with GJA1 (Cx43) knockdown. This class addition gives us some logical means to compare the quantitative pattern similarity difference between a "complete" gap junction communication inhibition and a complete inhibition of one mixed cell subpopulation of two total. We performed similarity score analysis for the collective *in vitro* classes with respect to the target novel 'GJ5050CtrlorBlock' pattern classifier and found that this specific bioelectric pattern niche possessed the highest similarity score in comparison to the simulated analog 'BETSE 50/50 GJ Mosaic' target pattern classifier.

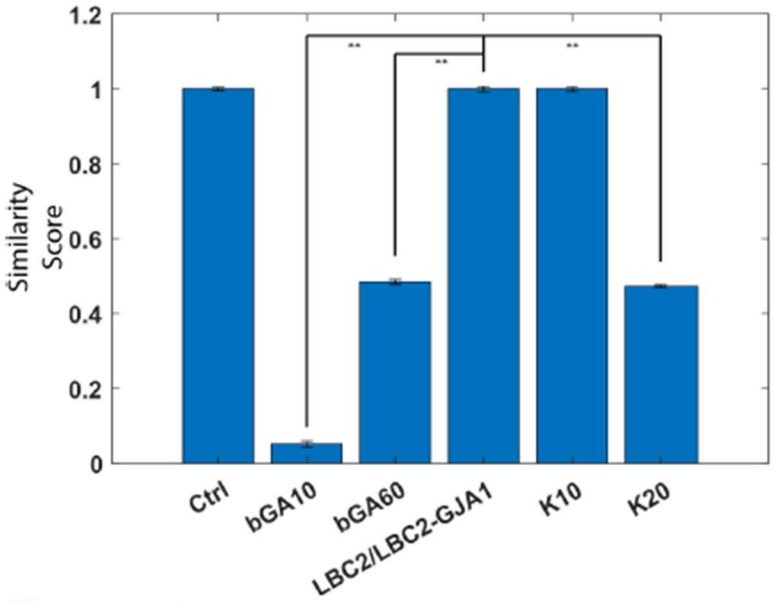
1.2
1
0.8
0.6
0.4
0.2
0
Similarity Score
**
**
**
Ctrl
bGA10
bGA60
LBC2/LBC2-GJA1
K10
K20

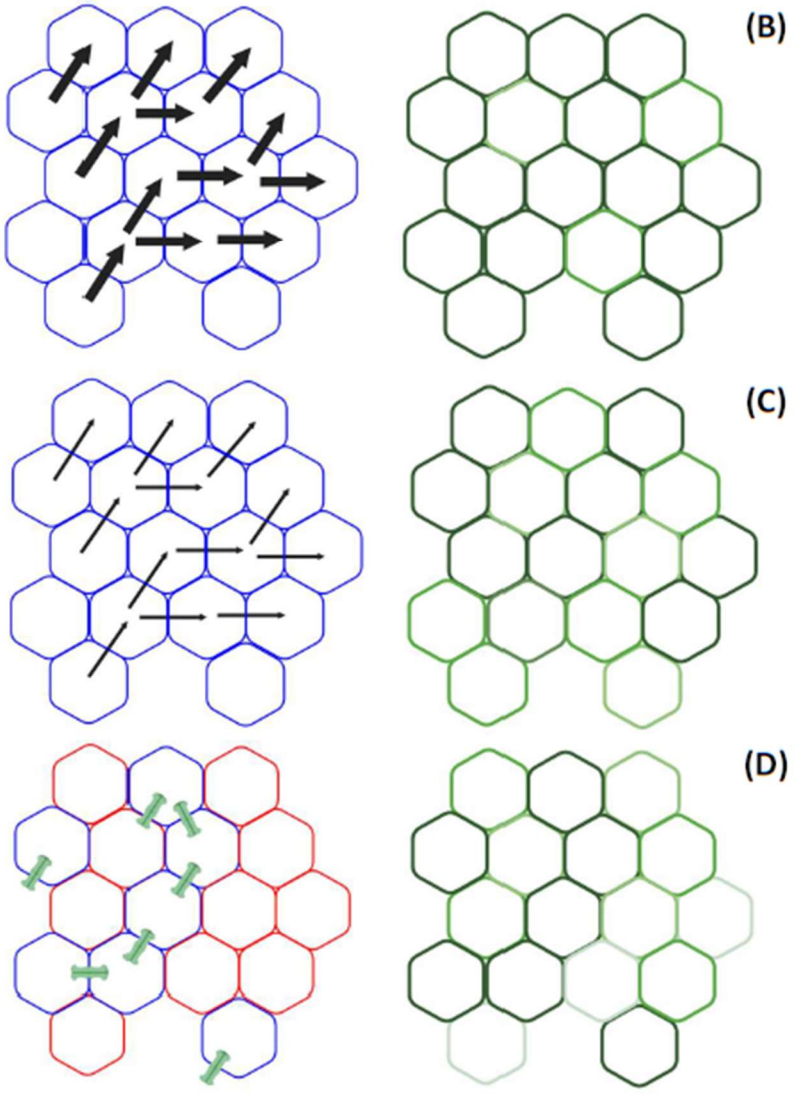
(B)
(C)
(D)

**Figure 3-7. The similarity scores are shown for the pattern comparison between condition specific experiment image sets and the target 'GJ5050CtrlorBlock' classifier (top panel). (B, left) A representative schematic is shown in which 25% of gap junction's currents are inhibited at random (inhibited gap junctions are shown in black); (B, right) A schematic represents the predicted resulting multicellular $V_{mem}$ distribution under 25% gap junction inhibition. (C, left) A representative schematic is shown in which 75% of gap junction's currents are inhibited at random (inhibited gap junctions are shown in black); (C, right) A schematic represents the predicted resulting multicellular Vmem distribution under 75% gap junction inhibition. (D, left) Shown is a typical cell culture schematic, where the spatial arrangement of LBC2 and LBC2-GJA1 hiPSCs is denoted by blue and red cell borders, respectively. The experiment preparation procedure ensured minimization of potential bias originating from identical cell population regions within a culture plate; the two lines were re-suspended in the same solution prior to seeding to ensure cell sub-population spatial 'noise', or heterogeneity. (D, right) a sample representative schematic of $DiBAC_4[3]$ accumulation throughout the interconnected cell clusters shows the consequences of inhibited intercellular communication; the right-hand portion of the cluster, which consisted of predominantly LBC2-GJA1 cells, exhibits a range of fluorescence intensities, whereas the adjacent LBC2 pairs share bioelectric signaling state information and form iso-potential pairs**

This measured pattern similarity outcome supported the hypothesized effect on emergent multicellular bioelectric patterning, even in the case when multiple parameters of the bioelectric system are simultaneously perturbed. Interestingly, there were statistically differences in similarity score between the 'BETSE 50/50 GJ Mosaic' and 'LBC2/LBC2-GJA1' condition and both '$\beta$-GA 10 $\mu$M' and '$\beta$-GA 60 $\mu$M' gap junction inhibition experiment pattern classes, as well as the 'K+ 20 mM supplement' pattern class. The $\beta$-GA media addition inhibits cell-cell ion flux for all collective populations, so the same expected locally distinct $V_{mem}$ heterogeneity amongst neighboring cells should be present in this co-culture. We observed a significant difference in quantitative pattern similarity when a portion of the colony cells have intercellular communication inhibited. This indicates that the pattern consequences resulting from this slight alteration in the bioelectric system conditions are accurately recapitulated even when compared to similar culture conditions. However, the difference between the LBC2/LBC2-GJA1 condition and '10 mM K+' and 'Control' experimental patterns were not statistically significant. Overall, these observed trends provide insight into the specific local and global pattern characteristics that are similar between the gap junction and K+ supplementation

perturbation patterns, as the relatively high similarity scores amongst the 'Control' and 'K+ supplementation' pattern culture conditions lend credence to the basal $V_{mem}$ spatial heterogeneity that is present in this specific culture condition. The almost indistinguishable similarity scores between the 'Control' and 'K+ supplementation' pattern classes reflect the hypothesized media K+ supplementation effects on the multicellular bioelectric system, specifically the global shift in electrochemical potential for the whole cell cluster. We interpret that the cells collectively shift their $V_{mem}$ towards more depolarized states but still maintain the local pattern features associated with variable gap junction intercellular communication in the 'Control' condition.

### 3.4 Discussion

Autonomous control of cell patterning during embryogenesis or morphogenesis integrates multiple intrinsic and extrinsic dynamic factors to achieve repeatable target morphological outcomes, such as the consistent emergent pattern classes that we report in this study. Understanding the underlying molecular components influencing these outcomes could open the door for leveraging the bioelectrical control mechanism of morphogenic trajectories. Previous studies have highlighted the role of ion channels defects in establishing altered anatomical trajectories in multiple species [72]; however, few to date [60] have computationally addressed the consequences of channelopathies across multiple scales (molecular, cellular, and multicellular). Interestingly, studies have shown Kir2.1 to be directly implicated in the onset of craniofacial defects in humans [104] and this effect has been recapitulated in frog and Drosophila embryos [105]. The conserved role in the emergence of downstream anatomical defects across species lends credence to a potential canonically conserved $V_{mem}$-current relationship for the inwardly rectifying

potassium channel. Thus, other human ion channel homologs may be probed for their role in developmental morphological trajectory establishment and maintenance via computational simulations. Therefore, we implemented a novel bioelectric systems characterization of hiPSC bioelectric pattern dynamics to predict emergent outcomes under normal ('Control') and altered cell culture conditions, specifically designed to probe the role of lower-level components in pattern instruction. This characterization design serves the dual purpose of understanding how individual bioelectric components work in an integrated manner to create stable bioelectric pattern outcomes and how specific perturbations to the individual or combined system components lead to predictable steady-state patterning outcomes. We first established an hiPSC-specific computational bioelectric model from the bottom-up via integration of literature electrophysiologic data or 'in-house' experimental electrophysiological data and transcriptomic data. Following the lower-level (subcellular and cellular) parameterization, we ran multiple simulations for various cell culture conditions to assess pattern similarity in each context. We targeted specific types of simulations in which either subcellular (gap junction function) or cellular-level (external media $K^+$ addition) adjustments to bioelectric system components have defined consequences on that component's function, but unknown effects on multicellular system pattern trajectories. Utilizing a previously developed image classification algorithm, TSSL [90] and RIPPER [89], we assigned quantitative values to image similarity and assessed how well computational simulations predicted resulting bioelectric patterns. We found that our 5 simulated culture conditions and resulting bioelectric patterns were quantitatively similar on a global and local scale. The similarity scoring observed is comparable to those observed in [68], and the inherent variability present in experimental images upon changing

the domain from virtual to experimental was also observed in this study. This multi-level integration effort demonstrated the ability to predict novel pattern features under defined certain cell culture conditions. We extended the pattern prediction effort to an unexplored culture niche in which two populations of hiPSCs containing unique cell bioelectric characteristics are cocultured. Simulated patterns replicating the co-culture conditions were quantitatively similar to that of the experimentally replicated 'LBC2/LBC2-GJA1' co-culture condition. Importantly, this validates the model's predictive utility under both well-defined and partially defined initial bioelectric system conditions. Ultimately, this model-guided pattern prediction represents a critical tool that enables the prediction and understanding of emergent bioelectric system dynamics *in vitro*.

The results from the culturing conditions and hiPSC cell co-culture validate the predictive utility of the computational modeling approach when applied to hiPSCs; however, the model's ultimate predictive utility is hindered by several factors. The model presented in this work is considered to be a simplified representation of single-cell bioelectric components and their activities; we assumed $Na^+$ and $Cl^-$ to lack $V_{mem}$-specific ion channel dynamics and assumed a single ion channel $K^+$ characterization; this does not occur realistically, as even a homogenous pluripotent stem cell population possess a distribution of voltage-gated $K^+$ ion channel expression and respective channel activity. Also, $Ca^{2+}$ signaling is a known stem cell fate control mechanism [170]; in mouse embryonic stem cells (mESCs), cell cycle progression is mediated by spikes in cytoplasmic $[Ca^{2+}]$ [170] and the switch between naïve and primed pluripotent states is directly modulated by intracellular calcium levels [170]. Calcium entry into the cytosol from the extracellular space is mediated by voltage-gated ion channels [171], so there is a direct

relationship between calcium signaling, cell fate, and the multicellular hiPSC bioelectric system. Despite the importance of $Ca^{2+}$ signaling in embryogenesis and development, this model does not include this $Ca^{2+}$ ion flux dynamics because our scRNA-sequencing transcriptomic data shows low expression voltage-gated $Ca^{2+}$ ion channel levels in comparison to $K^{+}$ voltage-gated ion channels. While this relationship is assumed to extend to ion channel protein expression this does not necessarily have to reflect reality. These model drawbacks could be potentially alleviated by the integration of proteomic data and more specifically designed patch clamp assay characterizations. However, there are other potential factors that could negatively affect model predictability. Furthermore, we populated the model to possess Cx43 $V_{mem}$-dependent gap junction conductance. In reality, hiPSCs possess a distribution of gap junction expression and isoforms, each isoform possessing slightly different $V_{mem}$ sensitivities. This lack of phenomenological model representation naturally lends model simulations to lose predictive accuracy even if all other relevant intrinsic and extrinsic variables and parameters are properly accounted for. In addition, the model does not account for changes to ion channel and gap junction activity dynamics after the simulation begins. These system components are subject to post-translational modifications and epigenetic modifications, as evidenced by the negative effect of nicotine (a teratogen) on HCN2 function during *X. laevis* neural crest development [60]. This consequently means that even an hiPSC model that fully incorporates transcriptomic and proteomic data could fail to produce solutions that reflect *in vitro* patterning outcomes if the functional consequences of these modifications are not incorporated into model channel function characteristic equations. These potential effects are ignored as one of the core tenets of biological systems modeling is to avoid overfitting

and unnecessarily over-complicating model structure in efforts to preserve predictive flexibility and to guide insights for specific model improvements [107]. Once properly trained and tuned with more experimental datasets and better biotechnological tools, such as ArcLight [106], model bioelectric systems may be probed and assessed for their temporal evolution properties and how they are affected by timed changes to aspects of the bioelectric machinery or culture environment. One promising tool that already offers a high level of temporal precision in its signal control is optogenetic ion channels, which have already shown applicability in mouse embryonic stem cells [108].

The novelty of this prediction pipeline extends past the validated multicellular biophysics; this bridge between the computational and *in vitro* domain space makes model-based bioelectric pattern prediction and control realistically applicable to artificial living machine design from iPSCs [52]. Furthermore, the particle swarm optimization results indicate that cell dynamics may function in different regions of the cell bioelectric parameter space and still create similar and robust patterning outcomes; thus, simulation-guided ionophore or gap junction supplement culture design can be used to test the feasibility of engineering multiple artificially induced bioelectric properties to obtain congruent end patterns. Gap junction role in intercellular communication is canonically conserved and has been shown to disrupt spatial differentiation trajectories and regulate information and cell state processing propagation from single cell to multicellular scale [67; 76]. Model-guided regulation of gap junction dynamics may be utilized in efforts to identify unique, novel multicellular pattern types and potential control over positional outcomes during morphogenesis or tissue regeneration. Ultimately, the novel bottom-up bioelectric system characterization enabled the ability to predict and control bioelectric

patterning in homogenous hiPSC cell clusters *in vitro*, opening the possibility to exert engineered control over bioelectric pattern design and subsequently ensure robust spatiotemporal morphogenic trajectories.

# CHAPTER 4. CHARACTERIZATION OF SYSTEMS METABOLIC PHENOTYPES THROUGHOUT HUMAN IPSC-CARDIOMYOCYTE DIFFERENTIATION

## 4.1 Introduction

Improvements in directed differentiation protocols and advances in purity of the resulting cells are encouraging for potential applications of human induced pluripotent stem cell (hiPSC) therapies for cardiac diseases; however, the immaturity of differentiated cardiac phenotypes hinders confidence in using hiPSC technologies in practical clinical applications. Furthermore, phenotypic heterogeneity could contribute to potential teratoma formation if residual pluripotent cells remain in the targeted therapeutic microenvironment. Therefore, careful consideration should be given to strategies used to improve large-scale production of terminally differentiated hiPSCs; the need for large quantities of pure, matured cardiomyocytes presents a current hurdle for cell manufacturing. Metabolic-based purification represents a preferrable alternative to sorting-based purification strategies, as it is non-invasive and highly effective [112]. Early successful strategies at implementation of metabolic purification relied on mimicking developmental process in their *in vivo* counterparts. It has been shown previously that cell metabolism influences cell fate via epigenetic modification of gene expression [113]. For example, glycolysis-associated acetyl-CoA production has been shown to be critical to maintenance of pluripotency in mouse and human PSCs [44]. Truly unlocking the potential of lineage-specific cell differentiation will rely on holistic understanding of intrinsic and extrinsic metabolic signal drivers of lineage specification upon exit from pluripotency [114; 115]. Protocol

optimization should also carefully consider temporal aspects, as the specific timing of signaling cues have large effects on differentiation outcomes. Therefore, attempts to synthetically modulate cell metabolic landscape should follow the chronological order of metabolic maturation *in vivo*. Multiple groups have performed hiPSC-CM metabolic characterizations and have started implementing these design philosophies in their protocols [116; 117]. Normal heart metabolic distribution shows that approximately 70% of ATP generation is derived from oxidation of fatty acids, and the rest derives from glucose, lactate, and pyruvate metabolism [118]. One study [116] took advantage of this knowledge to design a galactose- and fatty acid-based media formulation that coaxed cells into a metabolic landscape very similar to that of a normal matured heart *in vivo* and observed significant improvements and structural, functional, and electrophysiological maturation of downstream matured hiPSC-CMs. However, there is still a significant lack of information and resources pertaining to transient phenotypic progression that occurs at the start of differentiation. We hypothesized that computational modeling would help elucidate novel, actionable metabolic drivers of specific cell fate decisions to improve cardiomyocyte differentiation. Therefore, we enhanced a previously developed genome-scale computational model of the human metabolic network to better understand the effects of media composition on metabolic landscape for media-based improvements in directed differentiation applications and cellular therapies.

## 4.2 Methods

### *4.2.1 Computational Methods*

#### 4.2.1.1 Flux Balance Analysis

The system of equations representing the human metabolic network reactions is stored in a stoichiometric matrix (*S*) of size *a x b*, where *a* and *b* represent the number of network metabolites and reactions, respectively. Each matrix element $S_{ab}$ represents a reaction stoichiometric coefficient; entries containing negative values (< 0) represent the reactants, values of 0 represent the absence from the reaction, and positive values (> 0) represent reaction products. The expression relating metabolite availability, stoichiometric constraints, and reaction fluxes is shown below:

$$Sv = \frac{dm}{dt} \tag{4.1}$$

where v is a *n x 1* vector representing reaction flux magnitude, and m is a *m x 1* vector in which each element represents metabolite concentration. The system of mass balanced equations is subjected to steady-state conditions, implying concentration does not change with respect to time ($\frac{dm}{dt} = 0$); thus, the equation is revised to:

$$Sv = 0 \tag{4.2}$$

each reaction flux $v_j$ is subjected to upper ($v_{min,j}$) and lower bound ($v_{max,j}$) constraints:

$$v_{min,j} \leq v_j \leq v_{max,j}$$

The solutions satisfying equations 1, 2, and the minimization or maximization of a desired objective function are selected. These mathematical requirements enable the representation of this linear system as a Linear Programming (LP) problem, shown below:

$$\max f(v)$$
$$\text{subject to } Sv = 0 \tag{4.3}$$
$$\text{and } v_{min,j} \leq v_j \leq v_{max,j}$$

The output solution to the LP problem provides the minimal ($f_{min}$) or maximum ($f_{max}$) value of the objective function. These problems are solved computational optimization software Gurobi.

4.2.1.2 Flux Variance Analysis

Flux Variance Analysis (FVA) generates optimal fluxes as ranges that satisfy the maximization or minimization of a specific reaction ($v_j$) objective value, as shown in :

$$\min/\max v_j \text{ s.t. } f(v) = f_{max} \tag{4.4}$$

This representation describes various allowable flux values that a reaction ($v_j$) may obtain. The solution format is more representative of possible network flux distributions than a singular flux vector, which would be provided by parsimonious FBA (pFBA) simulations. Average FVA reaction flux values are estimated by calculating the mean of the minimum and maximum flux values from Eq. 4. 4. The model is required to solve two LP problems for each metabolic reaction; consequently, computational processing time is significantly increased in this type of simulation analysis.

4.2.1.3 Genome-scale metabolic reconstruction

A Genome-scale metabolic reconstruction is a comprehensive representation of all known metabolites, metabolic reactions, related enzymes, and their gene precursors [119; 120]. These reconstructions are consistently updated in accordance with new biochemical information and candidate metabolic reaction features, which are subsequently transformed into a format suitable for computational metabolic modeling [121]. The latest genome-scale reconstruction, Recon 3D, integrates data from 13,547 metabolic reactions, 8,401 metabolites, and 3,268 genes [122]. The representative reactions and metabolites are presented mathematically as entries in the stoichiometric matrix. Genes associated with metabolic enzymes are encoded with gene-protein-reaction rules (GPR), where gene names are represented in NCBI gene symbol or gene ID number format. Model GPRs are expressed as Boolean functions. More specifically, enzymes encoded by the expression of either one of two separate genes are represented with an OR Boolean expression (i.e. Gene 1 OR Gene 2 must be present to catalyze the reaction). Likewise, enzymes encoded by the requisite dual expression of two associated genes are represented with an AND Boolean expression (i.e. Gene 1 AND Gene 2 must be present to catalyze the reaction). Model integration of these expressions is accomplished by incorporating both gene expression values for "OR" statements, and incorporation of the minimum expression value between both encoding genes. Each metabolic reaction has an associated enzyme commission number (EC), which provides data concerning catalytic activity for the enzyme(s) of interest [123].

#### 4.2.1.4 Proteomic and Kinetic Value Model Constraints

For any network reaction with an associated enzyme commission (EC) [119] number and gene-reaction rule, an upper bound constraint was added:

$$v_{max,b} = k_{cat,b}[E]_b \tag{4.5}$$

where $k_{cat,b}$ is the catalytic rate constant representing the enzyme turnover number (1/hr), and $[E]_b$ represents estimated enzyme abundance available to catalyze reaction $b$. For reactions missing either an EC number or a gene-reaction rule, reaction upper bound was artificially set to a relatively high flux ($v_{max,b} = 1e7\ mmol/gDW - hr$) to recapitulate unconstrained reaction flux.

#### 4.2.1.5 Proteomic Enzyme Abundance Estimation and Transcriptomic Model Value Constraint

Estimation of proteomic abundance values was performed by processing WTC11 scRNA-Seq transcriptomic expression data through the protein prediction pathway utilized in [125], where the steps are explained in detail. Ultimately, the FBA model utilizes gene expression (transcripts per kilobase-million (TPM)-normalized) input user data and converts it to estimated protein abundance values (parts per million (PPM)-normalized) for the previously mentioned covered genes in Recon 3D. Proteomics data is converted from ppm to mmol/gDW via the following expression:

$$p_{mmol/gDW} = \frac{1000 f_{DW}}{N_a n_{aa} m_{aa} g_{Da}} \frac{p_{ppm}}{1000000} \tag{4.6}$$

where $N_a$ represents Avogadro's number, $n_{aa}$ represents average amino acid per protein amount, $m_{aa}$ represents average amino acid molecular mass; and $f_{DW}$ is the fraction of cell

dry weight that is protein content. Specific parameter values used in these studies are $n_{aa} = 300$, $m_{aa} = 100$, and $f_{DW} = 0.5$. Both transformed transcriptomic based- and experimental proteomic data subsequently is used to estimate $[E]_j$ with each reaction's gene-reaction rule (GRR). This GRR is a basic and/or conditional operation, where gene expression is the pre-requisite condition for the associated reaction to generate flux. If both experimental proteomics data and estimated enzyme abundance exist for a particular reaction, the conditional operator chooses the minimum value to be used as the model reaction constraint.

#### 4.2.1.6 Thermodynamic Constraints

The model representation of thermodynamic free energy reaction influence was implemented as the free energy-dependent reaction directionality: this was accomplished via the separation of model reaction equations into forward and reverse reaction groups. The thermodynamic status of a particular reaction ($j$) is implemented through a control Boolean variable $b_j$. A value of 1 represents a feasible reaction and 0 represents a non-feasible reaction. This value is determined by equation 4.7, where $\Delta G_j$ represents the change in reaction $j$ Gibbs free energy, and K is an arbitrarily large constant value set to the largest possible model Gibbs free energy ($\Delta G_j$) absolute value ($|\Delta G_j|$). The equations used to determine $\Delta G_j$ for model reactions (**excluding transport reactions**) are calculated as shown below:

$$\Delta G_j = \Delta G_j^o + RT \sum_{i=1}^{m} S_{ij} \ln x_i \tag{4.7}$$

where $\Delta G_j^o$ represents the standard change in reaction Gibbs free energy, R is the ideal gas constant, $S_{ij}$ is the stoichiometric coefficient for metabolite $i$ within reaction $j$, $x_i$ is the metabolite concentration, and T is the temperature. Calculation of model **intercompartmental transport reaction** Gibbs free energy was performed using the expression shown below in equation 4.8:

$$\Delta G_j = \Delta G_j^o + RT \sum_{i=1}^{m} S_{ij} \ln x_i + \sum_{i=1}^{m} c_i S_{trans,ij} FV \tag{4.8}$$

where $c_i$ represents the metabolite electrical charge, $S_{trans,ij}$ represents the stoichiometric coefficient of metabolite $i$ in transport reaction $j$, F represents Faraday's constant, and $V_{mem}$ is the voltage membrane potential difference between the two compartments involved in metabolite transport. $V_{mem}$ is estimated via calculation of the Goldman-Hodgkin-Katz equation, as shown below in equation 4.9:

$$V_{mem} = \frac{RT}{F} ln\left(\frac{P_{Na^+}[Na^+]_{out} + P_{K^+}[K^+]_{out} + P_{Cl^-}[Cl^-]_{in}}{P_{Na^+}[Na^+]_{in} + P_{K^+}[K^+]_{in} + P_{Cl^-}[Cl^-]_{out}}\right) \tag{4.9}$$

Where $P_{Na^+}$, $P_{K^+}$, and $P_{Cl^-}$ represents relative ionic permeability across the membrane. The values used in this study were 1, 5, and 80 for $Na^+$, $K^+$, and $Cl^-$, respectively [169]. Estimated $\Delta G_j^o$ values for many Recon3D reactions could be found in the Virtual

Metabolic Human database [120]. If any reaction had no available $\Delta G_j^o$ data, value $\Delta G_j^o = -999999$ was assigned to the reaction so that flux could still feasibly occur. For each reaction containing metabolite cytosolic concentration range values, the data from [172] was used to set upper and lower confidence bounds to determine $\Delta G_j$ in equation 4.8. If the reaction contained no associated cytosol concentration range data, a value was randomly chosen between $10^{-7}$ and $10^{-2}$ M to determine $\Delta G_j$ in equation 4.8. Media conditions reflected by Appendix tables (see **Table B 1**,**Table B 2**, **Table B 3**) are explicitly defined transport reactions for influx/efflux between the extracellular compartment and the cytosol, where the media concentration of the metabolite defines the $x_i$ in equation 4.7.

#### 4.2.1.7 Kinetic Data Conversion

Enzyme turnover rate data was extracted from the BRENDA database API [123]. First, all reactions associated with available enzyme EC numbers were extracted, with progression from most to least accurate values. If multiple $k_{cat}$ values were available for an enzyme-substrate pair, the average value was used. Only BRENDA $k_{cat}$s measured in the 7-8 pH range were kept to maintain solution flux physiological accuracy and relevance.

#### 4.2.1.8 SeaHorse Data Conversion and Model Constraint Implementation

The integration of SeaHorse assay oxygen consumption rate (OCR), extracellular acidification rate (ECAR), and chemical perturbation-associated electron transport chain (ETC) reaction flux data required the mapping of measured fluxes to corresponding

representative model reactions. Oxygen consumption rate was converted to relevant model units and set as the upper bound constraint for oxygen 'cytosol → mitochondria' and 'extracell → cytosol' inter-compartmental transport fluxes to the converted value. ECAR was then converted to a similar estimated metric, proton production rate (PPR); this inferred metric is a more direct measure of cellular lactate secretion rate. Each specific media formulation has its own unique buffering capacity, which directly affects media ΔpH measurements, the fundamental metric for ECAR measurements. Formulas including the effect of the media buffering power enable interconversion between ECAR and PPR. Calculated PPR was used as a model upper bound, due to its directly proportional relationship with cell $H^+$ secretion rate. Furthermore, the incorporation of ETC chemical perturbation agents enables isolation of PPR with respect to glycolytic activity. Two metabolic processes are responsible for proton secretion: lactate and $CO_2$ production; this notion was experimentally validated in myoblast cells by [128]. Therefore, calculation of glycolytic PPR must account for mitochondrial $CO_2$ and $H^+$ production; this is accomplished by isolating mitochondrial oxygen consumption (OCR) via subtraction of rotenone and antimycin A-treated OCR measurements from control OCR measurements ($OCR_{tot} - OCR_{Rot+AntA}$). The final expression to calculate glycolytic PPR is shown below:

$$\mathrm{PPR_{glyc}} = \left(\frac{ECAR_{tot}}{BP}\right) - \left(\frac{10^{pH-pK_1}}{(1+10^{pH-p\ _1})}\right) * \left(\frac{\max H^+}{O_2}\right) * (OCR_{tot} - OCR_{Rot+AntA}) \tag{4.10}$$

where $PPR_{glyc}$ represents glycolytic PPR, BP (mpH/pmol $H^+$ in 7 $\mu$l) represents media buffering power (or capacity), $ECAR_{tot}$ (mpH/min) represents whole-cell extracellular acidification rate, $K_1$ is the combined equilibrium constant for $CO_2 \rightarrow HCO_3^-$ dissociation, $\max H^+/O_2$ represents the ideal -associated proton secretion for a specific metabolic transformation (i.e. complete oxidation of glucose), represents the fraction of $CO_2$ produced that gives rise to $H^+$ secretion at experimental temperature and pH, and $OCR_{tot}$ and $OCR_{Rot+AntA}$ represent oxygen consumption rates under control and rotenone/antimycin A-treated conditions, respectively (pmol $O_2$/min). Specific values used in our calculations were BP = 0.041, pH = 7.4, $pK_1$ = 6.093, $\max H^+/O_2$ = 1 [168]. OCR measurements usually possessed units of pmol/min/1*$10^5$ cells or pmol/min/$\mu$g-protein dw. The 1 cell ~ 4e-10 gDW approximation from [129] were used to interconvert between unit formats when setting associated model constraints for hiPS cells. An example conversion is shown below:

$$\mathrm{OCR}_{measured} = 230\ \frac{pmol\ O_2}{min\ -\ 1*10^5\ cells} * (\frac{mmol}{10^9\ pmol}) * (\frac{60\ min}{hr}) * (\frac{1\ cell}{4*10^{-10}\ gDW}) \cong 0.69\ mmol/(gDW - hr) \quad (4.11)$$

ETC-based chemical perturbation-associated model constraints are shown in **Table 4-1**

, shown below:

**Table 4-1. Measured Flux/Equation/FBA Reaction table**

| Measured Flux | Equation | Associated FBA Reaction |
|---|---|---|
| Basal respiration | $OCR_{base}$ | $O_{2[extracell]} \rightleftharpoons O_{2[cyto]}$; $O_{2[extracell]} \rightleftharpoons O_{2[null]}$ |
| Mitochondrial respiration | $OCR_{base} - OCR_{rot/AntA}$ | $O_{2[cyto]} \rightleftharpoons O_{2[mito]}$ |
| ATP Production (oxidative) | $4.6 * (OCR_{base} - OCR_{olig})$ | $ADP_{[mito]} + 4H_{[cyto]} + P_{[mito]} \rightarrow ATP_{[mito]} + H_20_{[mito]} + 3H_{[mito]}$ |
| Proton Leak | $4.6 * (OCR_{olig} - OCR_{rot/AntA})$ | $ATP_{[mito]} \rightarrow ADP_{[mito]} + P_{[mito]}$ |
| Max Respiratory Capacity | $OCR_{FCCP} - OCR_{rot/AntA}$ | $O_{2[cyto]} \rightleftharpoons O_{2[mito]}$ |
| Extracellular acidification | $PPR_{base}$ | $H_{[cyto]} \rightleftharpoons H_{[extracell]}$; $H_{[extracell]} \rightleftharpoons H_{[null]}$ |

The activity of ATP synthase is driven by the thermodynamic electrochemical potential gradient across the inner mitochondrial membrane; this gradient is produced a result of electron transfer from reducing equivalents NADH and $FADH_2$ and consequent hydrogen transport into the mitochondrial intermembrane space. This relationship was exploited to estimate numerical oxygen consumption linked with mitochondrial ATP production. A model upper bound constraint value was obtained by subtracting the control OCR measurement value from the OCR value associated with oligomycin treatment. This relationship was chosen because oligomycin acts as a specific inhibitor of mitochondrial ATP synthase activity. Importantly, a hyperpolarization correction factor was applied to the corrected OCR measurements, due to the imperfect substrate conversion efficiency and incomplete utilization of derived phosphates [130; 168]. A combination of rotenone, a complex I inhibitor, and antimycin A, a complex III inhibitor, effectively blocks electron flow through the ETC, consequently preventing complex IV-based mitochondrial oxygen consumption. Therefore, control, or basal, OCR measurement values, were subtracted from OCR measurement values following rotenone

+ antimycin A treatment; this calculation enabled numerical estimation of metabolic flux associated with oxidative metabolic process.

### *4.2.2 Experimental Methods*

#### 4.2.2.1 hiPSC cell culture and directed hiPSC-cardiomyocyte differentiation

WTC11 hiPSCs were maintained, as previously described in Section 3.2.2.1. The cells were subsequently differentiated to hiPSC-derived cardiomyocytes using the protocol described here [36]: prior to the start of differentiation, cells were maintained for 2-3 days in 12-well or 24-well culture plates until they reach ~80-90% confluency. On the day of differentiation, mTeSR culture media was removed from the wells and replaced with RPMI-1640 (+) B27(-) insulin and 7-12 $\mu$M CHIR99021. The cells were then maintained at 37 °C for exactly 48 hours, after which point the RPMI-1640 media was replaced with RPMI-1640 (+) B27(-) insulin and 7-12 $\mu$M IWP2/4 culture media solution. The cells were then maintained at 37 °C for another 48 hours, before culture media was replaced with RPMI-1640 (+) B27/insulin. Cell culture media was then replaced every 48 hours for the next 6 days (days 8-14). After this, cell culture media was replaced with fresh RPMI-1640 (+) B27/insulin every 3 days. In the differentiation protocol involving the 'DreCustom' media formulation the cells underwent the same differentiation protocol described above, but the RPMI1640 (+)B27(-) insulin media formulation was supplemented with 4 mM L-glutamine and 50 $\mu$g/mL L-ascorbic acid from day 0 through the conclusion of the directed differentiation.

#### 4.2.2.2 Single-cell RNA sequencing (scRNA-seq) of hiPSCs and differentiated progeny

Samples maintained on both control and 'DreCustom' culture media conditions until days 0, 4, and 10 of the directed hiPSC-CM differentiation protocol [36], and were subsequently cryogenically preserved until single cell RNA sequencing preparation. On the day of the experiment cells were thawed and initially combined with molecular labels. The process is described here: first, cells were individually profiled by addition of poly(dT) primers in a solution mix. The cell suspension was composed of cells, partitioning oil, and primers, enabled generation of barcode-tagged cell droplets. These droplets were then loaded on 10x Genomics Single Cell 3′ Chips to generate single-cell gel beads in emulsion (GEMs). Immediately following GEM production, the gel bead coat was dissolved, allowing release of lysed cell contents and identifying molecular barcode label. These products underwent subsequent cDNA amplification via reverse transcription and purification. These amplified products were used with each sample's unique barcode label to construct sample-specific complementary DNA (cDNA) libraries in the Chromium instrument. The resulting barcoded libraries were then multiplexed and subjected to a standard NGS short-read sequencing protocol; the output data from these sequencing runs were cell-specific transcriptomic expression profiles.

#### 4.2.2.3 Processing raw scRNA-Seq data

Processing of sample scRNA-Seq data was conducted using Cell Ranger software by the 10x Genomics company (https://www.10xgenomics.com/). Raw base call (BCL) files generated from the Illumina sequencer were first demultiplexed into sample specific FASTQ files by utilizing the *cellranger mfastq* pipeline. Then, FASTQ files were processed through the *cellranger count* pipeline for each cell culture sample. More specifically, *cellranger count* used the STAR RNA-Seq aligner tool [131] to align cDNA

measured reads to the human reference genome, hg19. Then, aligned reads were checked for valid cell barcodes and unique molecular identifiers (UMIs) and filtered. Finally calculated UMI reads were normalized in Seurat [132] and exported as sample-specific matrices containing expression values as counts per million (CPM), or transcripts per million (TPM).

#### 4.2.2.4 MitoTracker Red experiment procedure and analysis

Mitotracker Red CMXRos was utilized to assess mitochondrial $V_{mem}$ during initial stages of hiPSC-CM differentiation (See **Appendix B**). First, a stock solution (10 mM) was prepared in DMSO, per the manufacturer's instructions. The WTC hiPSCs were grown to desired confluence and the directed hiPSC-cardiomyocyte differentiation protocol was performed for days -2 to 1.5. The differentiation media/MitoTracker working solution (15 uM) was applied to the cells , then they were maintained in dark incubation at 37 °C 12 hours prior to measurement. On the experiment day cells were peridiocally imaged in a BioTek Cytation 7 Imaging Plate reader for 12 hours. After the experiment, results were exported as Microsoft excel spreadsheets, where relative fluorescence intensities were analyzed for the various culture media conditions.

#### 4.2.2.5 SeaHorse XFp Experiment procedure and analysis

WTC11 hiPSCs were initially seeded at 275,000 cells per well (~72400 cells/$cm^2$) of a 12-well culture plate, where they were subjected to the [36] hiPSC-CM directed differentiation protocol for 8 days (days -2 to day 6), where they were subsequently passaged and seeded onto GFR-Matrigel coated SeaHorse XFp cell culture microplate wells (Seahorse Bioscience). Cells were maintained in RPMI-1640 (+) B27/insulin at 37

°C for 4 days before experimental analysis (equivalent to day 10 of differentiation). hiPSC-derived cardiac progenitor cells were analyzed in RPMI-1640 (+) B27/insulin culture media or RPMI-1640 (+) B27/insulin culture media supplemented with 4 mM GlutaMAX and 50 $\mu$g/mL L-ascorbic acid (named 'DreCustom'). Cell OCR and ECAR was measured with a XFp Extracellular Flux Analyzer (Seahorse Bioscience). OCR and ECAR were normalized using cell count numbers via Hoechst staining.

## 4.3 Results

### *4.3.1 Constructing genome-scale hiPSC-specific metabolic models*

The hiPSC-specific metabolic model was initialized in the Recon 3D framework [122]; the mathematical foundation of this model is stoichiometric matrix representation of the 13,547 reactions and 8,401 metabolites, which are currently accounted for in a community curated database. Initially, both hESC- (H1 and H9) and hiPSC-specific (C15 and C20) transcriptomic profiles [133] were used to parameterize FVA simulations in mTeSR media conditions. The input transcriptomic data was then converted to estimated enzymatic abundance values [124; 125] and subsequently combined with user-based reaction upper- and lower-bound flux constraints for all associated genes and enzyme commission (EC) numbers. Specifically, these constraints took the form of Michaelis-Menten reaction kinetics representation, where reaction enzyme catalytic rate constant ($k_{cat}$, unit $hr^{-1}$) is multiplied by estimated cell enzyme protein abundance ([E], unit mmol $gDW^{-1}$) to determine minimum and maximum allowable reaction fluxes ($V_{max}$, unit mmol $gDW^{-1}$ $h^{-1}$). The model also incorporated a previously developed custom enzymatic kinetic rate estimation pipeline, based on data pooled from the BRENDA database [123].

Furthermore, thermodynamic model reaction constraints were determined by calculation of transformed changes in Gibbs free energy ($\Delta G'$), which ultimately determines which reactions can carry non-zero "forward" fluxes via reactions containing negative calculated $\Delta G'$ values [134]. Finally, experimental or literature-based oxygen consumption rates and extracellular acidification rates were used to set novel context-dependent model flux constraints for relevant oxidative metabolic reactions. Collectively, these transcriptomic, proteomic, thermodynamic, and fluxomic constraints enable realistic and precise simulation of metabolic flux distribution in various media and environmental conditions.

### *4.3.2 Zhang et al Case Study*

We first applied our novel FBA pipeline that includes extracellular transport explicitly to the investigation of media composition on iPSC-derived cardiomyocyte differentiation using previously published datasets from the literature [129].

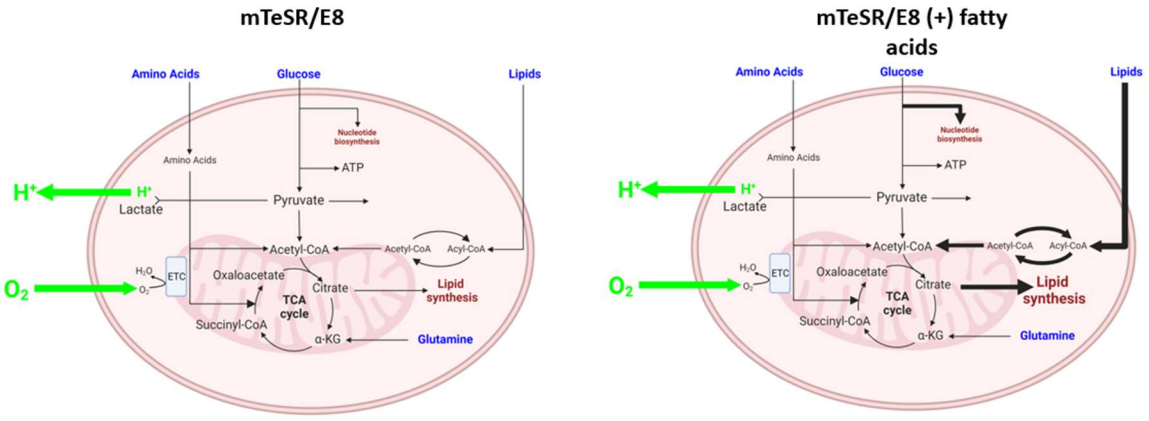


**Figure 4-1. Overall schematic shows changes to metabolic profile resulting specific media formulations; (left) cells cultured in a chemically defined culture media (mTeSR/E8); (right) relative changes to metabolic profile resulting from fatty acid supplementation.**

In the first study, published WTC11 hiPSC transcriptomic profiles were used to assess the effects in internal metabolic flux profiles under lipid supplementation. The authors'

observations that hPSC metabolism was 1) sensitive to media lipid composition as reflected in internal metabolite interconversion under mTeSR, E8 and MEF-CM media and 2) palmitic acid supplementation enhanced lipid biosynthetic products initiated further inquiry into the contribution of specific metabolic pathways to cell maintenance and function under specific media conditions (**Figure 4-1**). In our first model comparison performed, we simulated E8 vs E8 supplemented with albumin-bound [U-$^{13}C_{16}$]palmitate (U-Palm E8). Similar trends in metabolic pathway utilization were observed for both mTeSR and E8 media conditions, motivating our computational re-creation of the metabolic network profile prediction under the described media formulations. We initially defined reaction flux upper/lower bounds using our novel pipeline of combined omics, fluxome and media-based constraints data. We then generated an input media file containing the native mTeSR components and an additional 100 $\mu$M palmitic acid. Then FVA simulations were performed for the novel media and the mTeSR control conditions.

Most notably, the flux through the Glucose 6-Phosphate Dehydrogenase (G6PDH) enzyme increased under the simulated control media conditions, as indicated by the 5.31-fold flux increase under control (mTeSR) media conditions in comparison to the treatment media condition (mTeSR(+)palmitate). This observation stands in stark contrast to the other cytosolic NADPH producers ME1 and IDH1, whose fluxes were virtually unchanged between the media conditions. Similar trends were observed experimentally [129] when the study authors performed isotopomer spectral analysis on quantitatively labeled [3-$^{2}$H]glucose transfer to palmitate; this enabled quantitative estimation of cell reliance on oxidative pentose phosphate pathway fluxes. Experimentally, oxidative pentose phosphate pathway activity accounts for ~52-67% of the cytosolic NADPH pool in H9 and HUES 9

hESCs in chemically-defined culture media (E8), which represents a significant proportion even when compared to other highly proliferative cell types, such as cancer cells. Oxidative pentose phosphate activity is expected to be higher in proliferative phenotypes because of the high nucleotide and fatty acid biosynthetic demand. These results collectively suggest a critical function in lipid metabolism and are supported by the known role of NADPH in lipid biosynthesis as a provider of cytosolic reducing equivalents. In our analysis of the FVA results, we noted a global increase in TCA cycle flux upon palmitate supplementation, although not statistically significant (p-value = 0.2635). However, closer inspection reveals 4.61 and 6.18-fold increases in $\alpha$-KGDH and citrate synthase (CS) flux, which is significant compared to other pathway reactions (p-value = 0.0542). The increase in these specific TCA cycle fluxes suggests that mitochondrial glutaminolysis and reductive carboxylation processes are upregulated as a consequence of palmitate media supplementation, which is consistent with the observations from studies performed in [129] via stable isotope tracing of [1-$^{13}$C]glutamine with measured increases in 2-HG abundance. The results collectively suggest that palmitic acid culture media supplementation regulates cell lipogenic activity and distinct reactions within the oxidative metabolism subsystem.

Furthermore, the model results replicated the H9 cell lines reliance on G6PDH-dependent NADPH flux for the maintenance of lipid pool under chemically defined media formulations (E8 and mTeSR). While the addition of palmitate induced no simulated changes in fatty acid oxidation, there was a slight increase in lipid biosynthesis observed. This outcome is supported by experimental isotope labeling data [129], which showed an increased percentage of labeled M+16 fatty acids in HUES9 and H9 hESCs cultured in E8+BSA-bound [U-$^{13}C_{16}$] palmitate and 1 mM carnitine. Interestingly, FVA simulations

of mTeSR(+)AlbuMAX revealed increases in both $\beta$-oxidation and lipid biosynthesis pathway fluxes when compared to the mTeSR media condition. Gas Chromatography/mass Spectrometry (GC/MS) analysis reveals decreases in percent newly synthesized palmitate and cholesterol under AlbuMAX-supplemented conditions. While this observation was not specifically supported by the isotope labeling data the simulation results still provide insight into the cell's reliance on certain metabolic pathways, even when supplemented with unique combinations of metabolites from the same class (unsaturated fatty acids).

We next sought to examine changes in media metabolite and amino acid consumption that result from culture media composition modification. No appreciable changes were observed when media component uptake rates (or exchange reaction flux magnitude) was compared between control and AlbuMAX-supplement culture media conditions; however, closer observation reveal significant differences between glutamine and glutamate metabolite uptake rates associated with control and palmitate-supplemented media conditions. Glutaminolysis is defined on a high-level as glutamine uptake minus glutamate secretion.

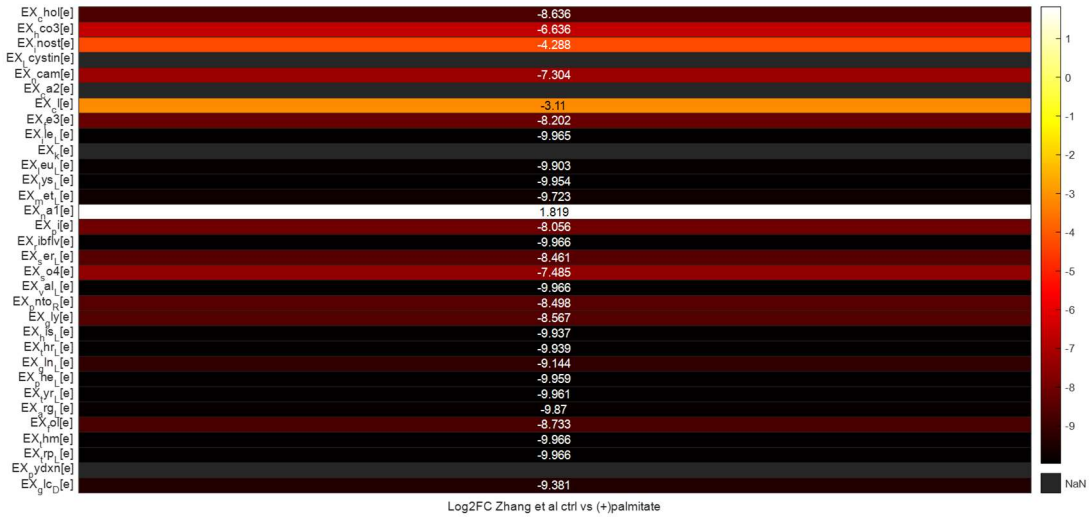


**Figure 4-2.Log2-fold change exchange reaction comparison between control mTeSR media and (+)palmitate culture media. Negative values denote greater flux in control cell culture media and positive values denote greater flux in '(+)palmitate' cell culture media conditions**

Log 2-fold change comparison reveals significant glutamate flux rates in treatment condition compared to control media conditions; since the model syntax represents greater uptake as more negatively valued fluxes then the interpretation from the model output is that the treated cells ***secrete*** more glutamate (**Figure 4-2**). When we combine this observation with the calculated decreased glutamine ***uptake*** flux in palmitate treated cells relative to control media conditions the model validates the observed reliance on glutaminolysis under chemically defined culture media conditions, as the authors observed a 4-fold increase in glutaminolysis in chemically defined media with respect to the treatment condition. Overall, we concluded that the model recapitulates differences in specific metabolic reaction and subsystem flux differences in hiPSCs that occur because of specific media compositions.

### *4.3.3 Tohyama et al Case Study*

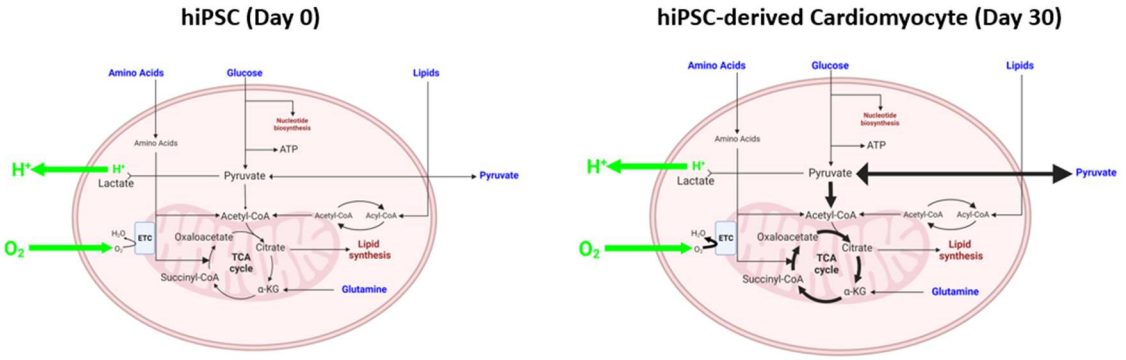


**Figure 4-3. Overall case study schematic shows relative changes to metabolic profile between hiPSCs and hiPSC-CMs in glucose/glutamine-withdrawn culture media.**

Metabolic selection has been implemented to directly control cell phenotype during *in vitro* hiPSC-CM differentiation; interestingly, this process also indirectly induced functional maturation of the downstream differentiated cardiomyocytes [135]. In the next case study selected to test the features of our media-specified, genome-scale flux analysis framework, the authors initially observed that PSC anabolic processes had been covered extensively in previous studies [136] but contrasting catabolic processes had received comparatively little attention. Therefore, they sought to further investigate media composition to reveal necessary metabolite precursors to hESC and hiPSC anabolic processes. To this end, the authors cultured hiPSCs in a modified high-glucose DMEM media (no lactate, pyruvate, or fatty acids) plus insulin-transferrin-selenium for control conditions; composition of the media was initially simplified one amino acid at a time with subsequent alkaline phosphatase (ALP) staining to determine hESC dependence on non-essential amino acid (NEAA) culture presence (**Figure 4-3**). Glucose (glc), glutamine (gln), cysteine, arginine, serine, and glycine collectively were found to be important for hESC survival, but media withdrawal of any component individually mostly had no impact on cell survival. In contrast, glutamine withdrawal under glucose-replete media conditions

led to complete hESC and hiPSC colony death within 48 hours. Therefore, they decided to specifically focus on glucose and glutamine metabolism. The authors tested various DMEM-based culture formulations in which they withdrew glucose for the '(-)glc' culture condition and withdrew both glucose and glutamine for the '(-)glc/gln' culture condition.

To replicate these conditions, we performed FVA simulations for the following culture media compositions: mTeSR, mTeSR (-) glucose, mTeSR (-) glucose and glutamine. We subsequently sought to compare similarities and differences in predicted metabolic pathway and reaction flux between the model and experimental observations. Through capillary electrophoresis and mass spectrometry (CE-MS)-based metabolome analysis, the authors reported that glucose-supplemented culture media conditions increased glycolytic and pentose phosphate pathway metabolite products, regardless of glutamine presence or absence. Similarly, our model simulation results reflected similar behavior, with the control mTeSR media conditions yielding increased glycolytic flux with respect to the glucose withdrawn mTeSR media condition (mTeSR(-)glucose) (**Figure 4-4**). Importantly, all previously developed bioinformatic-based constraints, in addition to media-based and fluxome-based model constraints, were required to elucidate the experimentally observed shifts in metabolic network activity. Model simulations in which only the original omics constraints were implanted revealed no differences in glycolysis, pentose phosphate pathway, TCA cycle, or ETC flux. This finding supports the hypothesized enhanced model flux predictive accuracy under the combined constraints, and increases confidence in metabolic profile prediction extension to novel media formulations. One of the main study objectives is the prediction of metabolic activity under

specific media formulations, so these simulation outcomes represent a critical step to achieving model-guided hiPSC media formulation based on target metabolic profiles.

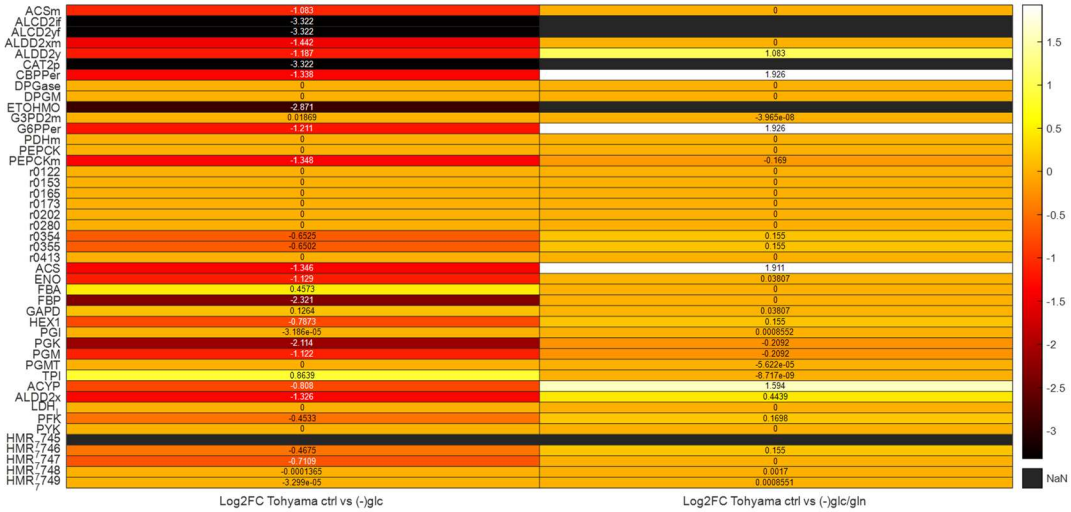


**Figure 4-4. Log2-fold change comparison of glycolytic flux reactions in (left) control media vs (-)glucose and (right) control vs (-)glucose/glutamine culture conditions**

We observed significant changes in glycolytic reaction fluxes between control and glucose-withdrawn mTeSR culture media conditions (p-value = 1.83e-4), as well as between control and glucose/glutamine-withdrawn media conditions (p-value = 2.64e-4). We next focused on oxidative metabolism, specifically the TCA cycle and electron transport chain (ETC). In the study, the researchers performed metabolome analyses in unlabeled Gln-supplemented culture media supplemented with [U-$^{13}$C]-labeled Glc ($^{13}C_6$-Glc) radio-labeled tracers and in unlabeled Glc-supplemented culture media further supplemented with [U-$^{13}$C]-labeled Gln ($^{13}C_5$-Gln) radio-labeled tracers. They observed that a majority of generated pyruvate was derived from the radio-labeled glucose and that most of TCA cycle intermediates were derived from radio-labeled glutamine ($^{13}C_5$-Gln), as indicated by fraction derived from $^{13}C_6$-Glc or $^{13}C_5$-Gln. To further analyze hESC

OXPHOS dependence, they utilized a SeaHorse flux analyzer to evaluate glycolytic and mitochondrial respiration under the previously described culture media conditions. They observed that baseline OCR was higher in Gln-supplemented media conditions, independent of glucose availability. Interestingly, we only observed significant differences in both TCA cycle (p-value = 0.038) and oxidative phosphorylation (p-value = 0.0025) reaction fluxes when we compared the control and glucose-withdrawn culture media conditions (**Figure 4-5**). Some of the most dramatic flux differences occurred for the ATP-citrate lyase (ACITL), 2-$\alpha$-ketoglutarate dehydrogenase (AKGDm), and succinate dehydrogenase (SUCD1m) reaction fluxes.

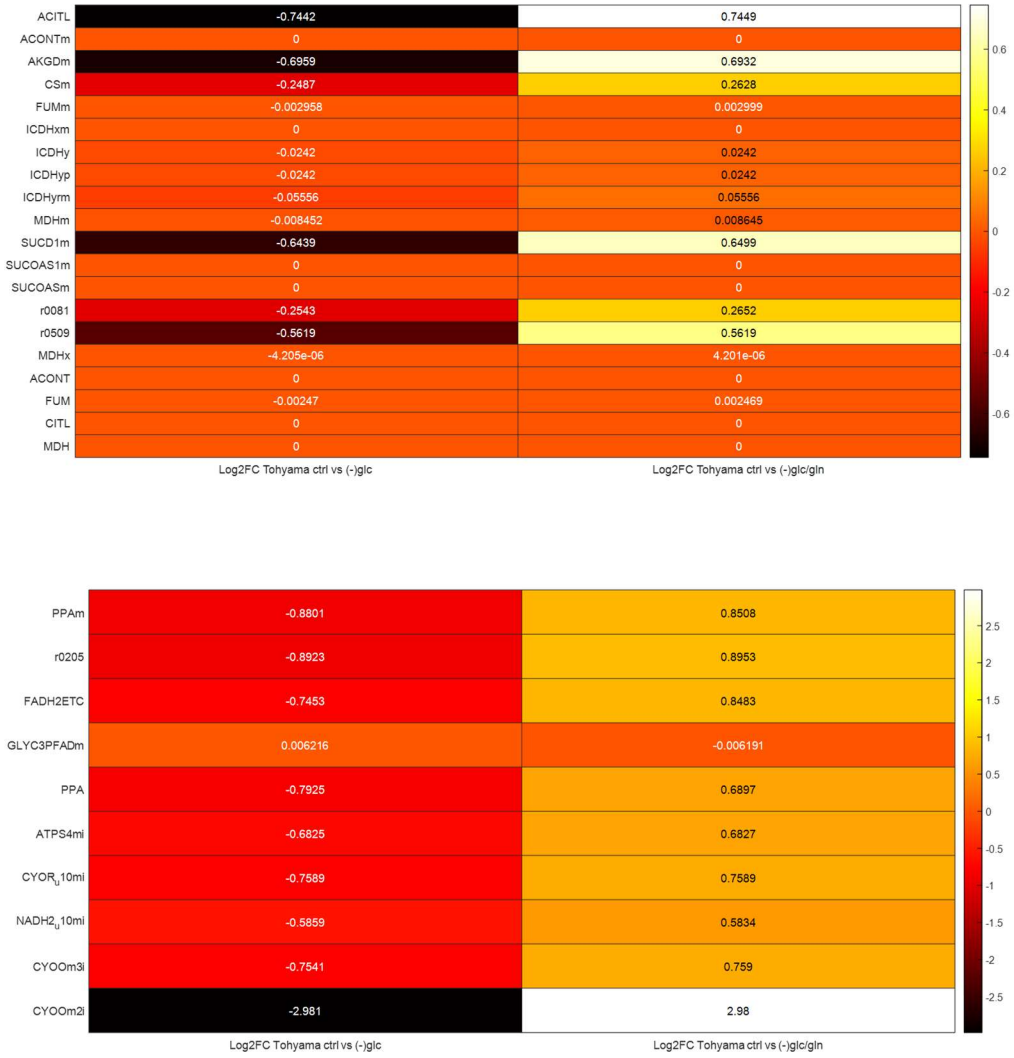


**Figure 4-5. TCA cycle and Oxidative phosphorylation (ETC) comparison Log2-fold change comparison figure. Top: The comparative fluxes between control and '(-)glc/gln' culture conditions are shown for the TCA cycle. Bottom: The comparative fluxes between control and '(-)glc/gln' culture conditions are shown for oxidative phosphorylation**

The significant change in succinate dehydrogenase (SUCD1m) flux reflects a possible explanation for this differential reliance, as SUCD1m directly links the TCA cycle to the electron transport chain (ETC) via the production of reducing equivalents $FADH_2$. Also, ATP-Citrate lyase (ACITL) has been previously shown to link glucose and glutamine metabolism [137], and 2-oxoglutarate dehydrogenase (AKGDm) acts directly downstream

of glutamine in the metabolite interconversion process, so significant changes to these specific reactions make logical sense, given the available culture media components.

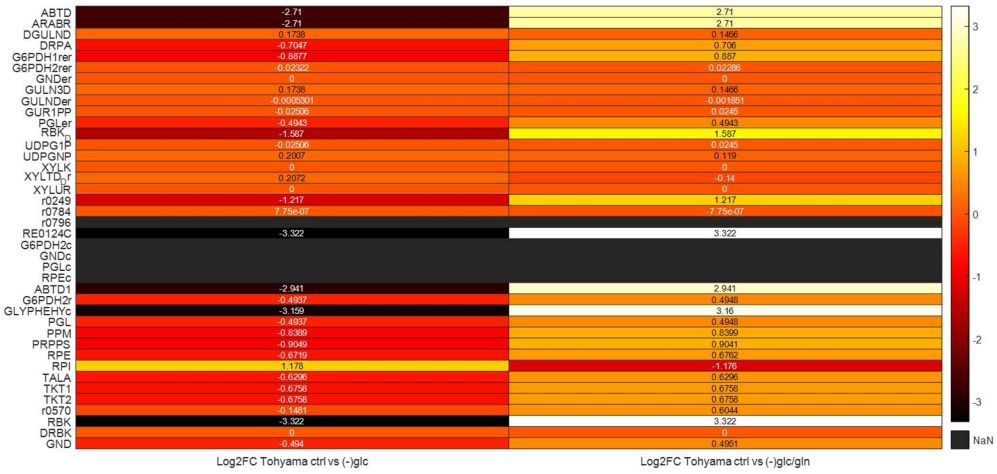


**Figure 4-6. This heatmap compares pentose phosphate pathway reaction flux log2-fold change comparison between control and palmitate-supplemented media conditions. Negative values denote greater flux in control media and positive values denote greater flux in (left) '(-)glc' or (right) '(-)glc/gln' media conditions**

We observed significant changes in pentose phosphate pathway subsystem flux under both culture conditions (p-value = 5.72e-5 and 3.03e-4, respectively) (Figure **4-6**) shows that most PPP reaction fluxes decrease upon glucose withdrawal, which is expected as glucose is a major source of intermediate metabolites. This observation was also supported by CE-MS-based metabolome analysis. We next sought to assess differences in metabolic flux that result from cell phenotypic differences. To this end, we recapitulated the media-based metabolic purification studies performed for hPSCs (day 0) against hPSC-derived cardiomyocytes (day 30). The authors initially maintained both cell types in the previously defined high-glucose DMEM and observed increases in oxidative metabolic process for hPSC-derived cardiomyocytes (hPSC-CMs). Our model results support the experimental findings, as **Figure 4-7** shows significant increases in both glycolytic and

oxidative metabolic process. The authors next compared phenotypic metabolic flux differences in glucose- and glutamine- replete culture media conditions. They observed that TCA cycle activity still could effectively generate ATP; interestingly, objective value comparison from our simulated results supports these observed trends. Simulation results show that the in DMEM culture media (control) ATP production objective value was ~37.4 mmol/(gDW-hr), and this value remained the same even in glucose- and glutamine-replete culture media conditions. However, hiPSC (day 0) ATP production objective value was ~38.8 mmol/(gDW-hr) in DMEM control media but was only ~6.57 mmol/(gDW-hr) in glucose and glutamine-withdrawn culture media condition simulations. Our observation not only reflects hPSC bioenergetic reliance on glucose and glutamine, but also cardiomyocyte metabolic flexibility under various defined media conditions [117]. We also replicated a lactate-based DMEM media condition in our computational simulations and observed no change in overall metabolic profile when compared to DMEM(-)glucose and glutamine simulation outcomes. This outcome of our model is consistent with literature reports that hPSC-derived cardiomyocytes can effectively utilize lactate or pyruvate as an alternate energy source [138; 135].

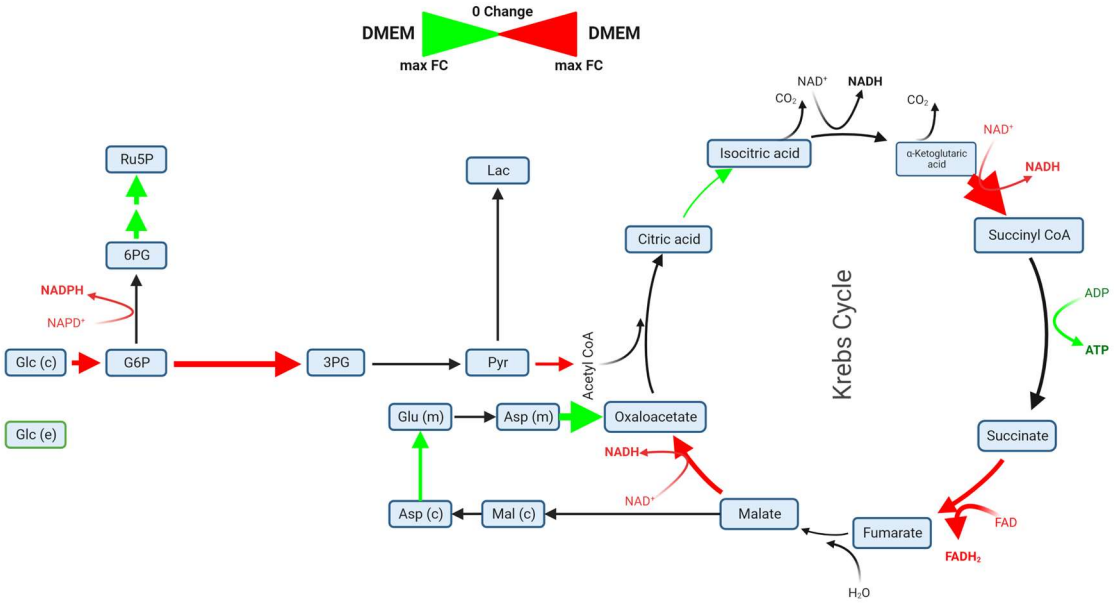


**Figure 4-7. Pluripotent (D0) vs immature cardiomyocyte (D30) comparison metabolic flux comparison; fluxes highlighted in red reflect greater reaction flux at day 30 and fluxes highlighted in green reflect greater reaction flux at day 0**

Finally, we compared exchange reactions between the cardiomyocyte and pluripotent phenotypes to test the experimental observations that cardiomyocytes are less reliant on non-essential amino acid metabolism [116]. This notion is supported by simulation outcomes from both control and glucose/glutamine-replete media conditions (**Figure 4-8**). Some of the most highly consumed hPSC metabolites (i.e., methionine, arginine, serine, valine, isoleucine) were found experimentally to be required for cell viability, via ALP staining.

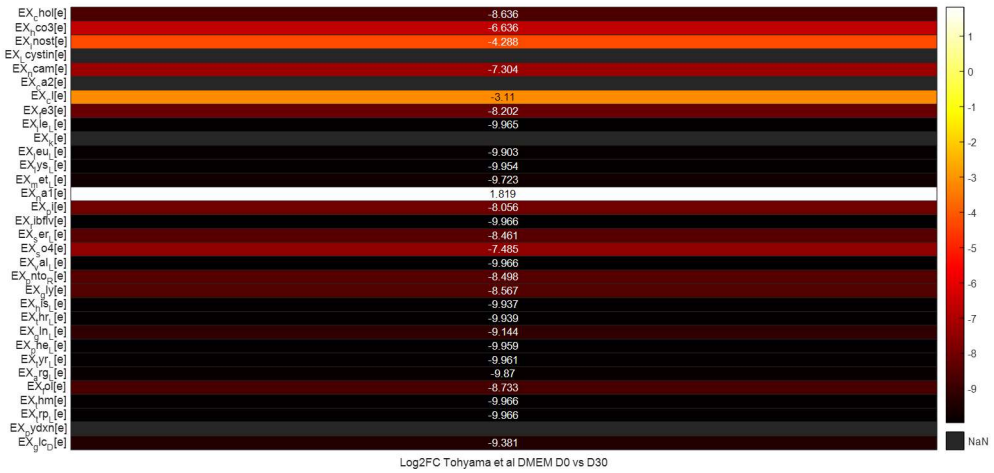


**Figure 4-8. Metabolite uptake comparison in pluripotent (D0) vs immature cardiomyocyte (D30) phenotypes. Negative values denote greater flux in control media and positive values denote greater flux in (left) '(-)glc' or (right) '(-)glc/gln' media conditions**

### *4.3.4 WTC11 scRNA-seq data analysis and differentiation insights*

Motivated by the previous analyses on published differentiation studies that yielded insights on the critical role of alternative amino acid sources for glutaminolysis during cardiomyocyte differentiation, we conducted a study in which WTC11 cells were cultured under standard RPMI conditions according to the Lian et al protocol or RPMI1640(+)L-glutamine/L-ascorbic acid. Transcriptomic data was collected by scRNAseq as described in section 4.2.2.3. After initial processing and quality control we performed differential expression analysis for our timepoint-specific differentiation cell samples (**Figure 4-9**). We specifically compared expression of known hiPSC-CM differentiation phenotype biomarkers to those present in our cell samples from differentiation days 0, 4, and 10. We observed expected POU5F1 (or OCT4) clustering on the left-hand portion of feature space and TNNT2 and ISL1 cardiomyocyte marker clustering in the upper middle portion of feature space. We sought to uncover new information about the transcriptomic landscape of our collected hiPSC-CM differentiation samples. Therefore, we next performed a

density-based dimensional reduction analysis, UMAP, to further elucidate defining biomarkers from our hiPSC-CM differentiation cell samples.

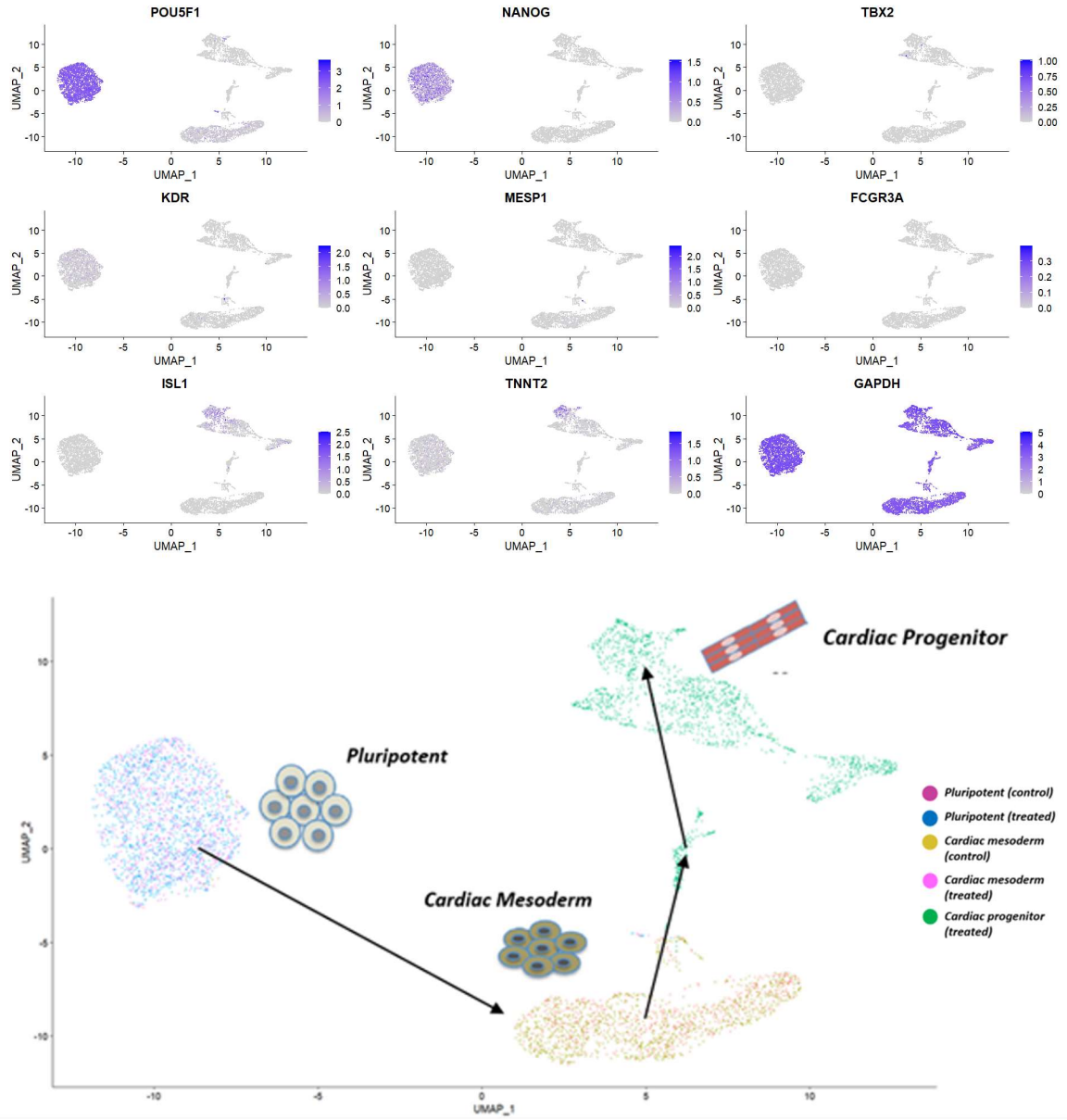


**Figure 4-9. (top) UMAP analysis shows distinct spatial clustering with respect to early hiPSC-CM differentiation phenotypic biomarkers. (bottom) UMAP analysis shows that scRNA-seq samples obtained during hiPSC-CM differentiation occupy distinct spaces in high-dimensional feature space**

The high-dimensional UMAP analysis, shown in **Figure 4-9**, revealed phenotype-specific occupation of specific spatial regions within high-dimensional feature space. The application of known transient phenotypic markers throughout hiPSC-CM differentiation

was used to elucidate a defined, "U-shaped" pseudo-time trajectory through which cells progressed to become cTnT- and Isl1-expressing immature cardiomyocytes. Based upon the similarity in clustering between treated and untreated samples from a given stage of differentiation, we combined the single cell transcriptomics into three classes: pluripotent (day 0), cardiac mesoderm (day 4), and cardiac progenitor cells (day 10). We next performed a differential expression analysis using the Seurat differential expression pipeline. We sought to observe unique defining biomarkers for the pluripotent, cardiac mesoderm, and cardiac progenitor phenotypes. For each phenotype, a pairwise comparison between it and the combined transcriptomics of the other two stages of differentiation was performed. This was conducted iteratively for a multi-class differential expression analysis.

**Table 4-2. Top Differentially Expressed Pluripotent Population Markers compared to combined set of cardiac mesoderm and cardiac progenitor cells**

| Gene | p-value | Log2-fold change (avg) | p-value (adjusted) |
|---|---|---|---|
| L1TD1 | 1E-400 | 4.908 | 1E-400 |
| FOXD3-AS1 | 1E-400 | 3.320 | 1E-400 |
| S100A10 | 1E-400 | 2.604 | 1E-400 |
| EPCAM | 1E-400 | 3.143 | 1E-400 |
| TDGF1 | 1E-400 | 4.134 | 1E-400 |
| POU5F1 | 1E-400 | 4.293 | 1E-400 |
| AL353747.4 | 1E-400 | 2.151 | 1E-400 |
| RARRES2 | 1E-400 | 2.429 | 1E-400 |

Traditionally, markers such as POU5F1 (or OCT4), NANOG, have been used to identify the pluripotent phenotype. Cells in our pluripotent sample population (603,000 cells) reveals POU5F1 (p-value adjusted: 1e-400) and NANOG (p-value adjusted: 3.83e-282) to be among the most highly differentially expressed genes when compared to cardiac mesoderm (1,377,000 cells) and cardiac progenitor phenotypic (1,020,000 cells) populations, as expected. We next more closely inspected the hypothesized cardiac mesoderm phenotype. Traditionally, markers such as Flk-1 and MESP-1 have been used to identify this phenotype. Interestingly, we observed FRZB (p-value adjusted = 2.15e-

286) and CDH2 (p-value adjusted = 6.09e-257) to be among our most highly differentially expressed genes for our scRNA-seq samples, as shown in **Table 4-2**. Soluble frizzle-related proteins are known to be closely associated with Wnt signaling as upstream effectors, and likely associated with the timed IWP2-induced Wnt pathway inhibition. Also, CDH2 expression is related to biomechanically mediated cell sorting during morphogenic processes. This biomechanical signaling is orchestrated by the cell-cell adhesion process and has been previously implicated in embryonic development [139]. This notion is supported by outcomes from gene set enrichment analysis (GSEA), as shown in **Figure 4-9.**

**Table 4-3. Top Cardiac Mesoderm differentially expressed markers compared to combined set of pluripotent and cardiac progenitor cells**

| Gene | p-value | Log2-fold change (avg) | p-value (adjusted) |
|---|---|---|---|
| SIX3 | 1E-400 | 4.908 | 1E-400 |
| LIX1 | 1E-400 | 3.320 | 1E-400 |
| DLK1 | 1E-400 | 2.604 | 1E-400 |
| PRTG | 1E-400 | 3.143 | 1E-400 |
| FRZB | 6.412E-291 | 4.134 | 2.572E-281 |
| GPC3 | 7.668E-286 | 4.293 | 2.572E-281 |
| MAPK10 | 1.405E-285 | 2.151 | 4.711E-281 |
| CDH2 | 1.851E-261 | 2.429 | 6.086E-257 |

We also observed SIX3 to be among our top differentially expressed genes in the cardiac mesoderm population (p-value adjusted = 1e-300) with respect to the pluripotent and cardiac progenitor populations (**Table 4-3**). SIX3 is a known regulator of Wnt signaling via repression of WNT1 expression. MAPK10 was also among the most highly differentially expressed genes (p-value adjusted = 4.71e-281). MAPK signaling plays multiple regulatory roles in many relevant cell processes, such as cell proliferation, differentiation, and transcriptional regulation.

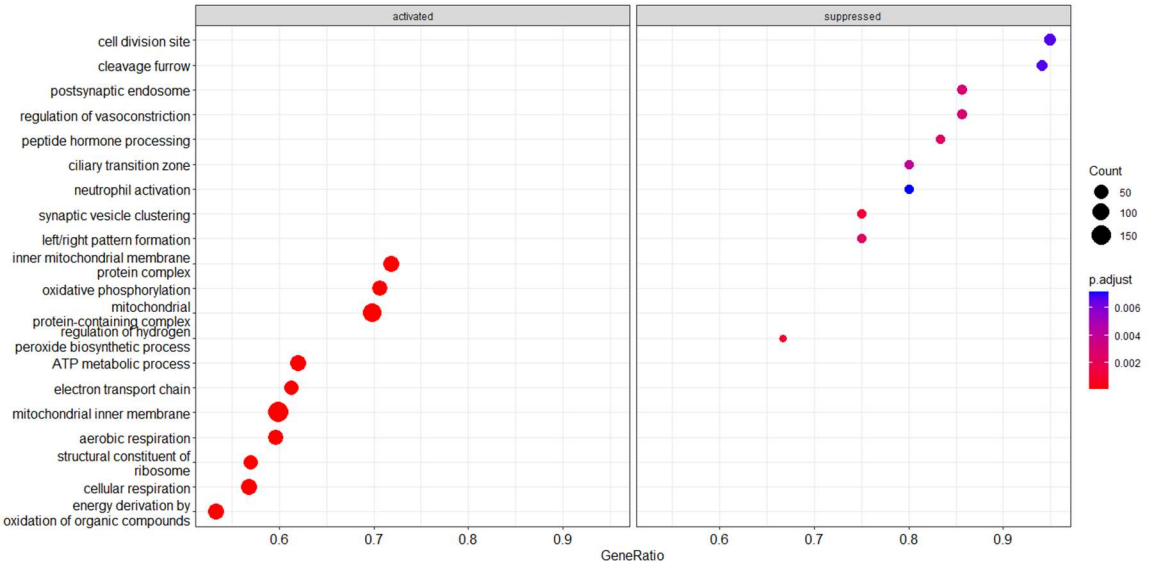


**Figure 4-10. Heatmap defining the active biological processes in pluripotent stem cells**

Many of these highly upregulated genes appear to be related to organogenesis and morphogenic processes, and our GSEA data supports this notion. For example, **Figure 4-10** shows 'animal organ morphogenesis', 'anatomical structure differentiation' and 'regulation of cell differentiation' processes enhanced in the cardiac mesoderm population, suggesting that co-differentiation may be occurring, despite occurring in a 2D monolayer differentiation context.

**Table 4-4. Cardiac Progenitor differentially expressed markers compared to combined set of pluripotent and cardiac mesoderm cells**

| Gene | p-value | Log2-fold change (avg) | p-value (adjusted) |
|---|---|---|---|
| NEAT1 | 1E-400 | 2.941 | 1E-400 |
| MEIS2 | 1E-400 | 1.733 | 1E-400 |
| ZFHX3 | 1E-400 | 1.506 | 1E-400 |
| FREM2 | 2.076E-306 | 2.089 | 6.961E-302 |
| ANXA2 | 5.577E-291 | 2.5908 | 1.870E-286 |
| SEMA3C | 1.894E-302 | 1.309 | 6.352E-298 |
| DLX5 | 1.564E-282 | 1.522 | 5.245E-278 |

We next focused on the cardiac progenitor (day 10) gene expression (**Table 4-4**). Many of the top differentially expressed genes were not found to be directly related to

processes associated with cardiogenesis (**Figure 4-11**), but MEIS2 has been implicated as a master regulator of HOX protein expression, and HOX regulation has been associated with cell fate decisions in cardiomyocyte differentiation in a previous study [140].

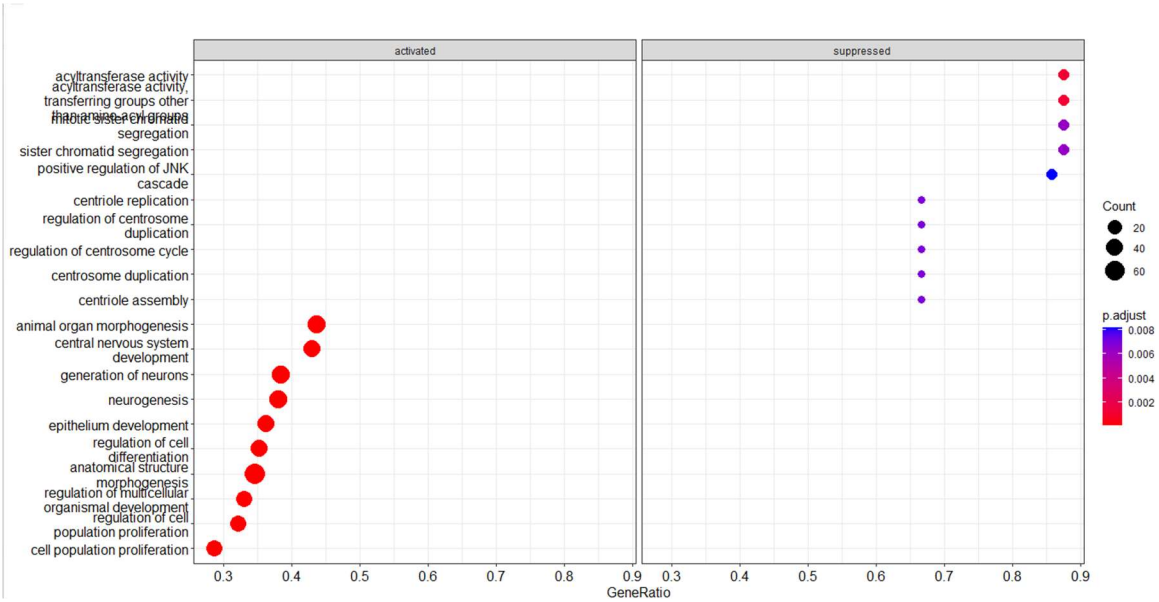


**Figure 4-11. This heatmap defines the active biological processes in cardiac mesoderm cells**

Furthermore, ANXA1 was found to be among the most highly differentially expressed genes in this sub-population. ANXA1 is associated with $Ca^{2+}$ binding activity regulation, and calcium cell influx is known to precede action potentials in cardiomyocytes and other excitable cells.

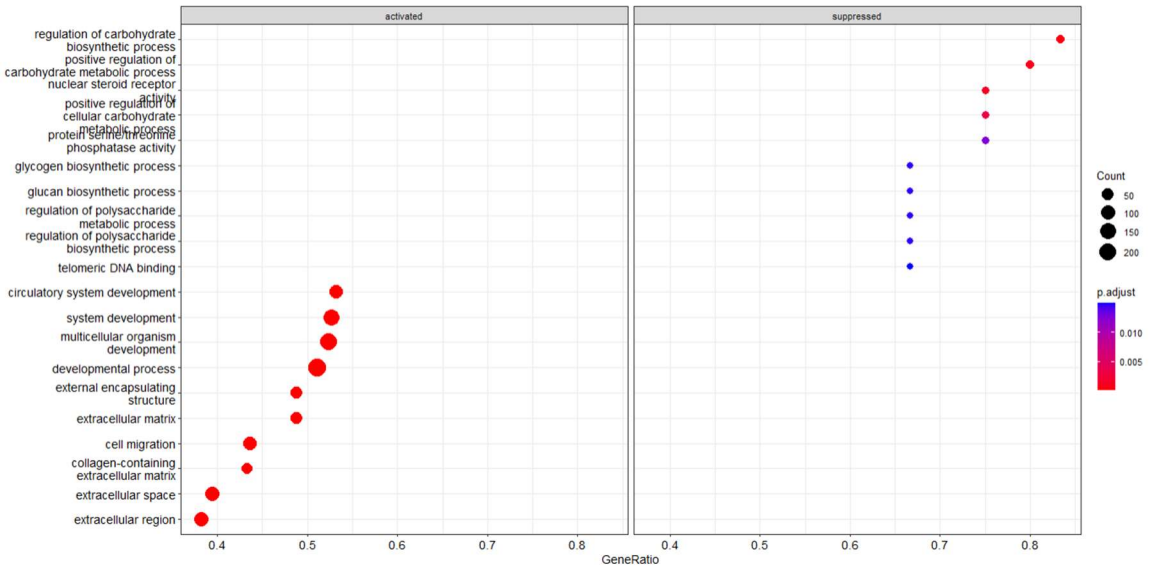


**Figure 4-12. This heatmap defines the active biological processes in cardiac progenitor cells**

GSEA reveals some of the most highly upregulated biological processes in this population as 'circulatory system development' and 'collagen-containing extracellular matrix', as shown in **Figure 4-12**. The 'circulatory system development' appearance was to be expected, as cardiogenesis falls under this category. However, it was interesting to find 'collagen-containing extracellular matrix' to be among the most highly upregulated biological processes, as one of the hypothesized beneficial side effects of ascorbic acid cell culture supplementation is the increased structural composition in the form of collagen expression [141]. Finally, we performed an "unsupervised" sample clustering on the collated cell samples. We determined that 5 sub-populations were sufficient to cover the variance present in the dataset, while still preserving uniqueness of newly identified sub-populations. Interestingly, we found that one of the derived groups had a very similar transcriptional landscape to that of immature cardiomyocytes. Cardiac troponin T (TNNT2) is known a key defining cardiomyocyte biomarker, and also happens to be one of the most highly upregulated genes in the novel sub-population, as shown in **Table 4-5**.

Furthermore, another highly expressed gene, TAGLN is known to be associated with calcium binding and actin cross-linking. The well-defined cardiomyocyte contraction mechanism involves calcium-mediated actin and myosin activation. Furthermore, calcium-activated ion channel expression (KCNMA1) appeared to be one of the defining features of this sub-population, which further supports its hypothesized role in cardiac maturation. We also observed upregulation of specific biomarkers pertaining to improved structural capacity of cardiac progenitor cells.

**Table 4-5. Unsupervised sample clustering reveals novel cardiogenic biomarkers**

| | |
|---|---|
| Positive | COL3A1, TGFBI, GABRP, LUM, TNNT2, KCNMA1, HAND1, LINC02381, ACTC1, COL1A1, MMP2, EPAS1, LOXL2, COL5A1, ARSI, LPCAT2, DCN, SLN, MTUS2 |
| Negative | HAPLN1, SEMA3E, MKI67, TOP2A, SFRP4, CENPF, CRDNE, SULT1E1 |

Collagen protein isoforms COL3A1 and COL1A1 are among the most highly differentially expressed genes and MMP2 is a well-known enzymatic regulator of the extracellular environment, biomechanical properties, and signal transduction. MMP overexpression has been shown to promote cell adhesion to collagen, which suggests both processes may be important in this phenotype. The pipeline that integrates transcriptomic-based estimation of cell enzyme abundance represents one of the most important advancements in genome-scale FBA modeling efforts [125], as it enables personalized metabolic modeling efforts and ensures that generated solution fluxes are more physiologically relevant and accurate. Therefore, we hypothesized that FVA simulations incorporating our novel combined omics, media, and fluxome constraints solutions will enable insights into potential metabolic pathway, reaction, or media component targets for desired control of metabolic profile and phenotypic outcomes.

### *4.3.5 Analysis of Simulated Metabolic Transitions though early hiPSC-CM Differentiation*

The start of differentiation in mouse and human PSCs is accompanied by a well-known shift from glycolytic to oxidative metabolism [166; 44]. However, we sought to utilize transcriptomic data and FVA simulations to better understand to metabolic flux signatures associated with the transition from pluripotency to mesoderm lineage, as specific extra-embryonic phenotypes contain unique metabolic profiles [142; 115; 143]. Therefore, we utilized single cell RNA sequencing datasets produced from our differentiation samples at days 0, 4, and 10 of the directed hiPSC-CM differentiation as transcriptomic model input for downstream reaction flux constraint. Even though we generated two separate samples for two of the three differentiation timepoints (distinguished by culture media treatment), we utilized the 'pluripotent (control)' transcriptomic dataset, 'cardiac mesoderm (control)' transcriptomic dataset, and 'cardiac progenitor (control)' transcriptomic dataset, based in observations from (**Figure 4-9**) that culture media did not significantly alter gene expression for the observed timepoints. Briefly, we process each sample individually before averaging gene expression for all cells sampled within a specific population. Finally, we performed the following simulations under mTeSR (day 0) and RPMI-160 (days 4 and 10) culture compositions. Subsequently, we performed simulations and observed increases in oxidative metabolic flux as the differentiation progressed from day 0 to day 4, although the observed changes were not significant. However, latter TCA cycle reaction fluxes did significantly increase from days 0 to 4. This supports experimental observations that glutamine oxidation becomes a more prevalent metabolic objective as cells transition to the mesoderm phenotypic state [112].

Moreover, we did observe statistically significant (p-value = 0.0918) changes in glycolytic metabolism between the days.

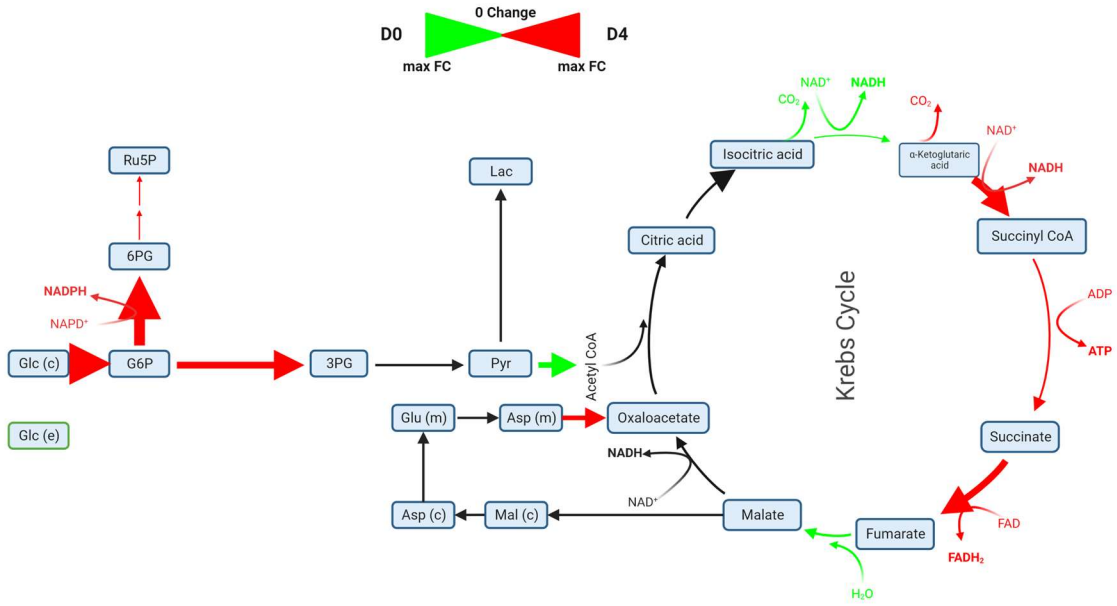


**Figure 4-13. Comparison of metabolic flux through central carbon metabolism in pluripotent (D0) and cardiac mesoderm (D4) phenotypes; fluxes highlighted in red reflect greater reaction flux at day 0 and fluxes highlighted in green reflect greater reaction flux at day 0**

**Figure 4-13 s**hows that flux through glycolytic reactions was more pronounced in pluripotency than at the early differentiation stages, which further supports the observed oxidative metabolic shift observed in multiple differentiation contexts.

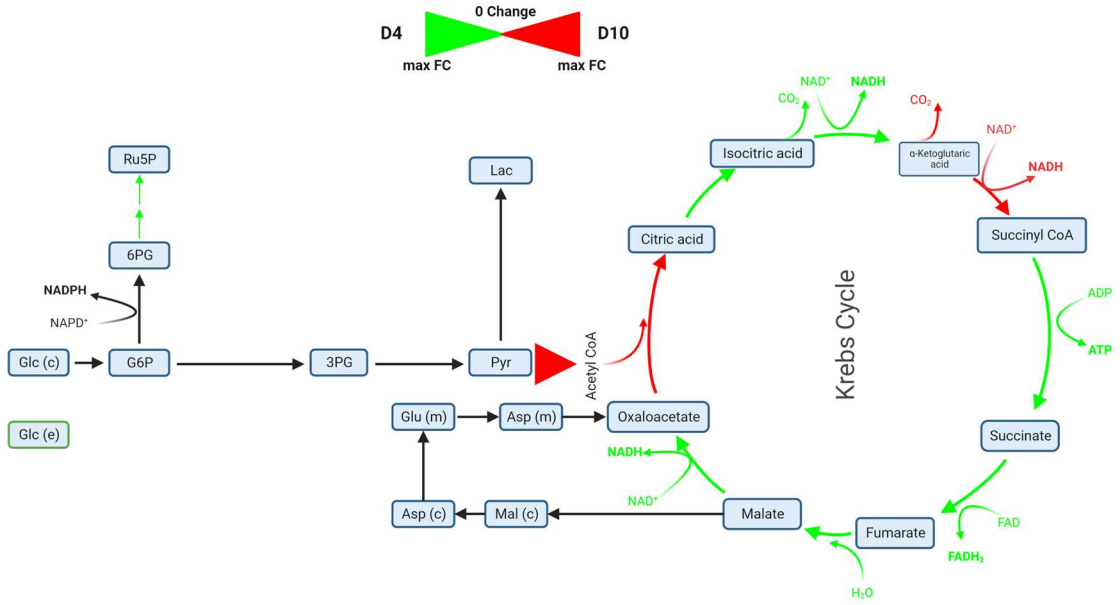


**Figure 4-14. Comparison of metabolic flux through central carbon metabolism in pluripotent (D4) and cardiac mesoderm (D10) phenotypes; fluxes highlighted in red reflect greater reaction flux at day 4 and fluxes highlighted in green reflect greater reaction flux at day 10**

From days 4 to 10, We observed a further continual increase in glycolytic flux. While this does not match the expected shift from glycolytic metabolism that accompanies cell differentiation (**Figure 4-14**), it does suggest that insulin-mediated glucose uptake could be responsible for this behavior, as insulin media supplementation begins on day 6

of the directed hiPSC-CM differentiation protocol [36].

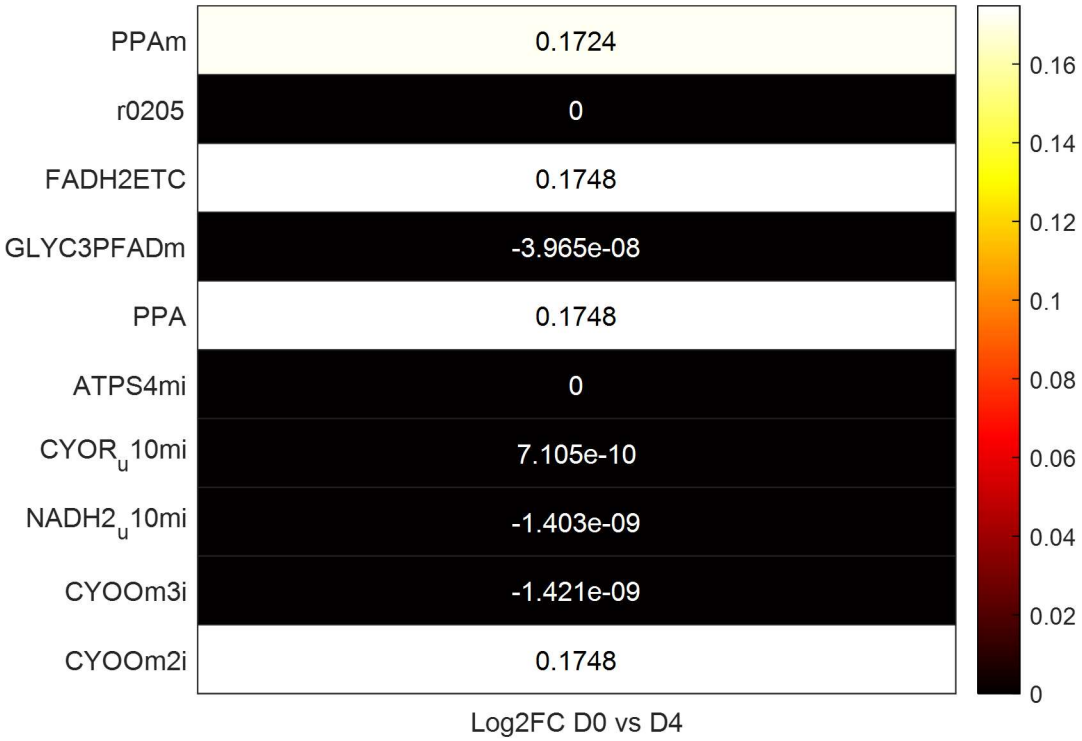


**Figure 4-15. Log2-fold change comparison of metabolic flux is the mesoderm (D0) vs. cardiac mesoderm (D4) phenotypes. Negative values denote greater flux at day 0 and positive values denote greater flux at day 4**

However, simulation outcomes show the changes to the TCA cycle mostly favour the mesoderm (day 4) phenotype. This observed effect could be occurring because of decreased mitochondrial protein expression at the beginning of PSC differentiation [144]. Furthermore, multiple groups have shown the differentiation media to contain high levels of glucose, which forces cells into a persistent high glycolytic metabotype. ETC flux outcomes in **Figure 4-15** show non-significant changes in metabolic flux that favour the cardiac mesoderm (day 4) phenotype, which aligns with the hypothesized shift from glycolytic to oxidative metabolism.

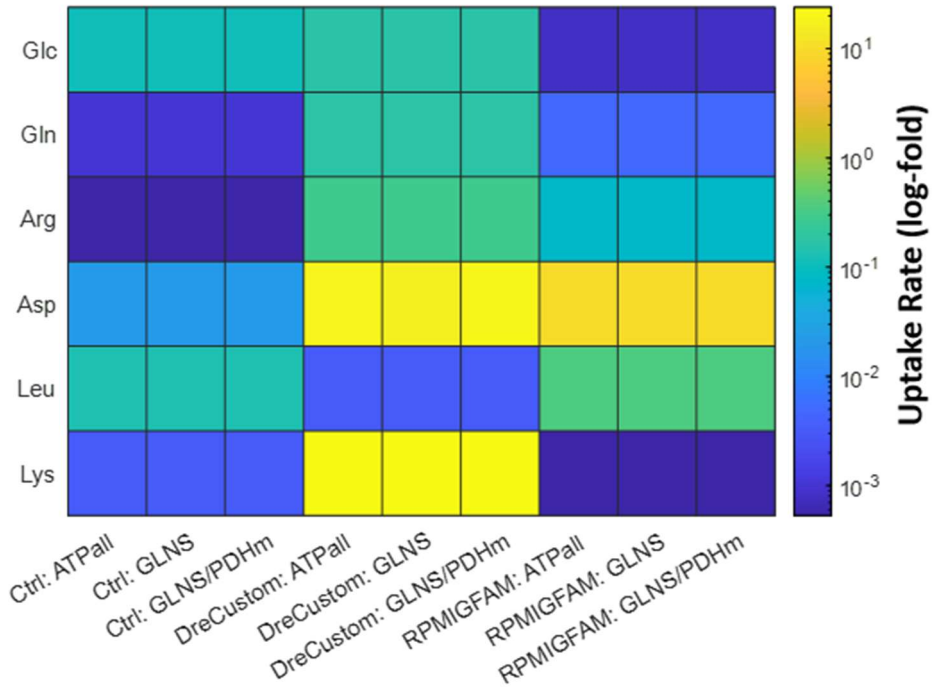


**Figure 4-16. Cardiac mesoderm (D4) metabolite uptake is compared across 3 media formulations: Control, 'DreCustom', and RPMIGFAM. Common non-essential amino acid uptake was compared for glucose (Glc), glutamine (Gln), arginine (Arg), aspartate (Asp), leucine (Leu), and lysine (Lys)**

We focused on exchange reaction rates for three culture medias: RPMI1640, RPMI1640(+)L-glutamine/L-ascorbic acid (or 'DreCustom'/'DRECUST'), and RPMI(+)L-galactose/oleic acid/palmitic acid (or 'RPMIGFAM'). Each of the culture media is designed to enhance hiPSC-CM differentiation efficacy and maturation and could potentially provide insights into which composite media metabolites cells prefer to accomplish cellular objectives. The 'DreCustom' media composition is defined in **Section 4.2.2.1**. The L-glutamine supplementation is hypothesized to increase metabolic flux through the latter TCA cycle reactions, which are responsible for generated the reducing equivalents NADH and $FADH_2$ for downstream electron transport chain function. The L-ascorbic acid is hypothesized to induce cardiogenesis through enhanced collagen production and cardiogenic markers [141; 167]. The 'GFAM' Media formulation was

design and utilized here because of the known shift *in vivo* from lactate to fatty acid substrate for energy metabolism [117]. The authors sought to mimic these metabolic shifts using a differentiation media supplemented with fatty acids and galactose, substrates that can be readily interconverted into metabolic pre-cursors for anaerobic respiration and $\beta$-oxidation. To gain a better understanding of important media composite metabolites required for different cell functions (or objectives) under these media formulations, we performed FVA simulations for the described media conditions by incorporating day 4 untreated sample scRNA-sequencing transcriptomic data to investigate the role of media composition on amino-acid uptake. Interestingly, we observed a shift in metabolite uptake preference for the day 4 cardiac mesoderm phenotype with respect to the day 0 mesoderm phenotype. **Figure 4-16** shows that the cells preferentially uptake lysine, aspartate, glutamine, and arginine, especially under the 'DreCustom' media treatment and this preference is independent of model objective function. Interestingly, a study suggests that supplementation of branched-chain amino acids, such as valine, isoleucine, and leucine, collectively contribute to mitochondrial biogenesis during cardiac maturation [145]. Collectively, these observations suggest that specific hiPSC-CM differentiation transitory phenotypes benefit to distinct culture media formulations. This result motivated additional experiments to test the differentiation phenotype under the DreCustom media compared to the standard iPSC-cardiomyocyte protocol.

### *4.3.6 SeaHorse Assay Outcomes*

The results from our FVA simulations suggest that L-glutamine and ascorbic acid supplementation can increase oxidative metabolic flux through the TCA cycle and electron transport chain. Therefore, we sought to experimentally validate changes in cell

bioenergetics in the presence of L-glutamine and L-ascorbic acid. We performed the directed hiPSC-CM differentiation [36] until day 10, where the cells are expected to obtain the cardiac progenitor/immature cardiomyocyte phenotype. We then performed a MitoStress XP test using a Seahorse XPf Flux Analyzer. The outcomes under control media conditions and treatment media conditions are shown below in **Figure 4-17**:

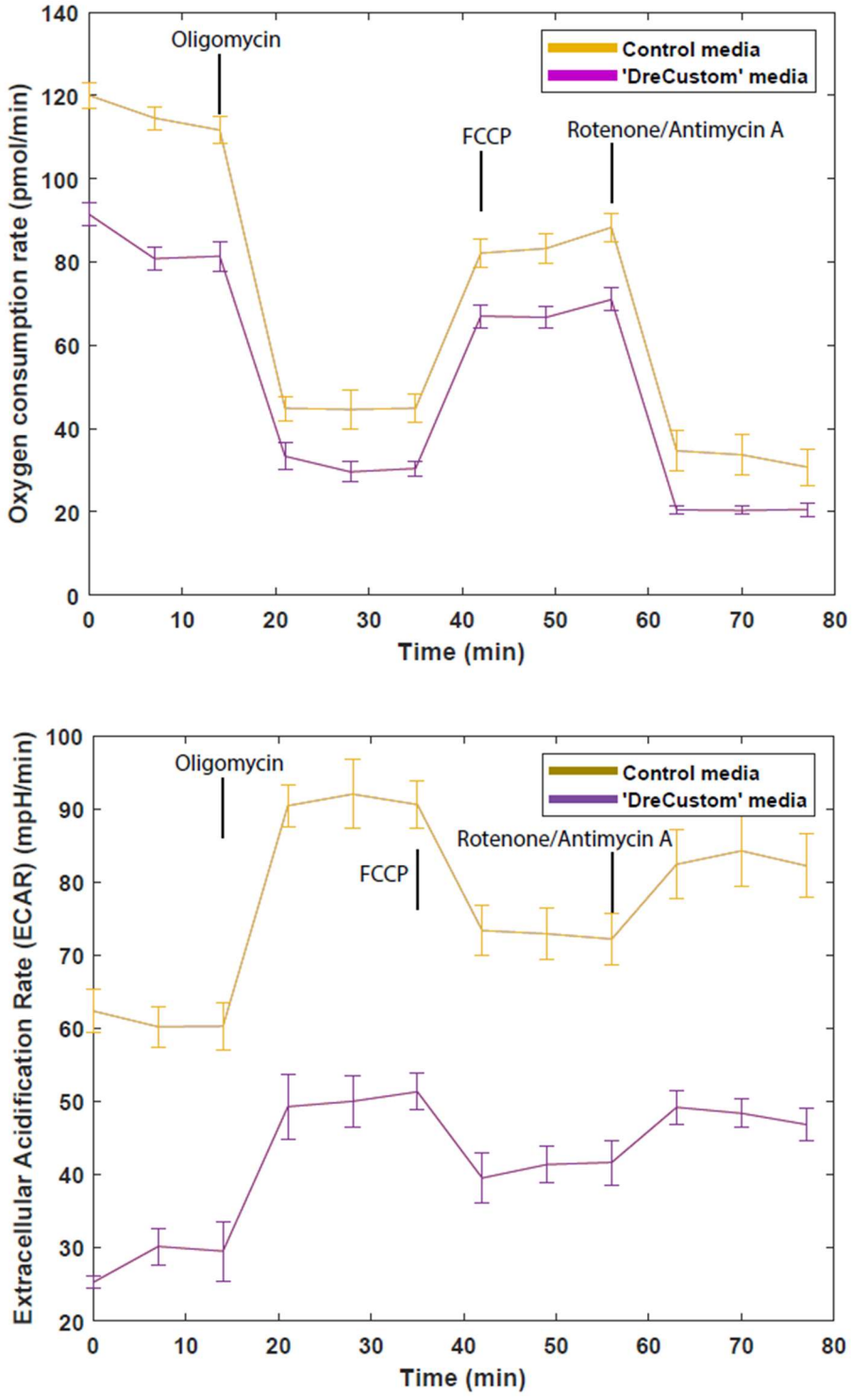


**Figure 4-17. The SeaHorse Assay Outcomes for the control media conditions are shown, along with outcomes from pharmacological perturbation of the electron transport chain (ETC); Basal OCR and ECAR measurements are taken from time point 0 to approximately 15 minutes; Oligomycin is added at approximately timepoint 15; FCCP is added at approximately timepoint 35**

The control culture media treatment resulted in a basal OCR of ~112 pmol/min/cells and ECAR of ~62 mpH/min/cells; the 'DreCustom' culture media treatment resulted in a basal OCR of ~93 pmol/min and ECAR of ~30 mpH/min/cells. While these results seem to present similar oxidative metabolic profiles, it is important to consider how aerobic and anaerobic metabolism are coordinating to obtain a complete picture of cellular bioenergetic profile. We also sought to further inspect the metabolic anaerobic to aerobic respiration activity shift that is hypothesized to occur.

**Figure 4-18** shows that the OCR:ECAR ratio for both control groups are ~2.667 and ~1.82**. Figure 4-18** shows that the OCR:ECAR ratio for both control groups are ~3.472 and ~2.6. These changes were found to be statistically significant (p-value = 0.008) between media treatment groups, which suggests that the L-glutamine and L-ascorbic acid supplementation yielded a significant improvement in mitochondrial respiration.

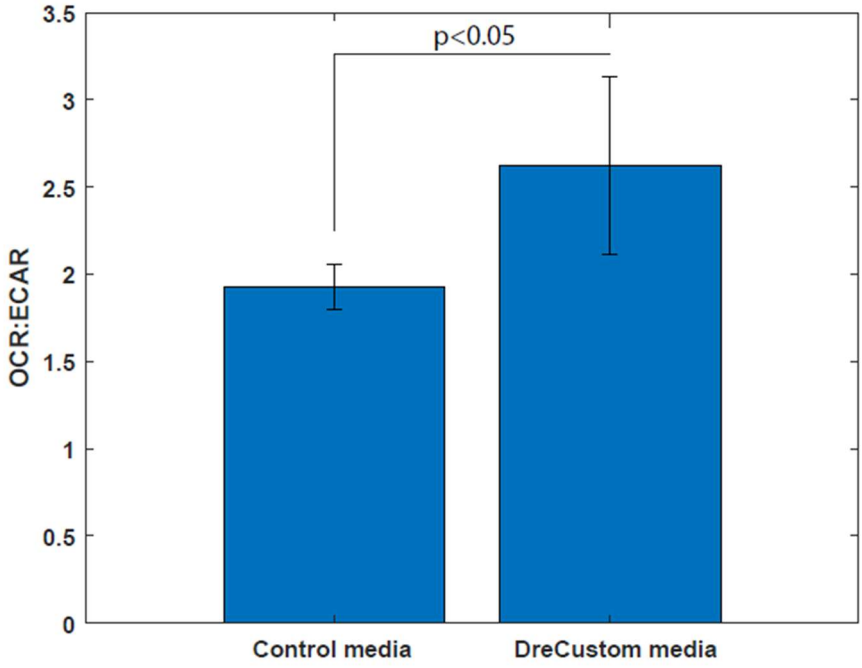


**Figure 4-18. OCR:ECAR ratio is shown for the Control culture media conditions and the 'DreCustom' culture media conditions (L-glutamine and L-ascorbic acid supplementation)**

## 4.4 Discussion

Current directed hiPSC-CM differentiation protocol advances have brought the cell manufacturing field closer to the realization of human cell-based therapies to treat cardiac conditions, but large-scale manufacturing efforts are limited by invasive quality control strategies and time- and resource-intensive cell culturing techniques. In this work, we found that computational simulations accurately predicted multi-scale metabolic signaling, given the correct omics and culture media-based model constraints. The models replicated previous experimentally observed changes in hiPSC/hESC and hiPSC-CM metabolic subsystem activity and single reaction fluxes that resulted from a variety of culture media modifications including changes in glucose content, lipid supplementation, and amino acid levels. We extended this knowledge to unexplored culture media conditions and cell phenotypes using single-cell RNA sequencing transcriptomic data and found novel media

metabolites that could potentially increase purity and maturation of resulting differentiated cells. We validated the potential of these novel media conditions to induce functional maturation with a metabolic respiration assay. One of the current drawbacks of hiPSC-CM differentiation is heterogeneity in purity and throughput across labs, even when the same iPS cell line is utilized. The lingering presence of pluripotent, non-differentiated cells, of course, presents a safety concern, as unreliable outcomes *in vitro* could lead to pathophysiological outcomes environments such as teratomas or aberrant electrochemical properties when engrafted in a patient. Therefore, another major focus in cell manufacturing is to determine specific cell signaling network hubs that would enable repeatable, robust outcomes in directed differentiations. One group has genetically engineered a hiPSC line that that forms pure, functional cardiomyocytes by inducing cardiac progenitor phenotypes via exogenous MYC expression [146]. Here, we sought to explore less invasive metabolite-based strategies in culture media to engineer cell fate. Metabolic control of cell fate offers a non-expensive, widely adoptable critical quality assurance approach to hiPSC-CM cell manufacturing.

By performing a comparative computational analysis of genome-scale metabolism across three individual published datasets, we observed several key commonalities in the metabolic reprogramming that occurred during PSC-to-cardiomyocyte differentiation. For example, comparison of modeling results from these studies indicate that pyruvate oxidation and glutamine oxidation represent critical targets for media-based metabolic engineering of hiPSC-CM differentiation. These metabolic targets can be modulated with culture supplementation of pyruvate and glutamine from days 0 to 2 or 4 of the hiPSC-CM differentiation. Furthermore, our model suggests new target metabolites for culture media

supplementation at distinct timepoints. At day 0 of the hiPSC-CM differentiation, cells showed a strong preference for leucine, lysine, and arginine uptake in both standard differentiation culture media and 'DreCustom' culture media. However, cells showed a preference for aspartate, lysine, arginine, and glutamine uptake day 4 of the differentiation. Moreover, simulation outcomes reflect that media conditions will affect preferred cell metabolite uptake 'decisions', as cells can readily interconvert multiple metabolite sources into pre-cursors for anabolic and catabolic cell objectives. The variety of reactions affected by one component being added to or withdrawn from culture media formulations motivates the approach of using a genome-scale model of human metabolism when assessing metabolic profiles. Had we chosen to focus on a select number of reactions to focus on within central metabolism, we could potentially lose insight into how specific environmental modifications (i.e., culture media composition) propagates throughout the interconnect metabolic system. Also, potential targets for pharmacological modification would potentially be missed. Furthermore, media composition is reflected by the upper bound constraints applied to metabolite transport between compartments (**Figure 4-16**); information that would remain hidden without analysis of the entire known human metabolic network. This is supported by simulation outcomes, as metabolite uptake does not vary between objective functions but instead various between differing culture media compositions. At the pre-mesoderm stage, the modeling results suggest an enhanced preference for lysine and aspartate in the 'DreCustom' media formulation. These study findings reflect the first steps to model-guided design of synthetically designed cellular systems.

Despite our promising model metabolic trend replications and novel insights, caution should be applied when translating findings to translational or clinical applications. One of the dual advantages and disadvantages of FBA is the simplistic representation of metabolic reactions. Not only are fluxes assessed strictly at steady state, but the model also misses important regulatory relationships and interaction with external signals. For example, it is well known that $\alpha$-KG levels directly impact histone H3K9m3 and H3K27m3 acetylation markers, which modulates PSCs between a naïve and primed pluripotent phenotype [44]. Furthermore, changes in [ADP]:[ATP] directly inactivates the AMPK/mTOR pathway in rodent embryos [147]. This modeling framework currently does not have the ability to track dynamic changes in metabolite levels throughout the course of simulation, although there are computational methods that exist that are suited to model these relationships, such as dynamic FBA. The day 10 model simulations reflect 'DreCustom' media-induced changes in TCA cycle and oxidative phosphorylation fluxes (i.e., mitochondrial fumurate), although not to a significant extent. It is important to consider that these observed outcomes were generated from simulations in which the previously defined SeaHorse-associated model constraints were not implemented, as that data was not readily available in literature resources or produced from our specific sample timepoints. These additional media- and fluxome-based novel model constraints were found to be critical in differentiating metabolic flux through oxidative metabolic reactions and may also be critical for reaction flux distinction in this context.

Overall, our results presented show the increased potential for hiPSC-derived cardiomyocytes to be implicated in translational cell therapies in a non-invasive manner. It was shown that culture media can be utilized as an avenue to coax cells into particular

metabolic flux distributions in a predictable manner. This is imperative because different phenotypes possess specific metabolic profiles, and we have shown the model's novel ability to predict metabolic profiles in hiPSCs and transient hiPSC-CM differentiation phenotypes under differing culture media formulations. Importantly, these predicted metabolic outcomes were shown for previously explored case studies as well as experimentally validated novel media conditions. Therefore, future model application in media-guided metabolic control of human stem cell metabolism becomes more realizable and provides a viable avenue for cell manufacturing strategies.

# CHAPTER 5. CONCLUSION

## 5.1 Thesis Contribution

In summary, we found that metabolic and bioelectric signaling can be utilized as tools to understand multi-level biological systems and to inform decisions on culture media composition *in vitro*. Central reliance on integrated bioelectric, biochemical, and biomechanical signals to determine multicellular emergent trajectories make holistic understanding of these parallel regulatory systems paramount for future engineered control strategies. The objective of this research was to use computational models to investigate how molecular components of bioelectric and metabolic biological cell systems alter multicellular bioelectric patterning (**Chapter 3**) and cell metabolic flux dynamics (**Chapter 4**) in determining phenotypic trajectories. Moreover, we sought to extend system understanding to an effort to guide emergent morphogenic outcomes via external signaling. The central hypothesis guiding this work was that specific media compositions can alter molecular components of bioelectric and metabolic multicellular systems in a predictable manner, leading to desired morphologies, cell phenotypes, and novel functionalities. These improvements would make them better suited for use in cellular therapies and other multicellular engineered living biological systems applications.

To test this hypothesis, we developed two computational modeling frameworks of bioelectric signaling dynamic in multicellular networks and metabolic networks in cells and to simulated and compare against experimental observation. Bioelectric patterning modulation has previously been modeled in lower-level organisms (*Xenopus Laevis*) [60], but hiPSC-based tissue studies have not been conducted to this point. The bioelectric model

integrated hiPSC scRNA-sequencing transcriptomic data and electrophysiological characterization data into a multi-scale bioelectric simulation engine [148], and we simulated bioelectric patterning under various culture media formulations. We developed a supervised machine learning image analysis pipeline to quantitatively assess model simulation pattern prediction accuracy with respect to experimentally observed patterns under the various culture media conditions. We found that the model generated bioelectric patterns accurately reflected *in vitro* patterning outcomes under various culture conditions, and that the model can potentially predict novel pattern outcomes under novel media conditions. Furthermore, we utilized parameter optimization to determine required conditions for emergent pattern generation *in silico*. This represents the first step to model-guided design of engineered living system morphogenesis in this unexplored space. Future work will involve extending this model platform to downstream transcriptional regulation and consequential cell fate modulation with metabolic media supplements (i.e., L-glutamine and L-ascorbic acid).

Secondly, we developed a human genome-scale computational metabolic network model, constrained with bioinformatic and novel experimental fluxome data, to elucidate changes in metabolic landscape caused by specific media formulations. These combined novel model constraints represented a significant improvement to model application to a wider variety of contexts, as previous application to cancer cells elucidated differences in metabolic flux that resulted from phenotypic cell differences [125], but failed to elucidate flux differences in similar phenotypes that result from media composition changes. Importantly, both previous bioinformatic and novel media and fluxome constraints were required to replicate metabolic flux differences. We initially assessed simulation accuracy

in two case studies specific to hiPSC and hiPSC-CM metabolism. We extended this study to a novel media formulation that was hypothesized to increase mitochondrial maturation. Model simulations support changes to oxidative metabolism resulting from the novel culture media composition. Importantly, we experimentally observed significant improvements in mitochondrial respiration. This work helped to address the current gap in knowledge between culture media formulation design, consequent cellular metabolic adaption, and potential cell fate modulation.

## 5.2 Future directions: An integrated bioelectric and metabolic approach to improving hiPSC-CM differentiation

Morphogenesis does not consist of parallel biochemical, biomechanical, and bioelectric systems operating in isolation, rather cellular constituents behave more like dynamic information processing units that collectively modulate cell fate decisions in response to the previously mentioned signals. Therefore, it is insufficient to model these signals in isolation, and true holistic understanding of morphogenic process for exploitation in design of engineered living systems will depend on the development of hybrid mechanistic- and agent-based modeling tools that integrate previous efforts of biochemical, bioelectric, and biomechanical signals in multicellular system dynamics outcomes, such as a combined platform that incorporates the metabolic network of Chapter 4 into the multicellular bioelectric description of Chapter 3. The existing bioelectric model architecture is not inclusive of all interacting external and internal signals responsible for modulating $V_{mem}$ and long-field potential pattern formation. The model in Chapter 3 performs adequately when considering effects from other bioelectric system components but fails to incorporate post-translational and epigenetic modifications that originate from

other sources. For example, [67] found that retinoic acid modulated gap junction activity and expression during early mESC differentiation and predicted their effect on downstream cell fate decisions and morphogenic pattern with an agent-based model. Furthermore, improvements in model predictive accuracy would require consideration of the effects of precisely timed signaling cues or intrinsic system modification. Since FBA operates under steady state conditions, this would require an extension to a dynamic mathematical representation. Dynamic FBA, or DFBA, has been utilized in previous studies to help elucidate PSC metabolic trends with respect to cell cycle state [149], and possess the capacity to incorporate temporal dynamic changes to the system or culture media. The bioelectric model already possesses the capacity to incorporate precisely-times signaling cues, but future studies must consider the effects of these cues on emergent trajectories.

Calcium has been recognized as a modulatory gating ligand for potassium ion channel activation in excitable cells [150]. Following an action potential calcium-induced potassium channel opening quickens repolarization and inhibits firing. While these channels are mainly found in neural tissue, they are also present in various parts of the heart [151]. Specifically, [150] found that $Ca^{2+}$-activated potassium channels are differentially expressed during cardiac development. Interestingly, our scRNA sequencing novel cardiac progenitor sub-population classification revealed a large conductance calcium-activated potassium channel, $K_{Ca}1.1$ or KCNMA1, to be a potential novel phenotypic biomarker. Future directions for bioelectric models of cardiac progenitor cell bioelectric dynamics should incorporate these channels and their associated ligand-dependent dynamics because channel activation can be directly modulated by extracellular

[$Ca^{2+}$], thereby representing a potential media-based target for control of bioelectric dynamics.

Finally, progress in both modeling and experimental validation studies will require biotechnological advance in both validatory assays and reporter probes. The metabolic model is difficult to populate with complete metabolomics data, due to both data unavailability and lack of necessary tools. Metabolism is inherently difficult to experimentally probe [113]. It is known that metabolite levels and downstream signaling pathway modifications work in concert to coordinate cell fate decisions. Current experimental probes are unable to elucidate specificity of metabolites responsible for process, and these signaling process could possibly be activated by multiple metabolic mechanisms. For example, which chromatin modifications occur due to differences in which metabolite levels? Also, causality becomes more difficult to assess, as experimental metabolomics characterizations often only provide 'snapshots' of cell metabolic state at a particular time and fails to account for the influential actions of specific media components over time. It is critical to consider questions such as how much each culture media nutrient source contributes to cell metabolic pool for a desired phenotype.

In summary, our presented work provides strong evidence that multi-scale understanding of bioelectric and metabolic multicellular systems can be exploited to inform design strategies for multicellular engineered living systems. The research presented in this thesis aims to elucidate specific external and molecular drivers of morphogenic and metabolic processes for potential exploitation with computational modeling tools. To this end, we developed various novel culture media formulations, predicted bioelectric and metabolic signaling dynamics, and experimentally validated our hypothesized simulated

system dynamics. These results collectively validate the potential for model-guided media design of engineered living systems using understanding of bioelectric and metabolic systems properties.

# APPENDIX A. SUPPLEMENTAL INFORMATION FOR CHAPTER 3

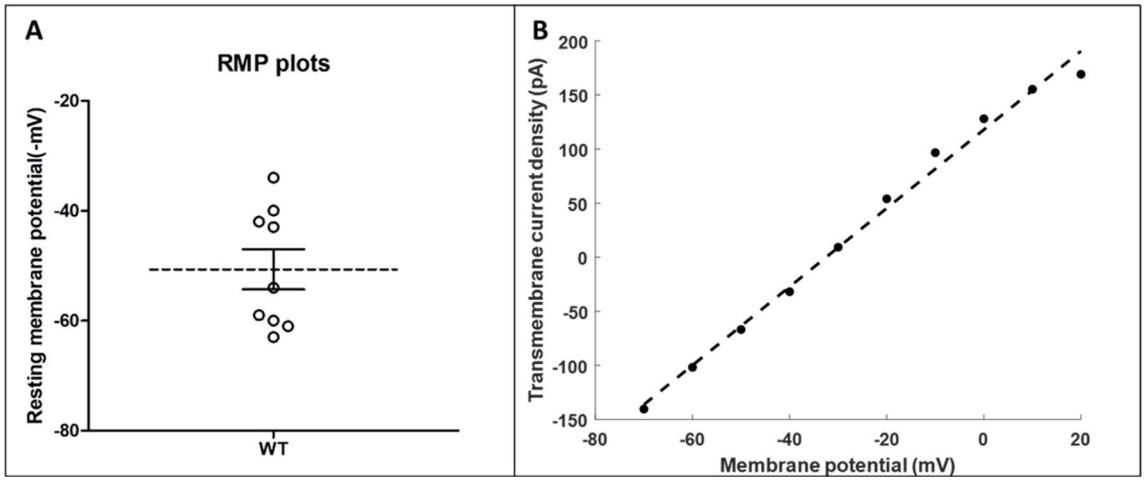


**Figure A 1. Whole-cell patch clamp data is shown for (A) individual samples (n=9) are patched at their respective resting membrane voltage potentials (Vmem); (B) transmembrane current density in response to increasing steady-state electrode holding potentials (mV); the dark line represents linear fit ($R^2$ = 0.9729) between the holding voltages and whole-cell transmembrane current density; the derived curve was used for downstream ionic flux parameterization**

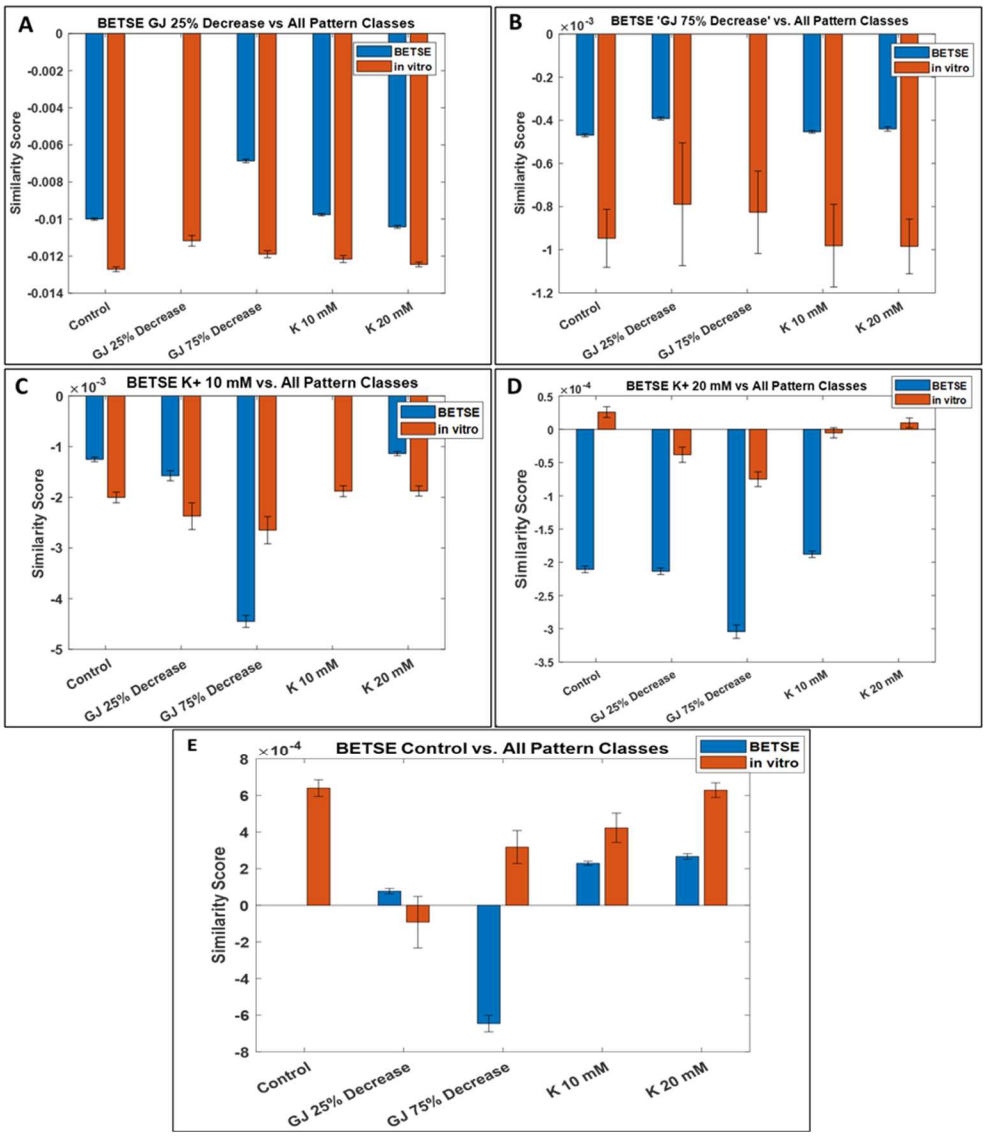


**Figure A 2. Similarity scores are shown for comparisons between BETSE culture condition target pattern classifiers. (A) Simulated 'GJ 25% decrease' classifier quantitative comparison to other BETSE and *in vitro* condition-specific image patterns. (B) Simulated 'GJ 75% decrease' classifier quantitative comparison to other BETSE and *in vitro* condition-specific image patterns. (C) Simulated 'K+ 10 mM supplement' classifier quantitative comparison to other BETSE and *in vitro* condition-specific image patterns. (D) Simulated 'K+ 20 mM supplement' classifier quantitative comparison to other BETSE and *in vitro* condition-specific image patterns. (E) Simulated 'Control' classifier quantitative comparison to other BETSE and *in vitro* condition-specific image patterns**

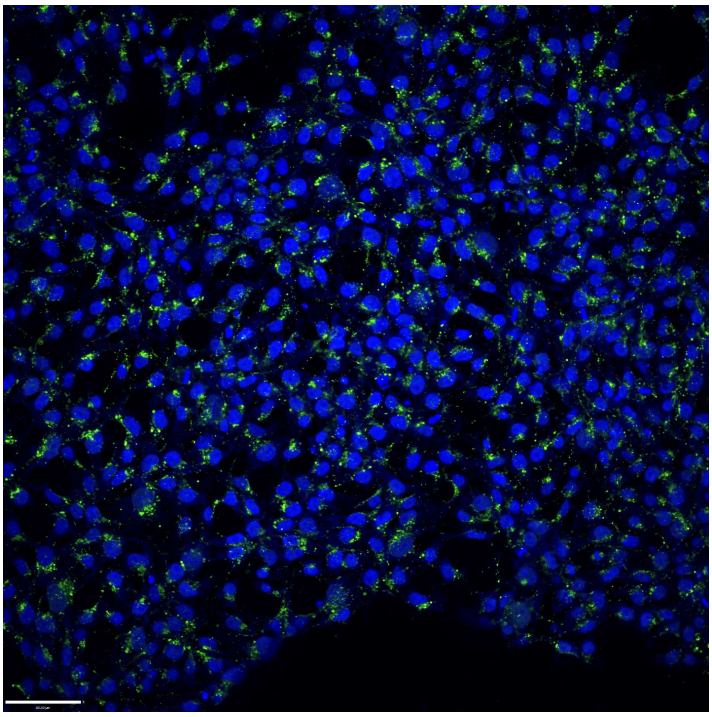

**Figure A 3. Expression of Connexin 43(Cx43) in WTC11 hiPSC clusters, as indicated by Cx43 immunocytochemical staining; The Cx43 is shown in green, and the nuclear Hoechst33342 stain is shown in blue**

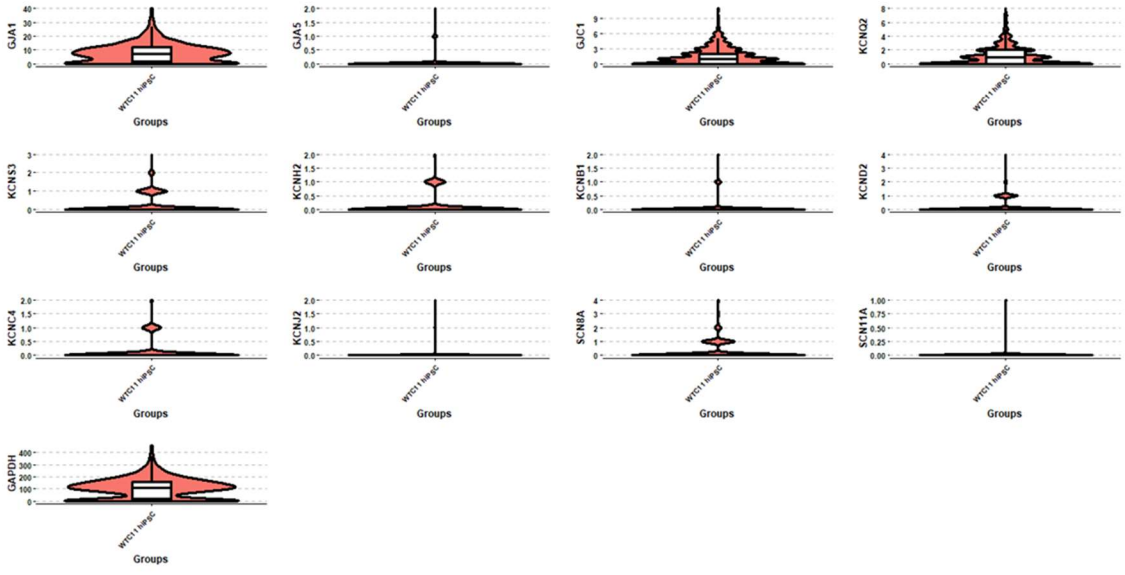


**Figure A 4. Single-cell RNA sequencing expression profiles for: Cx40 (GJA5), Cx43 (GJA1), and Cx45 (GJC1) connexin isoforms (1st row); voltage-gated $K^+$ ion channel isoforms Kv7.2 (KCNQ2), Kv9.3 (KCNS3), Kv11.1 (KCNH2), Kv2.1 (KCNB1), Kv4.2 (KCND2), Kv3.4 (KCNC4), and Kir2,1 (KCNJ2) (2nd row); voltage-gated $Na^+$ ion channel isoforms Nav1.6 (SCN8A), and Nav1.9 (SCN11A); Na+/K+-ATPase $\alpha$ (ATP1A1) and $\beta$ (ATP1B1) subunit isoforms (3rd row), and GAPDH in WTC11 hiPSCs.**

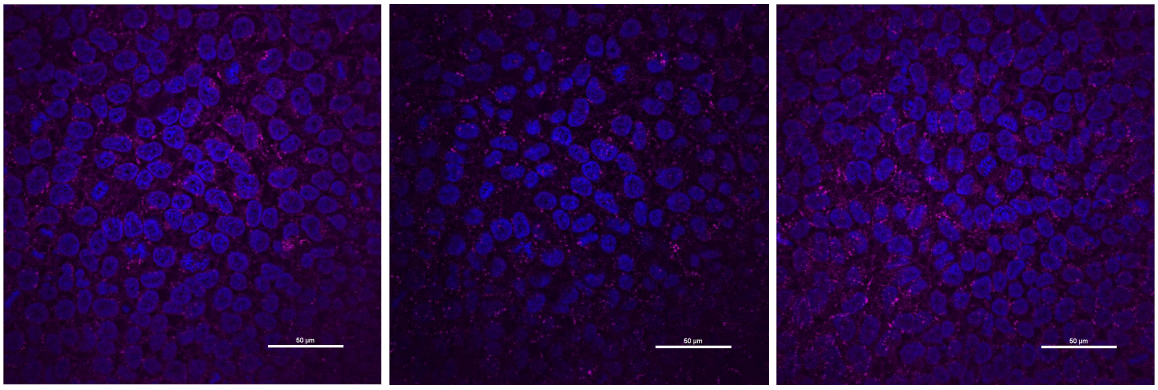

**Figure A 5. Expression of Connexin 43 in LBC2 hiPSC clusters, as indicated by Cx43 immunocytochemical staining; The Cx43 is shown in pink, and the nuclear Hoechst33342 stain is shown in blue.**

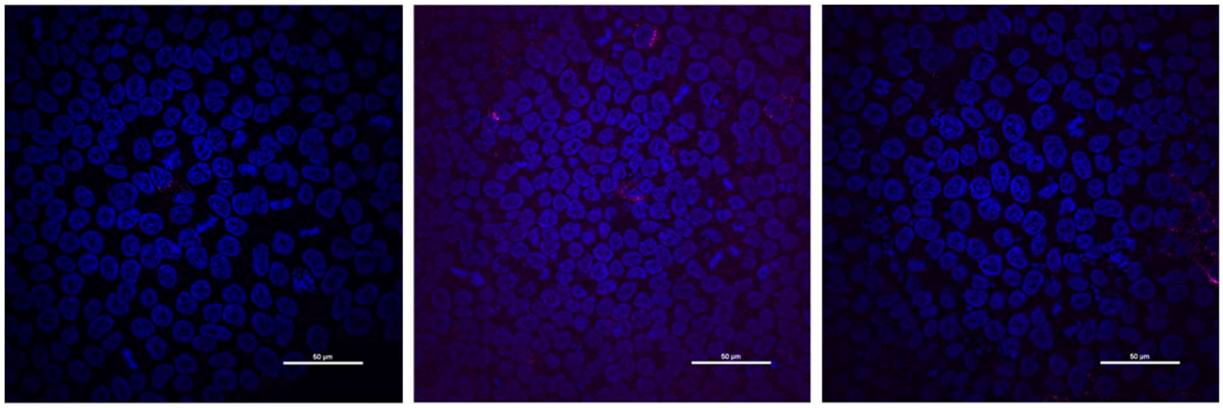

**Figure A 6. Expression of Connexin 43 in LBC2-GJA1 hiPSC clusters upon stable doxycycline-induced gene knockout, as indicated by Cx43 immunocytochemical staining; The Cx43 is shown in pink, and the nuclear Hoechst33342 stain is shown in blue.**

## A.1 QTS/TSSL Formulae/WEKA

We applied a previously developed spatial temporal logic algorithm [110] to quantitatively describe/define computational and experimentally obtained multicellular patterning. This is essentially the mechanism by which the respective patterns are quantitatively described/defined by. The quantitative valuation of an input image defines how each node (corresponding to a unique pattern) presents itself with respect to the remaining 'image space' (corresponding to the global cell cluster).

### *A.1.1 Quad-tree*

An input n x n greyscale photo is read into Matlab as a ***matrix*** $A_{kxk}$ where each element $a_{ij} = < a_{ij}^{(Gr)} >$ is the normalized RGB pixel value for a specific $< i, j >$ coordinate.

$$0 \leq a_{ij}^{(Gr)} \leq 1 \tag{A.1}$$

Given an ***input image's network A***, the submatrix ***A[$i_s$, $i_e$, $j_s$, $j_e$]*** corresponds to the rows and columns that are ½ the original length to create four quadrants from the original network. Following this syntax, we represented matrix A as a quad-tree. A ***quad-tree*** $Q = (V, R)$ is a quaternary tree representation of matrix A where each ***vertex*** $v \in V$ represents a quad-tree submatrix and the ***relation*** $R \subset V\ x\ V$ defines four children for each specified vertex. Additionally, each edge of the tree is labeled with the direction of the submatrix created represented as the child, using directions north west (NW), north east (NE), south east (SE), and south west (SW). The ***representation function*** $\mu^{(c)}(v): V \rightarrow [0, b]\ x\ [0, b]$ is defined for each matrix and submatrix. It provides the mean value and variance for the concentration of RGB colors in a particular region of the space represented by the vertex, v.

$$\mu^{(c)}(v) = \left(\mu_1^{(c)}, \mu_2^{(c)}\right) \tag{A.2}$$

$$\mu_1^{(c)} = \frac{1}{(i_e - i_s + 1)(j_e - j_s + 1)} \sum_{i,j \in \{i_s,\ldots,i_e\}\ x\ \{j_s,\ldots,j_e\}} a_{ij}^{(c)} \tag{A.3}$$

$$\mu_2^{(c)} = \frac{1}{(i_e - i_s + 1)(j_e - j_s + 1)} \sum_{i,j \in \{i_s,\ldots,i_e\}\ x\ \{j_s,\ldots,j_e\}} (a_{ij}^{(c)} - \mu_1^{(c)})^2 \tag{A.4}$$

The mean and variance metrics $\mu_1^{(c)}$and $\mu_2^{(c)}$provide information on a color species (R,G,B) concentration within a particular image frame and variance across the current level of resolution.

*A.1.2 QTS/TSSL formulae*

The Quad Transition Systems (QTSs) of input network quad-trees combines the set of directions with the previously defined metrics to create a more compact quad-tree representation [90]. This syntax provides a more compact representation of the original quad-tree for image comparison quantification and TSSL formula extraction. The QTS building algorithm starts from an input quad-tree $Q = (V, R)$ of a matrix $A_{kxk}$ and a unique labeling function $LQ: R \rightarrow D$. The algorithm is constructed such that it provides a compact labeling function tuple that characterizes the hierarchical connectivity amongst quad-tree nodes. The initialization phase defines structures for quad-tree states, directions, variables, and state transitions with subsequent equivalent leaf set partition. A self-transition is defined for each state (or node) in the partitioned set and non-leaf child nodes were also assigned a node transition. The parent to child transition is denoted a1(t), etc. to denote the directional transitions. Then, all non-leaf nodes are explored in a breadth-first search and new state tuples are added to the QTS structure. The same equivalent quad-tree node aggregation procedure defined earlier is repeated for the non-leaf nodes. The final QTS is a more compact representation of the original quad-tree. The TSSL syntax is as follows:

$$\varphi ::= \top \mid \bot \mid m \sim d \mid \neg\varphi \mid \varphi_1 \wedge \varphi_2 \mid \exists_B \circ \varphi \mid \forall_B \circ \varphi \mid \exists_B \varphi_1 U_k \varphi_2 \mid \exists_B \varphi_1 U_k \varphi_2 \quad \text{(A.5)}$$

with $\sim \in \{\leq, \geq\}, d \in [0, b], b \in R_+, k \epsilon N_{>0}, B \subseteq D : B \neq \emptyset$, and $m \in \Sigma$, with being the set of variables. From this specified syntax, two additional spatial mathematical operators can be defined: the *exist eventually* operator $\exists_B F_k$, the *for all eventually* operator $\forall_B F_k$, the *exists globally* operator $\exists_B G_k$, and the *for all globally* operator $\forall_B G_k$. This defined syntax can also be represented as shown below:

$$\exists_B F_k \varphi := \exists_B \top U_k \varphi \quad \exists_B G_k \varphi := \neg \forall_B F_k \neg \varphi. \tag{A.6}$$

$$\forall_B F_k \varphi := \forall_B \top U_k \varphi \quad \forall_B G_k \varphi := \neg \exists_B F_k \neg \varphi. \tag{A.7}$$

pl; TSSL shares semblance to CTL logic, the main difference being the interpretation of the mathematical operators [111]. The next and until operators do not operate over time per say, but spatially where they specify a *change in resolution.*

Qualitative & Quantitative Semantics: Let $Q = (S, s_l, \tau, \Sigma, [.], L)$ be a QTS, then satisfies a TSSL formula , written $Q \vDash \varphi$, if and only if $Q, s_l \vDash \varphi$ , where the equations used to characterize the TSSL formulae are shown below:

$$Q, s \vDash \top \tag{A.8}$$

$$Q, s \vDash m \sim d \tag{A.9}$$

$$Q, s \vDash \neg \varphi \tag{A.10}$$

$$Q, s \vDash \varphi_1 \wedge \varphi_2 \tag{A.11}$$

$$Q, s \models \exists_B \circ \varphi \tag{A.12}$$

$$Q, s \models \forall_B \circ \varphi \tag{A.13}$$

$$Q, s \models \exists_B \varphi_1 U_k \varphi_2 \tag{A.14}$$

$$Q, s \models \forall_B \varphi_1 U_k \varphi_2 \tag{A.15}$$

The qualitative semantics defined are utilized to check if an input spatial model does or does not violate a TSSL pattern formula. However, it does not possess the ability to determine how much a desired TSSL formula is satisfied or not. Quantitative semantics are incorporated to determine a numerical value that represents the amount of closeness or separation between two input QTSs. This value is referred to as the measure of satisfaction of a TSSL formula over an input TSSL formula. Given a QTS $Q_{TS} = (S, s_l, \tau, \Sigma, [.], L)$ the measure of a TSSL formula quantitative valuation $[\![\varphi]\!] : S \rightarrow [-b, b]$ is shown below:

$$[\![\top]\!](s) = b \tag{A.16}$$

$$[\![\bot]\!](s) = -b \tag{A.17}$$

$$[\![m \sim d]\!](s) = (\sim is \geq) \, ? \, ([s](m) - d) : (d - [s](m)) \tag{A.18}$$

$$[\![\neg\varphi]\!](s) = -[\![\varphi]\!](s) \tag{A.19}$$

$$[\![\varphi_1 \wedge \varphi_2]\!](s) = min\,([\![\varphi_1]\!](s), [\![\varphi_2]\!](s)) \tag{A.20}$$

$$[\![\exists_B \circ \varphi]\!](s) = \frac{1}{4}[\![\varphi]\!](\pi_1^B) \tag{A.21}$$

$$[\![\forall_B \circ \varphi]\!](s) = \frac{1}{4}[\![\varphi]\!](\pi_1^B) \tag{A.22}$$

$$[\![\exists_B \varphi_1 U_k \varphi_2]\!](s) = \ sup_{\pi^B \in LPaths^B(s)}\{min \frac{1}{4^i}[\![\varphi_2]\!](\pi_i^B) \tag{A.23}$$

$$inf\ \{\frac{1}{4^j}\ [\![\varphi_1]\!]\left(\pi_j^B\right) \mid j < i\}) \mid 0 < i\ \leq\ k\}\} \tag{A.24}$$

$$[\![\forall_B \varphi_1 U_k \varphi_2]\!](s) = \ inf_{\pi^B \in LPaths^B(s)}\{min \frac{1}{4^i}[\![\varphi_2]\!](\pi_i^B) \tag{A.25}$$

$$inf\ \{\frac{1}{4^j}\ [\![\varphi_1]\!]\left(\pi_j^B\right) \mid j < i\}) \mid 0 < i\ \leq\ k\}\} \tag{A.26}$$

The output provides a measure of the level of satisfaction of a desired TSSL formula over an input QTS. This output is constructed via combinations of distance (absolute and max), and correctness measures to link the quantitative and qualitative valuations of a QTS. The correctness value determines the level of similarity between two patterns of interest.

*i. max distance* - measures amount of greatest absolute distance between two quantitative valuations for some partition of space. The details of the metric calculation are described in further detail in [90].

*ii. correctness* – This value gives meaning to the level of TSSL formula satisfaction for a given input network. Formally, it states that, "a QTS satisfies target TSSL formula and max distance is less than the quantitative valuation of the TSSL formula over the first QTS

satisfying $\varphi$" [90]. This provides a means to merge formulas created from *in silico* and *in vitro* bioelectric pattern classes.

These additional metrics ultimately help in determining the ability of the computational platform to accurately predict iPSC bioelectric patterns. Ultimately, the QTSs are used to generate labeled data sets:

The dataset is then separated into training and testing sets $\mathcal{L}_y$ and $\mathcal{L}_T$. Image datasets containing desired patterns are denoted (+) and the others (-) for purposes of training a rule-based machine learning algorithm (RIPPER) to learn a set of rules (***classifier***) for the desired pattern set (+). These classifiers are then transformed to TSSL formulae characterizing +. The syntax used to define the rules follows:

Each classifier consists of a set of rules. $C_i$ describes a Boolean formula defining a certain variable's linear predicates at a QTS state (e.g. [s](m) > d, or $\mu_1^{(c)} > 0.75$) and $\sim_i$ describes the values in the + and – label sets. The linear predicates for any QTS state can be described with a QTS paths are translated further into unique classification formulas, utilizing the addition of next and existential and next *mathematical* spatial operators along the QTS paths. The resulting classifiers are read as if-else statements and the formal pattern description arises from this TSSL formula by utilizing QTS paths starting from the root state ($s_i$) to the state of interest. A typical TSSL formula is defined by the following syntax:

$$\Phi_+ := \bigvee_{j \in R_+} (\Phi_j \wedge \bigwedge_{i=1,\ldots,j-1} \neg \Phi\ ) \tag{A.27}$$

where $R_+$ is the set of indices of rules ($r_i$), with $\sim_i$ = +, and ($\Phi_i$) is the TSSL formula created from $C_i$.

### A.2 Quantitative Image Similarity Scoring

A TSSL formula ($\varphi$) provides quantitative information concerning the satisfaction of a desired target pattern, where an input image's quad-tree ($Q = (V, R)$) vertex ($v \in V$). The value assigned to each input quad tree was defined as $\rho(\varphi, v)$. For each recursion the input image's quantitative valuation was defined below:

$$\rho\left(\mu_i^{(c)} \geq d, v\right) = \mu_i^{(c)}(v) - d \tag{A.28}$$

$$\rho\left(\mu_i^{(c)} \leq d, v\right) = d - \mu_i^{(c)}(v) \tag{A.29}$$

$$\rho(\neg\varphi, v) = -\rho(\varphi, v) \tag{A.30}$$

$$\rho(\varphi_1 \wedge \varphi_2, v) = \left(\rho(\varphi_1, v), \rho(\varphi_1, v)\right) \tag{A.31}$$

$$\rho(\varphi_1 \vee \varphi_2, v) = \left(\rho(\varphi_1, v), \rho(\varphi_1, v)\right) \tag{A.32}$$

$$\rho(\exists_B \circ \varphi, v) = 0.25 max_{b \in B} \rho(\varphi, v_b) \tag{A.33}$$

$$\rho(\forall_B \circ \varphi, v) = 0.25 min_{b \in B} \rho(\varphi, v_b) \tag{A.34}$$

where $v_b$ was the child vertex of $v$ having label b

Proof of semantic validity can be found in [90; 110]. An image pattern classifier ( $\varphi(Q \vDash \varphi)$ ) satisfaction is declared if $\rho(\varphi, v_0) > 0$, where $v_0$ denotes the root of the previously defined quad-tree $Q$, and is declared violated if $\rho(\varphi, v_0) > 0$. This process is referred to

quantitative valuation, and its magnitude is utilized in the determination of degree of target pattern satisfaction or dis-satisfaction by quad-tree $Q$. The quantitative valuation is referred to as the quad-tree similarity score.

### A.3 Particle Swarm Optimization

The BETSE simulation input parameters $D_{mem,K+}$, $D_{mem,Na+}$, $D_{mem,Cl-}$, and $\beta_{GJ}^{o}$, play critical roles in determining global and local features of resulting output pattern images. If the parameter set is defined as $p \in \Omega \subset R^{N_p}$, where $\Omega$ represents a possible parameter range or set of parameter ranges and $N_p$ represents the total number of adjusted parameters. Images from condition-specific BETSE image sets (numbered 1,…,T) were processed through the TSSL algorithm and produced corresponding individual quadtrees and roots, $Q[t]$ and $v_0[t]$, respectively, for each image within the set. The target pattern specification against which simulated images are compared is denoted. as $\Phi_{Pattern}$; the quantified relationship for a set of simulated images resulting from parameterization values $p$ is defined with the following equation:

$$S(p) = max_{0 \le t \le T} \rho(\Phi_{Pattern}, v_0[t]) \tag{A.35}$$

The similarity score was denoted by $\rho$ and $S(p)$ was denoted as a random variable. This score was used to track simulation images possessing positive valuations, which indicated pattern presence. The problem then becomes maximizing the score $S(p)$ for a parameterization $p^*$. In summary, this algorithm searches for the parameters that, when averaged together, produced the maximum similarity score to the target pattern classifier. To accomplish this, the algorithm utilized average scores from *n* simulations to account for

noise in similarity scoring and simulation stochastic initialization. This means that the parameter(s), $p^*$, that induces the highest similarity score is essentially what is sought after. For $n$ simulations, the following mean similarity score expression was utilized:

$$E\big(S(p)\big) \approx \tilde{S}(p) = \left(\frac{1}{n}\right) * \sum_{i=1}^{n} S_i(p) \tag{A.36}$$

where $S_i(p)$ represents the similarity score for parameter set $p$ of the $i^{th}$ simulation. Similar to [68], we ran 3 simulations for each potential parameter set (n=3). Particle swarm optimization was chosen as the algorithm of choice to address the unknown structure of the solution space. It is a heuristic technique that is especially well-suited to explore irregular search spaces to find local maxima or minima. Here is how the algorithm operates: it initially places a set of $M$ particles at random points in parameter space, where each particle's position and velocity were denoted by $z_i \in \Omega$ and $z_i'$, respectively; the particle's position represented a value within the allowable parameter bounds and the particle's velocity represented a search direction from the currently-implemented solution; the particle's position and velocity were then updated in accordance with the following expressions after each simulated iteration.

$$z_i' \leftarrow W z_i + \eta\big(r_p\big)(z_i^* - z_i) + \eta(r_g)(z^* - z_i) \tag{A.37}$$

$$z_i \leftarrow z_i + z_i' \tag{A.38}$$

where $\eta(r_i)$ is a random number selected from distribution [0, $r_i$], and the parameters $W \in R, r_p, r_g$ are tuned by the user. This process is iterated until a user-defined search criterion

is satisfied. In the case that BETSE simulations produced positive similarity scores or negative similarity scores near zero for $\tilde{S}(p^*)$, the associated parameter set was called the optimized parameters.

### A.4 Simulated Bioelectric Pattern Classifiers

[1] 'Control' pattern class had 97.40% classification accuracy (n = 200);

$$\phi_{Control} = \forall_{\{Root\}} \circ [0.7726 \leq m \leq 0.7196] \wedge \forall_{\{NW,NE,SE,SE,SE\}} \circ [m \geq .705882] \wedge \forall_{\{NW,NE,NE\}} \circ [m \geq .7033] \wedge \forall_{\{NW,SW,NW,SW,SW\}} \circ [m \leq .8237] \wedge \forall_{\{NW,SW,NW,SW,SE\}} \circ [m \geq .7569] \wedge \forall_{\{NW,SE,NW\}} \circ [m \leq .9115] \wedge \forall_{\{NW,SE,NE,SE\}} \circ [m \geq .6542] \wedge \forall_{\{NW,SE,NE,SE,SE\}} \circ [m \leq .9176] \wedge \forall_{\{NW,NW,SW,NW,SW\}} \circ [m \leq .7794] \wedge \forall_{\{NW,SE,SW,NE,SW\}} \circ [m \leq .9118] \wedge \forall_{\{NW,SW,SW,NW,SW\}} \circ [m \leq .9111] \wedge \forall_{\{NW,SE,NE,NW\}} \circ [m \leq .9297] \wedge \forall_{\{NW,SE,SE\}} \circ [m \geq .6955] \wedge \forall_{\{NW,SE,SE,NE,SW\}} \circ [m \leq .9229] \wedge \forall_{\{NW,NE,NE,NE,NW\}} \circ [m \geq .5071] \wedge \forall_{\{NW,NE,NW,NE,SE\}} \circ [m \leq .9292]$$

[2] 'GJ75% magnitude decrease' pattern class had 94.73% classification accuracy (n = 200);

$$\phi_{GJ,75\%\ Decrease} = \forall_{\{Root\}} \circ [0.7238 \geq m] \wedge \forall_{\{NW,NW,NW,SE,SE\}} \circ [m \geq .9020] \wedge \forall_{\{NW,NW,NW,NE,NE\}} \circ [m \leq .7559] \wedge \forall_{\{NW,NE,SW,SW,SW\}} \circ [m \leq .6275] \wedge \forall_{\{NW,NE,NW,SW,SW\}} \circ [m \geq .9059] \wedge \forall_{\{NW,NW,NE,SE,SE\}} \circ [m \leq .6275] \wedge \forall_{\{NW,NE,SW,SW,NE\}} \circ [m \geq .8825] \wedge \forall_{\{NW,SE,NE\}} \circ [m \leq .8671] \wedge \forall_{\{NW,SE,NW,SW,NE\}} \circ [m \leq .6256] \wedge \forall_{\{NW,SE,NW,NW,NE\}} \circ [m \geq .8814] \wedge \forall_{\{NW,NE,SW,SW,NE\}} \circ [m \geq .6431] \wedge \forall_{\{NW,SE,NW,SE,SE\}} \circ [m \geq .8902] \wedge \forall_{\{NW,NE,SE,NW\}} \circ [m \geq .7015] \wedge \forall_{\{NW,SE,NE,NE,NE\}} \circ [m \leq .5498] \wedge \forall_{\{NW,NE,SE,NE,SE\}} \circ [m \leq .4814] \wedge \forall_{\{NW,NW,SW,NE,NE\}} \circ [m \leq .4588] \wedge \forall_{\{NW,NE,SE,SE,SE\}} \circ [m \geq .9451] \wedge \forall_{\{NW,SE,NW,NW,NE\}} \circ [m \leq .5765] \wedge \forall_{\{NW,SE,NW,SW,SW\}} \circ [m \geq .8912] \wedge \forall_{\{NW,SE,NE,NE,NW\}} \circ [m \leq .5609] \wedge \forall_{\{NW,NE,SE,NE,NE\}} \circ [m \geq .8720] \wedge \forall_{\{NW,NE,NE,NE,SW\}} \circ [m \leq .5706] \wedge \forall_{\{NW,NE,SW,NW,NE\}} \circ [m \geq .9490]$$

[3] 'GJ25% magnitude decrease' pattern class had 94.73% classification accuracy (n = 200);

$$\phi_{GJ,25\%\,Decrease} = \forall_{\{NW,SE,NE,SE\}} \circ [m \leq 0.1255] \wedge \forall_{\{NW,NW,SW,SW,SE\}} \circ [m \geq .3304] \wedge \forall_{\{NW,NE,NE,SE,NW\}} \circ [m \leq .2510] \wedge \forall_{\{NW,SE,NE,SE\}} \circ [m \leq .1240] \wedge \forall_{\{NW,NW,NE,NE\}} \circ [m \geq .1794] \wedge \forall_{\{NW,SW,NW,SW,NE\}} \circ [m \geq .3402] \wedge \forall_{\{NW,SW,SW,SW\}} \circ [m \leq .1387] \wedge \forall_{\{NW,NE,SE\}} \circ [m \leq .6460]$$

[4] 'K+ 10 mM supplement' pattern class (n = 200);

$$\phi_{K^+\,10\,mM} = \forall_{\{Root\}} \circ [m \geq 0.4552] \wedge \forall_{\{NW,NW,NW,NE\}} \circ [m \leq 0.1637] \wedge \forall_{\{NW,SW,NW,NW,SE\}} \circ [m \leq 0.2510] \wedge \forall_{\{Root\}} \circ [m \geq 0.6986] \wedge \forall_{\{NW,SE,SE,NE\}} \circ [m \leq 0.7272] \wedge \forall_{\{NW,SE,SE,SW,NE\}} \circ [m \geq 0.8882] \wedge \forall_{\{NW,NW,SW,SE,NW\}} \circ [m \geq 0.7765] \wedge \forall_{\{Root\}} \circ [m \geq 0.7152] \wedge \forall_{\{NW,NW,NW,NW,NE\}} \circ [m \leq 0.4755] \wedge \forall_{\{NW,NE,SE,NE,NE\}} \circ [m \leq 0.6961] \wedge \forall_{\{NW,NE,NW,SW,SW\}} \circ [m \geq 0.8108]$$

[5] 'K+ 20 mM supplement' pattern class (n = 200);

$$\phi_{K^+\,20\,mM} = \forall_{\{NW,NW,SE,SE,SW\}} \circ [m \geq 0.9235] \wedge \forall_{\{NW,NW,SE,SE,NW\}} \circ [m \leq 0.8971] \wedge \forall_{\{NW,NW,SE,NE,SW\}} \circ [m \geq 0.6255] \wedge \forall_{\{NW,SE,NW,NW,SE\}} \circ [m \geq 0.9225] \wedge \forall_{\{NW,SE,NW,NW,NE\}} \circ [m \leq 0.9049] \wedge \forall_{\{NW,NW,NW,NE\}} \circ [m \geq 0.1728] \wedge \forall_{\{NW,SE,NE,NW,SW\}} \circ [m \geq 0.9569] \wedge \forall_{\{NW,NW,NE,NE,SE\}} \circ [m \geq 0.5863] \wedge \forall_{\{NW,NE,SW,SE\}} \circ [m \leq 0.9206] \wedge \forall_{\{NW,SW,SW,SW,NE\}} \circ [.0745 \leq m \leq 0.0824] \wedge \forall_{\{NW,SW,SE,SW\}} \circ [m \leq 0.1252] \wedge \forall_{\{NW,NW,SE,SW,NE\}} \circ [m \geq 0.9431] \wedge \forall_{\{NW,SE,NW,SE,NE\}} \circ [m \geq 0.9029] \wedge \forall_{\{NW,SE,NW,NE,SE\}} \circ [m \leq 0.9225] \wedge \forall_{\{NW,SW,SW,NW,NE\}} \circ [m \geq 0.9912]$$

# APPENDIX B. SUPPLEMENTAL INFORMATION FOR CHAPTER 4

## B.1 Mitotracker Assay Outcomes

We observed that the initial exit from pluripotency upon differentiation is accompanied by specific metabolic profiles, and these profiles are specific to each extra-embryonic lineage (i.e., endoderm, mesoderm, ectoderm) [Mostafavi et al., 2021 - 144; Lu et al., 2019]. Therefore, we sought to assess media-induced oxidative metabolic transitions that occur at the start of differentiation. We incubated our cells with a fluorescent probe for mitochondrial $V_{mem}$, MitoTracker Red CMXRos, to track media-based changes in mitochondrial function. Mitotracker Red CMXRos is a fluorescent reporter that stains and accumulates in mitochondrial membranes in accordance with mitochondrial $V_{mem}$ state. Specifically, fluorescence intensity increases upon increase in mitochondrial $V_{mem}$. Because L-glutamine is supposed to enhance TCA cycle activity and oxidative phosphorylation, we hypothesized that L-glutamine supplementation in cell culture would increase mitochondrial function during hiPSC-cardiomyocyte differentiation. Furthermore, we hypothesized that the L-ascorbic acid supplement would provide a therapeutic benefit in antioxidant capacity that further promotes oxidative activity. To this end we cultured cells in control RPMI1640 media, RPMI1640 supplemented with L-glutamine, and RPMI1640 media supplemented with L-glutamine and L-ascorbic acid. These media conditions were used as the directed hiPSC-CM differentiation [36]

progressed from day 0 to day 1.5 (36 hours). Cells were then incubated in MitoTracker Red CMXRos and imaged for 12 hours. Unexpectedly, we observed an initial signal dominance in fluorescence for the control media conditions with respect to the L-glutamine and 'DreCustom' (L-glutamine+ascorbic acid) media conditions, as shown in **Figure B-1**. This behavior is supported by trends observed in [Mostafavi et al., 2021], as they found mitochondrial content decreases as hPSCs exit pluripotency and differentiate towards the mesoderm lineage. However, this observed trend turned out to be partially transient, as signal strength changes around 4 hours to support the hypothesized effect of L-glutamine on mitochondrial metabolic activity.

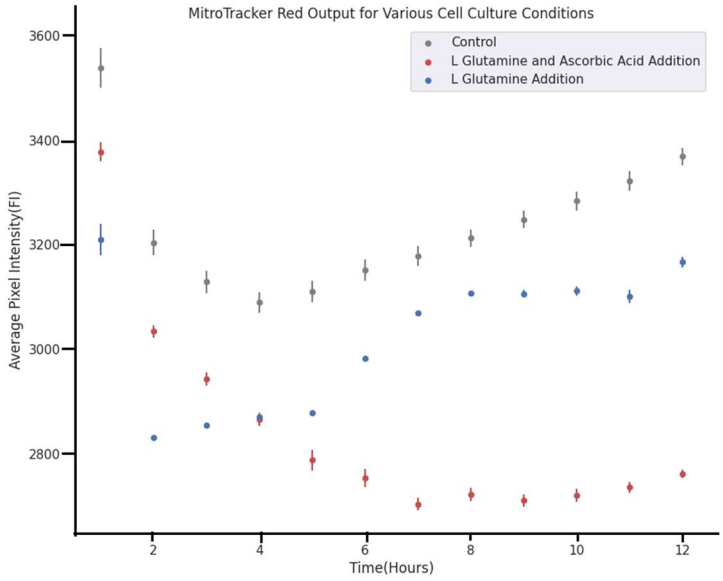


**Figure B 1. Figure showing MitoTracker fluorescence intensities compared between cell culture media conditions. The various culture media compositions are shown in the legend. The average pixel intensity shown increases in direct proportion to mitochondrial $V_{mem}$. Error bars:SEM**

By the end of the characterization the control media condition reflects the highest mitochondrial $V_{mem}$, followed by the L-glutamine-supplemented and ascorbic acid + L-glutamine-supplemented culture conditions. While this result was unexpected, co-staining with an immobile mitochondrial fluorescent probe would enable us to ensure that this effect

truly reflects changes in mitochondrial $V_{mem}$ and not variable cellular mitochondrial abundance.

## B.2. Culture Media Formulations

**Table B 1. mTeSR Culture Media composition**

| Metabolite | Concentration (mM) |
|---|---|
| L-cystine | 7.83E-08 |
| Vitamin B12 | 3.94E-10 |
| L-arginine | 5.48E-07 |
| L-asparagine | 1.37E-08 |
| L-aspartate | 1.37E-08 |
| Biotin | 1.12E-11 |
| Calcium | 8.24E-07 |
| Cholesterol | 5.03E-08 |
| Chloride | 1.01E-04 |
| Folate | 4.71E-09 |
| D-Glucose | 1.37E-05 |
| L-Glutamine | 2.94E-06 |
| L-Glutamate | 1.37E-07 |
| Glycine | 2.94E-07 |
| Reduced Glutathione | 6.38E-09 |
| Bicarbonate | 1.80E-05 |
| L-histidine | 1.18E-07 |
| L-isoleucine | 3.26E-07 |
| Inositol | 5.49E-08 |
| Potassium | 3.26E-06 |
| L-leucine | 3.54E-07 |
| L-lysine | 3.91E-07 |
| L-methionine | 9.06E-08 |
| Sodium | 1.14E-04 |
| Nicotinamide | 1.30E-08 |
| L-phenylalanine | 1.69E-07 |
| Phosphate | 1.00E-07 |
| Pantothenic acid | 3.69E-09 |
| L-proline | 2.16E-07 |
| Pyridoxine | 7.62E-09 |
| Riboflavin | 4.56E-10 |
| L-serine | 2.94E-07 |
| Sulfate | 3.20E-07 |
| Thymine | 2.42E-08 |
| L-Threonine | 3.52E-07 |
| L-Tryptophan | 3.46E-08 |
| L-Tyrosine | 1.68E-07 |
| L-Valine | 3.55E-07 |
| Pyridoxine | 7.62E-09 |
| Riboflavin | 4.56E-10 |
| L-serine | 2.94E-07 |
| Sulfate | 3.20E-07 |
| Thymine | 2.42E-08 |
| L-Threonine | 3.52E-07 |

| | |
|---|---|
| L-Tryptophan | 3.46E-08 |
| L-Tyrosine | 1.68E-07 |
| L-Valine | 3.55E-07 |
| L-Threonine | 3.52E-07 |

**Table B 2. RPMI 1640 media formulation**

| **Metabolite** | **Concentration (mM)** |
|---|---|
| 4-Hydroxyproline | 1.53E-07 |
| L-cystine | 2.08E-07 |
| Vitamin B12 | 3.69E-12 |
| L-arginine | 1.15E-06 |
| L-asparagine | 3.78E-07 |
| L-aspartate | 1.50E-07 |
| Biotin | 8.19E-10 |
| Calcium | 4.24E-07 |
| Cholesterol | 2.15E-08 |
| Chloride | 1.09E-04 |
| Folate | 2.27E-09 |
| D-Glucose | 1.11E-05 |
| L-Glutamine | 2.05E-06 |
| L-Glutamate | 1.36E-07 |
| Glycine | 1.33E-07 |
| Reduced Glutathione | 3.25E-09 |
| Bicarbonate | 2.38E-05 |
| L-histidine | 9.67E-08 |
| L-isoleucine | 3.81E-07 |
| Inositol | 1.94E-07 |
| Potassium | 5.37E-06 |
| L-leucine | 3.81E-07 |
| L-lysine | 2.19E-07 |
| L-methionine | 1.01E-07 |
| Sodium | 1.38E-04 |
| Nicotinamide | 8.19E-09 |
| L-phenylalanine | 9.08E-08 |
| Phosphate | 5.64E-06 |
| Pantothenic acid | 1.05E-09 |
| L-proline | 1.74E-07 |
| Pyridoxine | 4.86E-09 |
| Riboflavin | 5.31E-10 |
| L-serine | 2.85E-07 |
| Sulfate | 4.06E-07 |
| Thymine | 2.97E-09 |
| L-Threonine | 1.68E-07 |
| L-Tryptophan | 2.45E-08 |
| L-Tyrosine | 1.11E-07 |
| L-Valine | 1.71E-07 |

**Table B 3. DMEM media formulation**

| Metabolite | Concentration (mM) |
|---|---|
| L-cystine | 2.01E-07 |
| Folate | 9.07E-09 |
| D-Glucose | 2.50E-05 |
| L-Glutamine | 4.00E-03 |
| Glycine | 4.00E-07 |
| L-histidine | 2.00E-06 |
| L-isoleucine | 8.02E-07 |
| L-leucine | 8.02E-07 |
| L-lysine | 7.98E-07 |
| L-methionine | 2.01E-07 |
| L-phenylalanine | 4.00E-06 |
| Pyridoxine | 1.94E-08 |
| Riboflavin | 1.06E-09 |
| L-serine | 4.00E-06 |
| Thymine | 1.19E-08 |
| L-Threonine | 7.98E-07 |
| L-Tryptophan | 7.84E-08 |
| L-Tyrosine | 3.98E-07 |
| L-Valine | 8.03E-07 |
| L-arginine | 3.99E-07 |
| Calcium | 1.80E-06 |
| Cholesterol | 2.86E-08 |

# REFERENCES


[1] Ramalho-Santos, M., and Willenbring, H. (2007). On the Origin of the Term "Stem Cell". Cell Stem Cell *1*, 35-38.

[2] Maximow, A. (1909). Der Lymphozyt als gemeinsame Stammzelle der verschiedenen Blutelemente in der embryonalen Entwicklung und im postfetalen Leben der Säugetiere. Folia Haematol *8*, 125-141.

[3] Bujko, K., Kucia, M., Ratajczak, J., and Ratajczak, M.Z. (2019). Hematopoietic Stem and Progenitor Cells (HSPCs). Adv Exp Med Biol *1201*, 49-77.

[4] Evans, M.J., and Kaufman, M.H. (1981). Establishment in culture of pluripotential cells from mouse embryos. Nature *292*, 154-156.

[5] Thomson, J.A., Itskovitz-Eldor, J., Shapiro, S.S., Waknitz, M.A., Swiergiel, J.J., Marshall, V.S., and Jones, J.M. (1998). Embryonic Stem Cell Lines Derived from Human Blastocysts. Science *282*, 1145-1147.

[6] Lo, B., and Parham, L. (2009). Ethical issues in stem cell research. Endocr Rev *30*, 204-213.

[7] Matthews, K.R., and Moralí, D. (2020). National human embryo and embryoid research policies: a survey of 22 top research-intensive countries. Regen Med *15*, 1905-1917.

[8] Takahashi, K., and Yamanaka, S. (2006). Induction of pluripotent stem cells from mouse embryonic and adult fibroblast cultures by defined factors. Cell *126*, 663-676.

[9] Wilmut, I., Schnieke, A.E., McWhir, J., Kind, A.J., and Campbell, K.H.S. (1997). Viable offspring derived from fetal and adult mammalian cells. Nature *385*, 810-813.

[10] Cowan, C.A., Atienza, J., Melton, D.A., and Eggan, K. (2005). Nuclear reprogramming of somatic cells after fusion with human embryonic stem cells. Science *309*, 1369-1373.

[11] Tada, M., Takahama, Y., Abe, K., Nakatsuji, N., and Tada, T. (2001). Nuclear reprogramming of somatic cells by in vitro hybridization with ES cells. Curr Biol *11*, 1553-1558.

[12] Boyer, L.A., Lee, T.I., Cole, M.F., Johnstone, S.E., Levine, S.S., Zucker, J.P., Guenther, M.G., Kumar, R.M., Murray, H.L., Jenner, R.G.*, et al.* (2005). Core transcriptional regulatory circuitry in human embryonic stem cells. Cell *122*, 947-956.

[13] Loh, Y.-H., Wu, Q., Chew, J.-L., Vega, V.B., Zhang, W., Chen, X., Bourque, G., George, J., Leong, B., Liu, J.*, et al.* (2006). The Oct4 and Nanog transcription network regulates pluripotency in mouse embryonic stem cells. Nature Genetics *38*, 431-440.

[14] Miura, K., Okada, Y., Aoi, T., Okada, A., Takahashi, K., Okita, K., Nakagawa, M., Koyanagi, M., Tanabe, K., Ohnuki, M.*, et al.* (2009). Variation in the safety of induced pluripotent stem cell lines. Nat Biotechnol *27*, 743-745.

[15] Hu, B.Y., Weick, J.P., Yu, J., Ma, L.X., Zhang, X.Q., Thomson, J.A., and Zhang, S.C. (2010). Neural differentiation of human induced pluripotent stem cells follows developmental principles but with variable potency. Proc Natl Acad Sci U S A *107*, 4335-4340.

[16] Feng et al., 2010; Feng, Q., Lu, S.J., Klimanskaya, I., Gomes, I., Kim, D., Chung, Y., Honig, G.R., Kim, K.S., and Lanza, R. (2010). Hemangioblastic derivatives from human induced pluripotent stem cells exhibit limited expansion and early senescence. Stem cells (Dayton, Ohio) *28*, 704-712.

[17] Tanaka, T., Tohyama, S., Murata, M., Nomura, F., Kaneko, T., Chen, H., Hattori, F., Egashira, T., Seki, T., Ohno, Y.*, et al.* (2009). In vitro pharmacologic testing using human induced pluripotent stem cell-derived cardiomyocytes. Biochemical and Biophysical Research Communications *385*, 497-502.

[18] Itzhaki, I., Maizels, L., Huber, I., Zwi-Dantsis, L., Caspi, O., Winterstern, A., Feldman, O., Gepstein, A., Arbel, G., Hammerman, H.*, et al.* (2011). Modelling the long QT syndrome with induced pluripotent stem cells. Nature *471*, 225-229.

[19] Aydin, O., Passaro, A.P., Raman, R., Spellicy, S.E., Weinberg, R.P., Kamm, R.D., Sample, M., Truskey, G.A., Zartman, J., Dar, R.D.*, et al.* (2022). Principles for the design of multicellular engineered living systems. APL Bioengineering *6*, 010903.

[20] Elowitz, M.B., and Leibler, S. (2000). A synthetic oscillatory network of transcriptional regulators. Nature *403*, 335-338.

[21] Webster-Wood, V.A., Akkus, O., Gurkan, U.A., Chiel, H.J., and Quinn, R.D. (2017). Organismal engineering: Toward a robotic taxonomic key for devices using organic materials. Science Robotics *2*, eaap9281.

[22] Kim, J., Park, J., Yang, S., Baek, J., Kim, B., Lee, S.H., Yoon, E.S., Chun, K., and Park, S. (2007). Establishment of a fabrication method for a long-term actuated hybrid cell robot. Lab Chip *7*, 1504-1508.

[23] Sample, M., Boulicault, M., Allen, C., Bashir, R., Hyun, I., Levis, M., Lowenthal, C., Mertz, D., Montserrat, N., Palmer, M.J.*, et al.* (2019). Multi-cellular engineered living systems: building a community around responsible research on emergence. Biofabrication *11*, 043001.

[24] Turing, A.M. (1952). The chemical basis of morphogenesis. Philosophical Transactions of the Royal Society of London Series B, Biological Sciences *237*, 37-72.

[25] Sekine, R., Shibata, T., and Ebisuya, M. (2018). Synthetic mammalian pattern formation driven by differential diffusivity of Nodal and Lefty. Nature Communications *9*, 5456.

[26] Toda, S., Blauch, L.R., Tang, S.K.Y., Morsut, L., and Lim, W.A. (2018). Programming self-organizing multicellular structures with synthetic cell-cell signaling. Science *361*, 156-162.

[27] van Laake, L.W., Passier, R., Monshouwer-Kloots, J., Verkleij, A.J., Lips, D.J., Freund, C., den Ouden, K., Ward-van Oostwaard, D., Korving, J., Tertoolen, L.G.*, et al.* (2007). Human embryonic stem cell-derived cardiomyocytes survive and mature in the mouse heart and transiently improve function after myocardial infarction. Stem Cell Res *1*, 9-24.

[28] Shiba, Y., Fernandes, S., Zhu, W.Z., Filice, D., Muskheli, V., Kim, J., Palpant, N.J., Gantz, J., Moyes, K.W., Reinecke, H.*, et al.* (2012). Human ES-cell-derived cardiomyocytes electrically couple and suppress arrhythmias in injured hearts. Nature *489*, 322-325.

[29] Gao, L., Gregorich, Z.R., Zhu, W., Mattapally, S., Oduk, Y., Lou, X., Kannappan, R., Borovjagin, A.V., Walcott, G.P., Pollard, A.E.*, et al.* (2018). Large Cardiac Muscle Patches Engineered From Human Induced-Pluripotent Stem Cell-Derived Cardiac Cells Improve Recovery From Myocardial Infarction in Swine. Circulation *137*, 1712-1730.

[30] Floy, M.E., Shabnam, F., Simmons, A.D., Bhute, V.J., Jin, G., Friedrich, W.A., Steinberg, A.B., and Palecek, S.P. (2022). Advances in Manufacturing Cardiomyocytes from Human Pluripotent Stem Cells. Annual Review of Chemical and Biomolecular Engineering *13*, 255-278.

[31] Gourraud, P.A., Khankhanian, P., Cereb, N., Yang, S.Y., Feolo, M., Maiers, M., Rioux, J.D., Hauser, S., and Oksenberg, J. (2014). HLA diversity in the 1000 genomes dataset. PLoS One *9*, e97282.

[32] Pandey, P.R., Tomney, A., Woon, M.T., Uth, N., Shafighi, F., Ngabo, I., Vallabhaneni, H., Levinson, Y., Abraham, E., and Friedrich Ben-Nun, I. (2019). End-to-End Platform for Human Pluripotent Stem Cell Manufacturing. International journal of molecular sciences *21*.

[33] Tohyama, S., Fujita, J., Fujita, C., Yamaguchi, M., Kanaami, S., Ohno, R., Sakamoto, K., Kodama, M., Kurokawa, J., Kanazawa, H.*, et al.* (2017). Efficient Large-Scale 2D Culture System for Human Induced Pluripotent Stem Cells and Differentiated Cardiomyocytes. Stem Cell Reports *9*, 1406-1414.

[35] Chen, Q., and Hu, G. (2017). Post-transcriptional regulation of the pluripotent state. Current opinion in genetics & development *46*, 15-23.

[36] Lian, X., Hsiao, C., Wilson, G., Zhu, K., Hazeltine, L.B., Azarin, S.M., Raval, K.K., Zhang, J., Kamp, T.J., and Palecek, S.P. (2012). Robust cardiomyocyte differentiation from human pluripotent stem cells via temporal modulation of canonical Wnt signaling. Proc Natl Acad Sci U S A *109*, E1848-1857.

[37] Aguilar, J.S., Begum, A.N., Alvarez, J., Zhang, X.B., Hong, Y., and Hao, J. (2015). Directed cardiomyogenesis of human pluripotent stem cells by modulating Wnt/β-catenin and BMP signalling with small molecules. Biochem J *469*, 235-241.

[38] Tan, Y., Han, P., Gu, Q., Chen, G., Wang, L., Ma, R., Wu, J., Feng, C., Zhang, Y., Wang, L.*, et al.* (2018). Generation of clinical-grade functional cardiomyocytes from human embryonic stem cells in chemically defined conditions. J Tissue Eng Regen Med *12*, 153-163.

[39] Buikema, J.W., Lee, S., Goodyer, W.R., Maas, R.G., Chirikian, O., Li, G., Miao, Y., Paige, S.L., Lee, D., Wu, H.*, et al.* (2020). Wnt Activation and Reduced Cell-Cell Contact Synergistically Induce Massive Expansion of Functional Human iPSC-Derived Cardiomyocytes. Cell Stem Cell *27*, 50-63.e55.

[40] Qiu, X.X., Liu, Y., Zhang, Y.F., Guan, Y.N., Jia, Q.Q., Wang, C., Liang, H., Li, Y.Q., Yang, H.T., Qin, Y.W.*, et al.* (2017). Rapamycin and CHIR99021 Coordinate Robust Cardiomyocyte Differentiation From Human Pluripotent Stem Cells Via Reducing p53-Dependent Apoptosis. J Am Heart Assoc *6*.

[41] Yuasa, S., Itabashi, Y., Koshimizu, U., Tanaka, T., Sugimura, K., Kinoshita, M., Hattori, F., Fukami, S., Shimazaki, T., Ogawa, S.*, et al.* (2005). Transient inhibition of BMP signaling by Noggin induces cardiomyocyte differentiation of mouse embryonic stem cells. Nat Biotechnol *23*, 607-611.

[42] Shimoji, K., Yuasa, S., Onizuka, T., Hattori, F., Tanaka, T., Hara, M., Ohno, Y., Chen, H., Egasgira, T., Seki, T.*, et al.* (2010). G-CSF promotes the proliferation of developing cardiomyocytes in vivo and in derivation from ESCs and iPSCs. Cell Stem Cell *6*, 227-237.

[43] Kattman, S.J., Witty, A.D., Gagliardi, M., Dubois, N.C., Niapour, M., Hotta, A., Ellis, J., and Keller, G. (2011). Stage-specific optimization of activin/nodal and BMP signaling promotes cardiac differentiation of mouse and human pluripotent stem cell lines. Cell Stem Cell *8*, 228-240.

[44] Moussaieff, A., Rouleau, M., Kitsberg, D., Cohen, M., Levy, G., Barasch, D., Nemirovski, A., Shen-Orr, S., Laevsky, I., Amit, M.*, et al.* (2015). Glycolysis-Mediated Changes in Acetyl-CoA and Histone Acetylation Control the Early Differentiation of Embryonic Stem Cells. Cell Metabolism *21*, 392-402.

[45] Tohyama, S., Fujita, J., Hishiki, T., Matsuura, T., Hattori, F., Ohno, R., Kanazawa, H., Seki, T., Nakajima, K., Kishino, Y.*, et al.* (2016). Glutamine Oxidation Is Indispensable for Survival of Human Pluripotent Stem Cells. Cell Metabolism *23*, 663-674.

[46] Berzingi, S., Newman, M., and Yu, H.-G. (2016). Altering bioelectricity on inhibition of human breast cancer cells. Cancer Cell International *16*, 72.

[47] Blackiston, D.J., McLaughlin, K.A., and Levin, M. (2009). Bioelectric controls of cell proliferation: ion channels, membrane voltage and the cell cycle. Cell cycle (Georgetown, Tex) *8*, 3527-3536.

[48] Emmons-Bell, M., Durant, F., Hammelman, J., Bessonov, N., Volpert, V., Morokuma, J., Pinet, K., Adams, D.S., Pietak, A., Lobo, D.*, et al.* (2015). Gap Junctional Blockade Stochastically Induces Different Species-Specific Head Anatomies in Genetically Wild-Type Girardia dorotocephala Flatworms. International journal of molecular sciences *16*, 27865-27896.

[49] Pai, V.P., Aw, S., Shomrat, T., Lemire, J.M., and Levin, M. (2012). Transmembrane voltage potential controls embryonic eye patterning in Xenopus laevis. Development (Cambridge, England) *139*, 313-323.

[50] Atsuta, Y., Tomizawa, R.R., Levin, M., and Tabin, C.J. (2019). L-type voltage-gated Ca<sup>2+</sup> channel Ca<sub>V</sub>1.2 regulates chondrogenesis during limb development. Proceedings of the National Academy of Sciences *116*, 21592-21601.

[51] Arora, N., Alsous, J.I., Guggenheim, J.W., Mak, M., Munera, J., Wells, J.M., Kamm, R.D., Asada, H.H., Shvartsman, S.Y., and Griffith, L.G. (2017). A process engineering approach to increase organoid yield. Development (Cambridge) *144*, 1128-1136.

[52] Kamm, R.D., Bashir, R., Arora, N., Dar, R.D., Gillette, M.U., Griffith, L.G., Kemp, M.L., Kinlaw, K., Levin, M., Martin, A.C.*, et al.* (2018). Perspective: The promise of multi-cellular engineered living systems. APL Bioengineering *2*, 040901.

[53] White, D.E., Kinney, M.A., McDevitt, T.C., and Kemp, M.L. (2013). Spatial Pattern Dynamics of 3D Stem Cell Loss of Pluripotency via Rules-Based Computational Modeling. PLOS Computational Biology *9*, e1002952.

[54] White, D.E., Sylvester, J.B., Levario, T.J., Lu, H., Streelman, J.T., McDevitt, T.C., and Kemp, M.L. (2015). Quantitative multivariate analysis of dynamic multicellular morphogenic trajectories. Integrative Biology (United Kingdom) *7*, 825-833.

[55] Green, J.B.A., and Sharpe, J. (2015). Positional information and reaction-diffusion: Two big ideas in developmental biology combine. Development (Cambridge) *142*, 1203-1211.

[56] Okuda, S., Takata, N., Hasegawa, Y., Kawada, M., Inoue, Y., Adachi, T., Sasai, Y., and Eiraku, M. (2018). Strain-triggered mechanical feedback in self-organizing optic-cup morphogenesis. Science Advances *4*, eaau1354.

[57] Sun, Y., and Wang, Q. (2013). Modeling and simulations of multicellular aggregate self-assembly in biofabrication using kinetic Monte Carlo methods. Soft Matter *9*, 2172-2186.

[58] Sánchez-Gutiérrez, D., Tozluoglu, M., Barry, J.D., Pascual, A., Mao, Y., and Escudero, L.M. (2016). Fundamental physical cellular constraints drive self-organization of tissues. Embo j *35*, 77-88.

[59] Hughes, A.J., Miyazaki, H., Coyle, M.C., Zhang, J., Laurie, M.T., Chu, D., Vavrušová, Z., Schneider, R.A., Klein, O.D., and Gartner, Z.J. (2018). Engineered Tissue Folding by Mechanical Compaction of the Mesenchyme. Developmental cell *44*, 165-178.e166.

[60] Pai, V.P., Pietak, A., Willocq, V., Ye, B., Shi, N.-Q., and Levin, M. (2018). HCN2 Rescues brain defects by enforcing endogenous voltage pre-patterns. Nature Communications *9*, 998.

[61] Villoutreix, P., Andén, J., Lim, B., Lu, H., Kevrekidis, I.G., Singer, A., and Shvartsman, S.Y. (2017). Synthesizing developmental trajectories. PLOS Computational Biology *13*, e1005742.

[62] Oyetunde, T., Bao, F.S., Chen, J.-W., Martin, H.G., and Tang, Y.J. (2018). Leveraging knowledge engineering and machine learning for microbial bio-manufacturing. Biotechnology Advances *36*, 1308-1315.

[63] Arnold, S.J., and Robertson, E.J. (2009). Making a commitment: cell lineage allocation and axis patterning in the early mouse embryo. Nat Rev Mol Cell Biol *10*, 91-103.

[64] Heemskerk, I., and Warmflash, A. (2016). Pluripotent stem cells as a model for embryonic patterning: From signaling dynamics to spatial organization in a dish. Developmental dynamics : an official publication of the American Association of Anatomists *245*, 976-990.

[65] Kamm, R.D., Bashir, R., Arora, N., Dar, R.D., Gillette, M.U., Griffith, L.G., Kemp, M.L., Kinlaw, K., Levin, M., Martin, A.C.*, et al.* (2018). Perspective: The promise of multi-cellular engineered living systems. APL Bioengineering *2*, 040901.

[66] Cervera, J., Pai, V.P., Levin, M., and Mafe, S. (2019). From non-excitable single-cell to multicellular bioelectrical states supported by ion channels and gap junction proteins: Electrical potentials as distributed controllers. Progress in Biophysics and Molecular Biology *149*, 39-53.

[67] Glen, C.M., McDevitt, T.C., and Kemp, M.L. (2018). Dynamic intercellular transport modulates the spatial patterning of differentiation during early neural commitment. Nature Communications *9*, 4111.

[68] Libby, A.R.G., Briers, D., Haghighi, I., Joy, D.A., Conklin, B.R., Belta, C., and McDevitt, T.C. (2019). Automated Design of Pluripotent Stem Cell Self-Organization. Cell systems *9*, 483-495.e410.

[69] Tewary, M., Ostblom, J., Prochazka, L., Zulueta-Coarasa, T., Shakiba, N., Fernandez-Gonzalez, R., and Zandstra, P.W. (2017). A stepwise model of reaction-diffusion and positional information governs self-organized human peri-gastrulation-like patterning. Development (Cambridge, England) *144*, 4298-4312.

[70] Cervera, J., Levin, M., and Mafe, S. (2021). Morphology changes induced by intercellular gap junction blocking: A reaction-diffusion mechanism. Biosystems *209*, 104511.

[71] Chhabra, S., Liu, L., Goh, R., Kong, X., and Warmflash, A. (2019). Dissecting the dynamics of signaling events in the BMP, WNT, and NODAL cascade during self-organized fate patterning in human gastruloids. PLOS Biology *17*, e3000498.

[72] George, L.F., and Bates, E.A. (2022). Mechanisms Underlying Influence of Bioelectricity in Development. Front Cell Dev Biol *10*, 772230.

[73] Jiang, P., Rushing, S.N., Kong, C.-w., Fu, J., Lieu, D.K.-T., Chan, C.W., Deng, W., and Li, R.A. (2010). Electrophysiological properties of human induced pluripotent stem cells. American Journal of Physiology-Cell Physiology *298*, C486-C495.

[74] Wang, K., Xue, T., Tsang, S.Y., Van Huizen, R., Wong, C.W., Lai, K.W., Ye, Z., Cheng, L., Au, K.W., Zhang, J.*, et al.* (2005). Electrophysiological properties of pluripotent human and mouse embryonic stem cells. Stem cells (Dayton, Ohio) *23*, 1526-1534.

[75] Riol, A., Cervera, J., Levin, M., and Mafe, S. (2021). Cell Systems Bioelectricity: How Different Intercellular Gap Junctions Could Regionalize a Multicellular Aggregate. Cancers *13*, 5300.

[76] Zamir, A., Li, G., Chase, K., Moskovitch, R., Sun, B., and Zaritsky, A. (2022). Emergence of synchronized multicellular mechanosensing from spatiotemporal integration of heterogeneous single-cell information transfer. Cell systems *13*, 711-723.e717.

[77] Adams, D.S., and Levin, M. (2006). Inverse drug screens: a rapid and inexpensive method for implicating molecular targets. Genesis *44*, 530-540.

[78] Bhavsar, M.B., Leppik, L., Costa Oliveira, K.M., and Barker, J.H. (2020). Role of Bioelectricity During Cell Proliferation in Different Cell Types. Frontiers in Bioengineering and Biotechnology *8*.

[79] Harris, A.L., Spray, D.C., and Bennett, M.V. (1983). Control of intercellular communication by voltage dependence of gap junctional conductance. The Journal of neuroscience : the official journal of the Society for Neuroscience *3*, 79-100.

[80] Levin, M. (2007). Large-scale biophysics: ion flows and regeneration. Trends Cell Biol *17*, 261-270.

[81] Bowman, C.L., and Baglioni, A. (1984). Application of the Goldman-Hodgkin-Katz current equation to membrane current-voltage data. Journal of theoretical biology *108 1*, 1-29.

[82] Costa, P.F., Emilio, M.G., Fernandes, P.L., Ferreira, H.G., and Ferreira, K.G. (1989). Determination of ionic permeability coefficients of the plasma membrane of Xenopus laevis oocytes under voltage clamp. The Journal of physiology *413*, 199-211.;

[83] Kirichok, Y., Navarro, B., and Clapham, D.E. (2006). Whole-cell patch-clamp measurements of spermatozoa reveal an alkaline-activated Ca2+ channel. Nature *439*, 737-740.

[84] Huettner, J.E., Lu, A., Qu, Y., Wu, Y., Kim, M., and McDonald, J.W. (2006). Gap junctions and connexon hemichannels in human embryonic stem cells. Stem cells (Dayton, Ohio) *24*, 1654-1667.

[85] Picoli, C., Soleilhac, E., Journet, A., Barette, C., Comte, M., Giaume, C., Mouthon, F., Fauvarque, M.O., and Charvériat, M. (2019). High-Content Screening Identifies New Inhibitors of Connexin 43 Gap Junctions. Assay and drug development technologies *17*, 240-248.

[86] Otsu, K., Kuruma, A., Yanagida, E., Shoji, S., Inoue, T., Hirayama, Y., Uematsu, H., Hara, Y., and Kawano, S. (2005). Na+/K+ ATPase and its functional coupling with Na+/Ca2+ exchanger in mouse embryonic stem cells during differentiation into cardiomyocytes. Cell Calcium *37*, 137-151.

[87] Vrbjar, N., Dzurba, A., and Ziegelhöffer, A. (1995). Enzyme kinetics and the activation energy of Mg-ATPase in cardiac sarcolemma: ADP as an alternative substrate. Gen Physiol Biophys *14*, 313-321.

[88] Adams, D.S., and Levin, M. (2012). Measuring resting membrane potential using the fluorescent voltage reporters DiBAC4(3) and CC2-DMPE. Cold Spring Harb Protoc *2012*, 459-464.

[89] Cohen, W.W. (1995). Fast Effective Rule Induction. In Machine Learning Proceedings 1995, A. Prieditis, and S. Russell, eds. (San Francisco (CA): Morgan Kaufmann), pp. 115-123.

[90] Bartocci, E., Gol, E.A., Haghighi, I., and Belta, C. (2018). A Formal Methods Approach to Pattern Recognition and Synthesis in Reaction Diffusion Networks. IEEE Transactions on Control of Network Systems *5*, 308-320.

[91] Hotary, K.B., and Robinson, K.R. (1994). Endogenous electrical currents and voltage gradients in Xenopus embryos and the consequences of their disruption. Developmental biology *166*, 789-800.

[92] Takeda, Y., Ward, S.M., Sanders, K.M., and Koh, S.D. (2005). Effects of the gap junction blocker glycyrrhetinic acid on gastrointestinal smooth muscle cells. American journal of physiology Gastrointestinal and liver physiology *288*, G832-841.

[93] Matchkov, V.V., Rahman, A., Peng, H., Nilsson, H., and Aalkjaer, C. (2004). Junctional and nonjunctional effects of heptanol and glycyrrhetinic acid derivates in rat mesenteric small arteries. Br J Pharmacol *142*, 961-972.

[94] Hille, B. (2001). Ion Channels of Excitable Membranes, Vol 18.

[95] Ng, S.Y., Chin, C.H., Lau, Y.T., Luo, J., Wong, C.K., Bian, Z.X., and Tsang, S.Y. (2010). Role of voltage-gated potassium channels in the fate determination of embryonic stem cells. Journal of cellular physiology 224, 165-177.

[96] Eberhart, R., and Kennedy, J. (1995). A new optimizer using particle swarm theory. Paper presented at: MHS'95 Proceedings of the Sixth International Symposium on Micro Machine and Human Science.

[97] Salas, P.J., and López, E.M. (1982). Validity of the Goldman-Hodgkin-Katz equation in paracellular ionic pathways of gallbladder epithelium. Biochimica et biophysica acta *691*, 178-182.

[98] Bonzanni, M., Payne, S.L., Adelfio, M., Kaplan, D.L., Levin, M., and Oudin, M.J. (2020). Defined extracellular ionic solutions to study and manipulate the cellular resting membrane potential. Biology Open *9*, bio048553.

[99] Gallacher, D.V., and Morris, A.P. (1986). A patch-clamp study of potassium currents in resting and acetylcholine-stimulated mouse submandibular acinar cells. The Journal of physiology *373*, 379-395.

[100] Weir, M.P., and Lo, C.W. (1982). Gap junctional communication compartments in the Drosophila wing disk. Proc Natl Acad Sci U S A *79*, 3232-3235.

[101] Krüger, J., and Bohrmann, J. (2015). Bioelectric patterning during oogenesis: stage-specific distribution of membrane potentials, intracellular pH and ion-transport mechanisms in Drosophila ovarian follicles. BMC Dev Biol *15*, 1-1.

[102] Palacios-Prado, N., and Bukauskas, F.F. (2009). Heterotypic gap junction channels as voltage-sensitive valves for intercellular signaling. Proceedings of the National Academy of Sciences *106*, 14855-14860.

[103] George, L.F., and Bates, E.A. (2022). Mechanisms Underlying Influence of Bioelectricity in Development. Frontiers in Cell and Developmental Biology *10*.

[104] Belus, M.T., Rogers, M.A., Elzubeir, A., Josey, M., Rose, S., Andreeva, V., Yelick, P.C., and Bates, E.A. (2018). Kir2.1 is important for efficient BMP signaling in mammalian face development. Developmental biology *444 Suppl 1*, S297-s307.

[105] Dahal, G.R., Rawson, J., Gassaway, B., Kwok, B., Tong, Y., Ptácek, L.J., and Bates, E. (2012). An inwardly rectifying K+ channel is required for patterning. Development (Cambridge, England) *139*, 3653-3664.

[106] Sun, Y.H., Kao, H.K.J., Chang, C.W., Merleev, A., Overton, J.L., Pretto, D., Yechikov, S., Maverakis, E., Chiamvimonvat, N., Chan, J.W.*, et al.* (2020). Human induced pluripotent stem cell line with genetically encoded fluorescent voltage indicator generated via CRISPR for action potential assessment post-cardiogenesis. Stem cells (Dayton, Ohio) *38*, 90-101.

[107] Voit, E.O. (2018). A First Course in Systems Biology (Garland Science).

[108] Wang, S., Du, L., and Peng, G.-H. (2019). Optogenetic stimulation inhibits the self-renewal of mouse embryonic stem cells. Cell & Bioscience *9*, 73.

[109] Gemel, J., Valiunas, V., Brink, P.R., and Beyer, E.C. (2004). Connexin43 and connexin26 form gap junctions, but not heteromeric channels in co-expressing cells. J Cell Sci *117*, 2469-2480.

[110] Haghighi, I., Jones, A., Kong, Z., Bartocci, E., Gros, R., and Belta, C. (2015). SpaTeL: a novel spatial-temporal logic and its applications to networked systems. In Proceedings of the 18th International Conference on Hybrid Systems: Computation and Control (Seattle, Washington: Association for Computing Machinery), pp. 189–198.

[111] Clarke, E.M., and Emerson, E.A. (1982). Design and synthesis of synchronization skeletons using branching time temporal logic (Berlin, Heidelberg: Springer Berlin Heidelberg).

[112] Morita, Y., and Tohyama, S. (2020). Metabolic Regulation of Cardiac Differentiation and Maturation in Pluripotent Stem Cells: A Lesson from Heart Development. JMA journal *3*, 193-200.

[113] Zhang, J., Zhao, J., Dahan, P., Lu, V., Zhang, C., Li, H., and Teitell, M.A. (2018). Metabolism in Pluripotent Stem Cells and Early Mammalian Development. Cell Metabolism *27*, 332-338.

[114] Lee, J.H., Laronde, S., Collins, T.J., Shapovalova, Z., Tanasijevic, B., McNicol, J.D., Fiebig-Comyn, A., Benoit, Y.D., Lee, J.B., Mitchell, R.R.*, et al.* (2017).

Lineage-Specific Differentiation Is Influenced by State of Human Pluripotency. Cell reports *19*, 20-35.

[115] Lu, V., Dahan, P., Ahsan, F.M., Patananan, A.N., Roy, I.J., Torres, A., Jr., Nguyen, R.M.T., Huang, D., Braas, D., and Teitell, M.A. (2019). Mitochondrial metabolism and glutamine are essential for mesoderm differentiation of human pluripotent stem cells. Cell Res *29*, 596-598.

[116] Correia, C., Koshkin, A., Duarte, P., Hu, D., Teixeira, A., Domian, I., Serra, M., and Alves, P.M. (2017). Distinct carbon sources affect structural and functional maturation of cardiomyocytes derived from human pluripotent stem cells. Scientific reports *7*, 8590.

[117] Lopaschuk, G.D., and Jaswal, J.S. (2010). Energy metabolic phenotype of the cardiomyocyte during development, differentiation, and postnatal maturation. J Cardiovasc Pharmacol *56*, 130-140.

[118] Lionetti, V., Stanley, W.C., and Recchia, F.A. (2011). Modulating fatty acid oxidation in heart failure. Cardiovasc Res *90*, 202-209.

[119] Duarte, N.C., Becker, S.A., Jamshidi, N., Thiele, I., Mo, M.L., Vo, T.D., Srivas, R., and Palsson, B. (2007). Global reconstruction of the human metabolic network based on genomic and bibliomic data. Proc Natl Acad Sci U S A *104*, 1777-1782.

[120] Thiele, I., Swainston, N., Fleming, R.M.T., Hoppe, A., Sahoo, S., Aurich, M.K., Haraldsdottir, H., Mo, M.L., Rolfsson, O., Stobbe, M.D.*, et al.* (2013). A community-driven global reconstruction of human metabolism. Nature Biotechnology *31*, 419-425.

[121] Thiele, I., and Palsson, B. (2010). A protocol for generating a high-quality genome-scale metabolic reconstruction. Nature protocols *5*, 93-121.

[122] Brunk, E., Sahoo, S., Zielinski, D.C., Altunkaya, A., Dräger, A., Mih, N., Gatto, F., Nilsson, A., Preciat Gonzalez, G.A., Aurich, M.K.*, et al.* (2018). Recon3D enables a three-dimensional view of gene variation in human metabolism. Nature Biotechnology *36*, 272-281.

[123] Schomburg, I., Chang, A., Ebeling, C., Gremse, M., Heldt, C., Huhn, G., and Schomburg, D. (2004). BRENDA, the enzyme database: updates and major new developments. Nucleic Acids Res *32*, D431-433.

[124] Schwanhäusser, B., Busse, D., Li, N., Dittmar, G., Schuchhardt, J., Wolf, J., Chen, W., and Selbach, M. (2011). Global quantification of mammalian gene expression control. Nature *473*, 337-342.

[125] Lewis, J.E., Forshaw, T.E., Boothman, D.A., Furdui, C.M., and Kemp, M.L. (2021). Personalized Genome-Scale Metabolic Models Identify Targets of Redox Metabolism in Radiation-Resistant Tumors. Cell systems *12*, 68-81.e11.

[126] Wang, M., Herrmann, C.J., Simonovic, M., Szklarczyk, D., and von Mering, C. (2015). Version 4.0 of PaxDb: Protein abundance data, integrated across model organisms, tissues, and cell-lines. Proteomics *15*, 3163-3168.

[127] Binder, J.X., Pletscher-Frankild, S., Tsafou, K., Stolte, C., O'Donoghue, S.I., Schneider, R., and Jensen, L.J. (2014). COMPARTMENTS: unification and visualization of protein subcellular localization evidence. Database *2014*.

[128] Mookerjee, S.A., and Brand, M.D. (2015). Measurement and Analysis of Extracellular Acid Production to Determine Glycolytic Rate. J Vis Exp, e53464.

[129] Zhang, H., Badur, M.G., Divakaruni, A.S., Parker, S.J., Jäger, C., Hiller, K., Murphy, A.N., and Metallo, C.M. (2016). Distinct Metabolic States Can Support Self-Renewal and Lipogenesis in Human Pluripotent Stem Cells under Different Culture Conditions. Cell reports *16*, 1536-1547.

[130] Hinkle, P.C. (2005). P/O ratios of mitochondrial oxidative phosphorylation. Biochim Biophys Acta *1706*, 1-11.

[131] Dobin, A., Davis, C.A., Schlesinger, F., Drenkow, J., Zaleski, C., Jha, S., Batut, P., Chaisson, M., and Gingeras, T.R. (2013). STAR: ultrafast universal RNA-seq aligner. Bioinformatics 29, 15-21.

[132] Hao, Y., Stuart, T., Kowalski, M., Choudhary, S., Hoffman, P., Hartman, A., Srivastava, A., Molla, G., Madad, S., Fernandez-Granda, C.*, et al.* (2022). Dictionary learning for integrative, multimodal, and scalable single-cell analysis. bioRxiv, 2022.2002.2024.481684.

[133] Liu, Q., Jiang, C., Xu, J., Zhao, M.T., Van Bortle, K., Cheng, X., Wang, G., Chang, H.Y., Wu, J.C., and Snyder, M.P. (2017). Genome-Wide Temporal Profiling of Transcriptome and Open Chromatin of Early Cardiomyocyte Differentiation Derived From hiPSCs and hESCs. Circ Res *121*, 376-391.

[134] Noor, E., Flamholz, A., Liebermeister, W., Bar-Even, A., and Milo, R. (2013). A note on the kinetics of enzyme action: A decomposition that highlights thermodynamic effects. FEBS Letters *587*, 2772-2777.

[135] Tohyama, S., Hattori, F., Sano, M., Hishiki, T., Nagahata, Y., Matsuura, T., Hashimoto, H., Suzuki, T., Yamashita, H., Satoh, Y.*, et al.* (2013). Distinct Metabolic Flow Enables Large-Scale Purification of Mouse and Human Pluripotent Stem Cell-Derived Cardiomyocytes. Cell Stem Cell *12*, 127-137.

[136] Folmes, Clifford D.L., Nelson, Timothy J., Martinez-Fernandez, A., Arrell, D.K., Lindor, Jelena Z., Dzeja, Petras P., Ikeda, Y., Perez-Terzic, C., and Terzic, A. (2011). Somatic Oxidative Bioenergetics Transitions into Pluripotency-Dependent Glycolysis to Facilitate Nuclear Reprogramming. Cell Metabolism *14*, 264-271.

[137] Zaidi, N., Swinnen, J.V., and Smans, K. (2012). ATP-citrate lyase: a key player in cancer metabolism. Cancer Res *72*, 3709-3714.

[138] Werner, J.C., and Sicard, R.E. (1987). Lactate Metabolism of Isolated, Perfused Fetal, and Newborn Pig Hearts. Pediatric Research *22*, 552-556.

[139] Alimperti, S., and Andreadis, S.T. (2015). CDH2 and CDH11 act as regulators of stem cell fate decisions. Stem Cell Res *14*, 270-282.

[140] Friedman, C.E., Nguyen, Q., Lukowski, S.W., Helfer, A., Chiu, H.S., Miklas, J., Levy, S., Suo, S., Han, J.-D.J., Osteil, P.*, et al.* (2018). Single-Cell Transcriptomic Analysis of Cardiac Differentiation from Human PSCs Reveals HOPX-Dependent Cardiomyocyte Maturation. Cell Stem Cell *23*, 586-598.e588.

[141] Cao, N., Liu, Z., Chen, Z., Wang, J., Chen, T., Zhao, X., Ma, Y., Qin, L., Kang, J., Wei, B.*, et al.* (2012). Ascorbic acid enhances the cardiac differentiation of induced pluripotent stem cells through promoting the proliferation of cardiac progenitor cells. Cell Res *22*, 219-236.

[142] Cliff, T.S., Wu, T., Boward, B.R., Yin, A., Yin, H., Glushka, J.N., Prestegaard, J.H., and Dalton, S. (2017). MYC Controls Human Pluripotent Stem Cell Fate Decisions through Regulation of Metabolic Flux. Cell Stem Cell *21*, 502-516.e509.

[143] Song, C., Xu, F., Ren, Z., Zhang, Y., Meng, Y., Yang, Y., Lingadahalli, S., Cheung, E., Li, G., Liu, W.*, et al.* (2019). Elevated Exogenous Pyruvate

Potentiates Mesodermal Differentiation through Metabolic Modulation and AMPK/mTOR Pathway in Human Embryonic Stem Cells. Stem Cell Reports *13*, 338-351.

[144] Mostafavi, S., Balafkan, N., Pettersen, I.K.N., Nido, G.S., Siller, R., Tzoulis, C., Sullivan, G.J., and Bindoff, L.A. (2021). Distinct Mitochondrial Remodeling During Mesoderm Differentiation in a Human-Based Stem Cell Model. Frontiers in Cell and Developmental Biology *9*.

[145] Ye, Z., Wang, S., Zhang, C., and Zhao, Y. (2020). Coordinated Modulation of Energy Metabolism and Inflammation by Branched-Chain Amino Acids and Fatty Acids. Frontiers in Endocrinology *11*.

[146] Birket, M.J., Ribeiro, M.C., Verkerk, A.O., Ward, D., Leitoguinho, A.R., den Hartogh, S.C., Orlova, V.V., Devalla, H.D., Schwach, V., Bellin, M.*, et al.* (2015). Expansion and patterning of cardiovascular progenitors derived from human pluripotent stem cells. Nature Biotechnology *33*, 970-979.

[147] Bulut-Karslioglu, A., Biechele, S., Jin, H., Macrae, T.A., Hejna, M., Gertsenstein, M., Song, J.S., and Ramalho-Santos, M. (2016). Inhibition of mTOR induces a paused pluripotent state. Nature *540*, 119-123.

[148] Pietak, A., and Levin, M. (2016). Exploring Instructive Physiological Signaling with the Bioelectric Tissue Simulation Engine. Frontiers in bioengineering and biotechnology *4*, 55.

[149] Lee, H.-J., Shen, F., Eames, A., Jedrychowski, M.P., and Chandrasekaran, S. (2021). Dynamic metabolic network modeling of a mammalian cell cycle using time-course multi-omics data. bioRxiv, 2021.2010.2011.464012.

[150] Clusin, W.T. (2017). Role of Calcium-Activated Potassium Channels in the Heart. Cardiology Plus *2*.

[151] Weisbrod, D. (2020). Small and Intermediate Calcium Activated Potassium Channels in the Heart: Role and Strategies in the Treatment of Cardiovascular Diseases. Frontiers in physiology *11*, 590534.

[152] Moretti, A., Bellin, M., Welling, A., Jung, C.B., Lam, J.T., Bott-Flügel, L., Dorn, T., Goedel, A., Höhnke, C., Hofmann, F.*, et al.* (2010). Patient-specific induced

pluripotent stem-cell models for long-QT syndrome. N Engl J Med *363*, 1397-1409.

[153] Tordoff, J., Krajnc, M., Walczak, N., Lima, M., Beal, J., Shvartsman, S., and Weiss, R. (2021). Incomplete Cell Sorting Creates Engineerable Structures with Long-Term Stability. Cell Reports Physical Science *2*, 100305.

[154] Oh, Y., Cho, G.-S., Li, Z., Hong, I., Zhu, R., Kim, M.-J., Kim, Yong J., Tampakakis, E., Tung, L., Huganir, R.*, et al.* (2016). Functional Coupling with Cardiac Muscle Promotes Maturation of hPSC-Derived Sympathetic Neurons. Cell Stem Cell *19*, 95-106.

[155] Sun, X., and Nunes, S.S. (2016). Biowire platform for maturation of human pluripotent stem cell-derived cardiomyocytes. Methods *101*, 21-26.

[156] Chernet, B.T., and Levin, M. (2013). Transmembrane voltage potential is an essential cellular parameter for the detection and control of tumor development in a Xenopus model. Disease Models & Mechanisms *6*, 595-607.

[157] Cone, C.D., and Cone, C.M. (1976). Induction of Mitosis in Mature Neurons in Central Nervous System by Sustained Depolarization. Science *192*, 155-158.

[158] Vandenberg, L.N., Morrie, R.D., and Adams, D.S. (2011). V-ATPase-dependent ectodermal voltage and pH regionalization are required for craniofacial morphogenesis. Developmental dynamics : an official publication of the American Association of Anatomists *240*, 1889-1904.

[159] Glen, C.M., Kemp, M.L., and Voit, E.O. (2019). Agent-based modeling of morphogenetic systems: Advantages and challenges. PLOS Computational Biology *15*, e1006577.

[160] Krasznai, Z., Márián, T., Balkay, L., Emri, M., and Trón, L. (1995). Flow cytometric determination of absolute membrane potential of cells. Journal of photochemistry and photobiology B, Biology *28*, 93-99.

[161] Hodgkin, A.L., and Katz, B. (1949). The effect of sodium ions on the electrical activity of giant axon of the squid. The Journal of physiology *108*, 37-77.

[162] Andreev, V.P., and Lisin, E.E. (1992). Investigation of the electroosmotic flow effect on the efficiency of capillary electrophoresis. Electrophoresis *13*, 832-837.

[163] McNamara, H.M., Salegame, R., Tanoury, Z.A., Xu, H., Begum, S., Ortiz, G., Pourquie, O., and Cohen, A.E. (2020). Bioelectrical domain walls in homogeneous tissues. Nature Physics *16*, 357-364.

[164] Davidson, J.S., Baumgarten, I.M., and Harley, E.H. (1986). Reversible inhibition of intercellular junctional communication by glycyrrhetinic acid. Biochem Biophys Res Commun *134*, 29-36.

[165] Chang, K., Creighton, C.J., Davis, C., Donehower, L., Drummond, J., Wheeler, D., Ally, A., Balasundaram, M., Birol, I., Butterfield, Y.S.N.*, et al.* (2013). The Cancer Genome Atlas Pan-Cancer analysis project. Nature Genetics *45*, 1113-1120.

[166] Gu, W., Gaeta, X., Sahakyan, A., Chan, A.B., Hong, C.S., Kim, R., Braas, D., Plath, K., Lowry, W.E., and Christofk, H.R. (2016). Glycolytic Metabolism Plays a Functional Role in Regulating Human Pluripotent Stem Cell State. Cell Stem Cell *19*, 476-490.

[167] Abbey, D., and Seshagiri, P.B. (2017). Ascorbic acid-mediated enhanced cardiomyocyte differentiation of mouse ES-cells involves interplay of DNA methylation and multiple-signals. Differentiation *96*, 1-14.

[168] Ramirez, A.K., Lynes, M.D., Shamsi, F., Xue, R., Tseng, Y.H., Kahn, C.R., Kasif, S., and Dreyfuss, J.M. (2017). Integrating Extracellular Flux Measurements and Genome-Scale Modeling Reveals Differences between Brown and White Adipocytes. Cell reports 21, 3040-3048.

[169] Haraldsdóttir, H.S., Thiele, I., and Fleming, R.M.T. (2012). Quantitative Assignment of Reaction Directionality in a Multicompartmental Human Metabolic Reconstruction. Biophysical Journal 102, 1703-1711.

[170] Snoeck, H.W. (2020). Calcium regulation of stem cells. EMBO reports 21, e50028.

[171] Tonelli, F.M., Santos, A.K., Gomes, D.A., da Silva, S.L., Gomes, K.N., Ladeira, L.O., and Resende, R.R. (2012). Stem cells and calcium signaling. Adv Exp Med Biol 740, 891-916.

[172] Park, J.O., Rubin, S.A., Xu, Y.-F., Amador-Noguez, D., Fan, J., Shlomi, T., and Rabinowitz, J.D. (2016). Metabolite concentrations, fluxes and free energies imply efficient enzyme usage. Nature Chemical Biology 12, 482-489.